



National Library  
of Canada

Bibliothèque nationale  
du Canada

Canadian Theses Service

Service des thèses canadiennes

Ottawa, Canada  
K1A 0N4

## NOTICE

The quality of this microform is heavily dependent upon the quality of the original thesis submitted for microfilming. Every effort has been made to ensure the highest quality of reproduction possible.

If pages are missing, contact the university which granted the degree.

Some pages may have indistinct print especially if the original pages were typed with a poor typewriter ribbon or if the university sent us an inferior photocopy.

Reproduction in full or in part of this microform is governed by the Canadian Copyright Act, R.S.C. 1970, c. C-30, and subsequent amendments.

## AVIS

La qualité de cette microforme dépend grandement de la qualité de la thèse soumise au microfilmage. Nous avons tout fait pour assurer une qualité supérieure de reproduction.

S'il manque des pages, veuillez communiquer avec l'université qui a conféré le grade.

La qualité d'impression de certaines pages peut laisser à désirer, surtout si les pages originales ont été dactylographiées à l'aide d'un ruban usé ou si l'université nous a fait parvenir une photocopie de qualité inférieure.

La reproduction, même partielle, de cette microforme est soumise à la Loi canadienne sur le droit d'auteur, SRC 1970, c. C-30, et ses amendements subséquents.

UNIVERSITY OF ALBERTA

A SHIELDED TRANSVERSE GRADIENT COIL FOR *IN VIVO* NMR

BY

QIN LIU



A THESIS

SUBMITTED TO THE FACULTY OF GRADUATE STUDIES AND RESEARCH

IN PARTIAL FULFILMENT OF THE REQUIREMENTS FOR THE

DEGREE

OF

MASTER OF SCIENCE

IN

MEDICAL PHYSICS

DEPARTMENT OF PHYSICS

EDMONTON, ALBERTA

FALL 1991



National Library  
of Canada

Bibliothèque nationale  
du Canada

Canadian Theses Service    Service des thèses canadiennes

Ottawa, Canada  
K1A 0N4

The author has granted an irrevocable non-exclusive licence allowing the National Library of Canada to reproduce, loan, distribute or sell copies of his/her thesis by any means and in any form or format, making this thesis available to interested persons.

The author retains ownership of the copyright in his/her thesis. Neither the thesis nor substantial extracts from it may be printed or otherwise reproduced without his/her permission.

L'auteur a accordé une licence irrévocable et non exclusive permettant à la Bibliothèque nationale du Canada de reproduire, prêter, distribuer ou vendre des copies de sa thèse de quelque manière et sous quelque forme que ce soit pour mettre des exemplaires de cette thèse à la disposition des personnes intéressées.

L'auteur conserve la propriété du droit d'auteur qui protège sa thèse. Ni la thèse ni des extraits substantiels de celle-ci ne doivent être imprimés ou autrement reproduits sans son autorisation.

ISBN 0-315-69983-3

UNIVERSITY OF ALBERTA  
RELEASE FORM

NAME OF AUTHOR      Qin Liu  
TITLE OF THESIS      A Shielded Transverse Gradient Coil For *in vivo* NMR  
DEGREE              Master of Science  
YEAR THIS DEGREE GRANTED      1991

Permission is hereby granted to THE UNIVERSITY OF ALBERTA LIBRARY to reproduce single copies of this thesis and to lend or sell such copies for private, scholarly or scientific research purposes only.

The author reserves other publication rights, and neither the thesis nor extensive extracts from it may be printed or otherwise reproduced without the author's written permission.



---

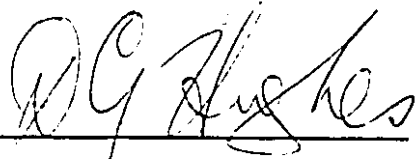
Qin Liu  
Department of Physics  
University of Alberta  
Edmonton, Alberta  
T6G 2J1

Date: July 4, 1991

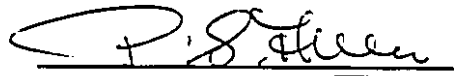
THE UNIVERSITY OF ALBERTA

FACULTY OF GRADUATE STUDIES AND RESEARCH

The undersigned certify that they have read, and recommend to the Faculty of Graduate Studies and Research for acceptance, a thesis entitled "A Shielded Transverse Gradient Coil For *in vivo* NMR" submitted by Qin Liu in partial fulfilment of the requirements for the degree of Master of Science in Medical Physics.



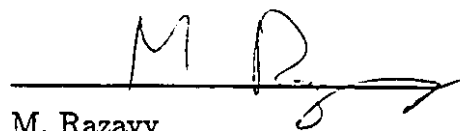
D.G. Hughes, Supervisor



P.S. Allen



F.S. Chute



M. Razavy

Date: July 4, 1991

*TO MY PARENTS*

## ABSTRACT

Switched magnetic field gradients, used in magnetic resonance imaging and *in vivo* spectroscopy, induce eddy currents in nearby conducting structures. These eddy currents give rise to time-dependent magnetic fields which cause troublesome artifacts. However, they can be suppressed by surrounding the primary gradient coil with an appropriately designed shielding coil, thereby reducing the inductive coupling with surrounding conductors.

Such a shielded coil can be designed using the so-called target field approach, recently outlined by Turner, whereby the current distribution on a cylindrical surface, which gives rise to a specific magnetic field profile, can be found. This approach also enables cylindrical coils of minimum inductance to be designed, this being important in achieving gradient pulses with short rise and fall times. In this thesis, the target field approach is developed in detail.

A cylindrical shielded transverse gradient coil was constructed for an animal-size magnet in the *in vivo* NMR facility located at the University of Alberta Hospital. Conducting paths, which allow the required current distribution to be approximated, were milled in copper sheets which were then glued on to cylindrical formers. The use of sheets milled to the desired shapes gives rise to a coil of much lower electrical resistance than the use of discrete wires whose diameter is equal to the thickness of the sheets, thus providing a larger gradient for a given power dissipation. Details of the novel construction process are described.

The magnetic field distribution inside the shielded coil, was found to correspond to a gradient which was uniform to within about 0.5% over a 10 *cm* by 10 *cm* by 10 *cm* cube. The maximum fringe field outside the shielded coil was found to be between 2% and 5% of the maximum fringe field generated by

the primary coil alone. The AC resistance of the coil measured at 5 kHz is considerably larger than the DC resistance, indicating that eddy currents and skin depth effects are important at this frequency.



## ACKNOWLEDGEMENTS

Above all I would like to thank Dr. D.G. Hughes, my research supervisor, for his guidance and assistance throughout the term of this project. He has taught me much about research methods and the presentation of scientific material. On numerous occasions, his insights and questions directed me towards solutions. I wish to thank Dr. R. Turner for providing the coil winding pattern. I would also like to thank Dr. P.S. Allen for his interest and assistance in this project, and Dr. M. Razavy for his help in understanding of the variational method involving complex quantities.

My special thanks should be given to Mr. E. Cairns for his suggestion of a construction method which was the main factor of successful construction of the coil. I would like to express my gratitude to Ken Marsh for his assistance on various technical aspects of the coil construction throughout the term of this project. It is not possible to thank all the other people properly who helped me on various technical aspects, Ray Pegington, Tom Villett, Paul Zimmermann, Gill Lachat, Randy Lundblad, Jim Mackinnon, and Pat Wong. I wish to thank Baolian Xu for his help on preparation of some graphs in the thesis.

I wish to acknowledge the Natural Sciences and Engineering Research Council of Canada and the Medical Research Council of Canada for their financial support. The University of Alberta is also gratefully acknowledged for providing me financial support in the form of the Graduate Assistantship.

Finally, I would like to give my very special thanks to my wife, Yang Zhuo. Her understanding, encouragement and support made this thesis possible.

# TABLE OF CONTENTS

|       |   |    |
|-------|---|----|
| 1     | INTRODUCTION  | 1  |
| 2     | BASIC CONCEPTS OF NMR AND NMR IMAGING   | 4  |
| 2.1   | Nuclear magnetic moments and their behavior in a magnetic field                                 | 4  |
| 2.2   | Classical description of NMR . . . . .  | 5  |
| 2.3   | Detection of NMR signals . . . . .  | 9  |
| 2.4   | Spin-echo techniques . . . . .  | 11 |
| 2.5   | NMR imaging . . . . .   | 13 |
| 3     | THE THEORY OF MAGNETIC SHIELDING OF GRADIENT COILS<br>IN MRI                                    | 18 |
| 3.1   | The magnetic field generated by a current distributed on the<br>surface of a cylinder . . . . . | 19 |
| 3.2   | Magnetic shielding of cylindrical coils . . . . .   | 23 |
| 3.3   | Minimization of the inductance of a cylindrical coil . . . . .                                  | 26 |
| 3.3.1 | Inductance of an unshielded coil . . . . .  | 27 |
| 3.3.2 | Inductance of a shielded coil . . . . .   | 28 |
| 3.3.3 | Minimization of the inductance of a cylindrical coil . . . . .                                  | 30 |
| 3.4   | Shielded gradient coils of minimum inductance . . . . .   | 34 |
| 3.4.1 | A longitudinal gradient coil of minimum inductance . . . . .                                    | 34 |
| 3.4.2 | A transverse gradient coil of minimum inductance . . . . .                                      | 35 |

|       |  |    |
|-------|--|----|
| 4     | DESIGN AND CONSTRUCTION OF A SHIELDED TRANSVERSE GRADIENT COIL                                     | 37 |
| 4.1   | Design considerations . . . . .  | 37 |
| 4.1.1 | Coil dimensions . . . . .  | 37 |
| 4.1.2 | Selection of the type of conducting paths . . . . .  | 38 |
| 4.1.3 | Mechanical stresses on the coil and former . . . . .   | 43 |
| 4.1.4 | Estimate of the temperature rise in the coil due to Joule heating . . . . .                        | 45 |
| 4.2   | Construction of the coil . . . . .   | 46 |
| 5     | TESTING OF THE SHIELDED TRANSVERSE GRADIENT COIL   | 51 |
| 5.1   | Selection of epoxy for bonding copper and fiberglass . . . . .                                     | 51 |
| 5.2   | Measurement of the electrical resistance of the shielded coil . . . . .                            | 52 |
| 5.3   | Measurement of the inductance and AC resistance of the shielded coil . . . . .                     | 56 |
| 5.4   | Measurement of the magnetic field generated by the shielded transverse gradient coil . . . . .     | 60 |
| 5.4.1 | Determination of the magnetic field strength from the voltage induced in the search coil . . . . . | 61 |
| 5.4.2 | Description of the search coil and measurement of its area-turns . . . . .                         | 61 |
| 5.4.3 | The magnetic field profile inside the unshielded primary coil . . . . .                            | 62 |
| 5.4.4 | The magnetic field profile inside the shielded coil . . . . .                                      | 66 |

5.4.5 Shielding performance of the shielded coil . . . . . 75

BIBLIOGRAPHY . . . . . 90

## LIST OF TABLES

|      |  |    |
|------|--|----|
| 5.1  | Mechanical strength of the PC-7 epoxy bonded joint between copper and fiberglass . . . . .   | 53 |
| 5.2  | Resistances of the primary coil alone, the shielding coil alone and the complete shielded coil . . . . .   | 54 |
| 5.3  | Resistances of individual quadrants of the primary and shielding coils . . . . .   | 55 |
| 5.4  | Resistances of the two branches of the shielding coil . . . . .  | 55 |
| 5.5  | Dependence of the inductance, $L_p$ , and AC resistance, $R_L$ , of the primary coil on the frequency, $\nu$ , of the current flowing through it   | 58 |
| 5.6  | Dependence of the inductance, $L_s$ , and AC resistance, $R_L$ , of the shielding coil on the frequency, $\nu$ , of the current flowing through it   | 58 |
| 5.7  | Dependence of the inductance, $L$ , and AC resistance, $R_L$ , of the shielded coil on the frequency, $\nu$ , of the current flowing through it  | 58 |
| 5.8  | Dependence of the inductance, $L$ , and AC resistance, $R_L$ , of the shielded coil on the frequency $\nu$ when the shielding coil is disconnected and shorted so as to mimic passive shielding . . . . .  | 60 |
| 5.9  | The slopes of the best fits to the data of $B_z$ as a function of $x$ at $y = 0, \pm 5 \text{ cm}$ and at $z = -6.3 \text{ cm}, -0.3 \text{ cm}$ and $5.7 \text{ cm}$ for a $1 \text{ A}, 1 \text{ kHz}$ current passing through the unshielded primary coil . . . | 67 |
| 5.10 | The intercepts of the best fits to the data of $B_z$ as a function of $x$ at $y = 0, \pm 5 \text{ cm}$ and at $z = -6.3 \text{ cm}, -0.3 \text{ cm}$ and $5.7 \text{ cm}$ for a $1 \text{ A}, 1 \text{ kHz}$ current passing through the unshielded primary coil   | 67 |

|      |   |    |
|------|---|----|
| 5.11 | The slopes of the best fits to the data of $B_z$ as a function of $x$ at $y = 0, \pm 5 \text{ cm}$ and at $z = -4.7 \text{ cm}, 0.3 \text{ cm}$ and $5.3 \text{ cm}$ for a $1 \text{ A}, 1 \text{ kHz}$ current passing through the shielded coil . . . . .     | 76 |
| 5.12 | The intercepts of the best fits to the data of $B_z$ as a function of $x$ at $y = 0, \pm 5 \text{ cm}$ and at $z = -4.7 \text{ cm}, 0.3 \text{ cm}$ and $5.3 \text{ cm}$ for a $1 \text{ A}, 1 \text{ kHz}$ current passing through the shielded coil . . . . . | 76 |
| 5.13 | The slopes of the best fits to the data of $B_z$ as a function of $x$ at $y = 0, \pm 5 \text{ cm}$ and at $z = -4.7 \text{ cm}, 0.3 \text{ cm}$ and $5.3 \text{ cm}$ for a $1 \text{ A}, 5 \text{ kHz}$ current passing through the shielded coil . . . . .     | 77 |
| 5.14 | The intercepts of the best fits to the data of $B_z$ as a function of $x$ at $y = 0, \pm 5 \text{ cm}$ and at $z = -4.7 \text{ cm}, 0.3 \text{ cm}$ and $5.3 \text{ cm}$ for a $1 \text{ A}, 5 \text{ kHz}$ current passing through the shielded coil . . . . . | 77 |

## LIST OF FIGURES

|     |   |    |
|-----|---|----|
| 2.1 | Precession of the nuclear magnetization in the rotating frame . . .   | 8  |
| 2.2 | A pulse sequence for the spin-echo experiment . . . . .   | 12 |
| 2.3 | A pulse sequence for two-dimensional Fourier imaging . . . . .  | 16 |
| 4.1 | Pattern showing the locations of the spiral cuts in two quadrants<br>of the primary coil . . . . .  | 42 |
| 4.2 | Cross section of the shielded transverse gradient coil in the $x$ - $z$<br>plane, showing mechanical forces acting on it when installed in<br>the magnet . . . . .  | 44 |
| 4.3 | A photograph of the shielded transverse gradient coil . . . . .   | 50 |
| 5.1 | The circuit for the measurement of the coil inductance . . . . .  | 57 |
| 5.2 | The longitudinal component of the magnetic field, $B_z$ , generated<br>by a 1 A, 1 kHz current passing through the unshielded primary<br>coil, plotted as a function of $z$ at (a) $x = 5$ cm and $y = 5$ cm,<br>and (b) $x = -5$ cm and $y = 5$ cm . . . . .   | 63 |
| 5.3 | The longitudinal component of the magnetic field, $B_z$ , generated<br>by a 1 A, 1 kHz current passing through the unshielded primary<br>coil, plotted as a function of $z$ at (a) $x = 5$ cm and $y = 0$ , and<br>(b) $x = -5$ cm and $y = 0$ . . . . .        | 64 |
| 5.4 | The longitudinal component of the magnetic field, $B_z$ , generated<br>by a 1 A, 1 kHz current passing through the unshielded primary<br>coil, plotted as a function of $z$ at (a) $x = 5$ cm and $y = -5$ cm,<br>and (b) $x = -5$ cm and $y = -5$ cm . . . . . | 65 |

|      |  |    |
|------|--|----|
| 5.5  | The longitudinal component of the magnetic field, $B_z$ , generated by a 1 A, 1 kHz current passing through the unshielded primary coil, plotted as a function of $x$ at $y = 0$ and $z = -0.3$ cm . . . .                                   | 68 |
| 5.6  | The longitudinal component of the magnetic field, $B_z$ , generated by a 1 A, 1 kHz current passing through the shielded coil, plotted as a function of $z$ at (a) $x = 5$ cm and $y = 5$ cm, and (b) $x = -5$ cm and $y = 5$ cm . . . . .   | 69 |
| 5.7  | The longitudinal component of the magnetic field, $B_z$ , generated by a 1 A, 1 kHz current passing through the shielded coil, plotted as a function of $z$ at (a) $x = 5$ cm and $y = 0$ , and (b) $x = -5$ cm and $y = 0$ . . . . .        | 70 |
| 5.8  | The longitudinal component of the magnetic field, $B_z$ , generated by a 1 A, 1 kHz current passing through the shielded coil, plotted as a function of $z$ at (a) $x = 5$ cm and $y = -5$ cm, and (b) $x = -5$ cm and $y = -5$ cm . . . . . | 71 |
| 5.9  | The longitudinal component of the magnetic field, $B_z$ , generated by a 1 A, 5 kHz current passing through the shielded coil, plotted as a function of $z$ at (a) $x = 5$ cm and $y = 5$ cm, and (b) $x = -5$ cm and $y = 5$ cm . . . . .   | 72 |
| 5.10 | The longitudinal component of the magnetic field, $B_z$ , generated by a 1 A, 5 kHz current passing through the shielded coil, plotted as a function of $z$ at (a) $x = 5$ cm and $y = 0$ , and (b) $x = -5$ cm and $y = 0$ . . . . .        | 73 |



|      |  |    |
|------|--|----|
| 5.11 | The longitudinal component of the magnetic field, $B_z$ , generated by a 1 A, 5 kHz current passing through the shielded coil, plotted as a function of $z$ at (a) $x = 5\text{ cm}$ and $y = -5\text{ cm}$ , and (b) $x = -5\text{ cm}$ and $y = -5\text{ cm}$ . . . . .      | 74 |
| 5.12 | The longitudinal component of the magnetic field, $B_z$ , generated by a 1 A, 1 kHz current passing through the shielded coil, plotted as a function of $x$ at $y = 0$ and $z = 0.3\text{ cm}$ . . . . .   | 78 |
| 5.13 | The longitudinal component of the magnetic field, $B_z$ , generated by a 1 A, 5 kHz current passing through the shielded coil, plotted as a function of $x$ at $y = 0$ and $z = 0.3\text{ cm}$ . . . . .   | 79 |
| 5.14 | The transverse component of the fringe field, $B_x$ , at $x = 18.5\text{ cm}$ and $y = 0$ , generated by a 1 A, 1 kHz current, plotted as a function of $z$ for (a) the unshielded primary coil, (b) the actively shielded coil and (c) the passively shielded coil . . . . .  | 81 |
| 5.15 | The transverse component of the fringe field, $B_x$ , at $x = -18.5\text{ cm}$ and $y = 0$ , generated by a 1 A, 1 kHz current, plotted as a function of $z$ for (a) the unshielded primary coil, (b) the actively shielded coil and (c) the passively shielded coil . . . . . | 82 |
| 5.16 | The transverse component of the fringe field, $B_x$ , at $x = 18.5\text{ cm}$ and $y = 0$ , generated by a 1 A, 5 kHz current, plotted as a function of $z$ for (a) the unshielded primary coil, (b) the actively shielded coil and (c) the passively shielded coil . . . . .  | 83 |
| 5.17 | The transverse component of the fringe field, $B_x$ , at $x = -18.5\text{ cm}$ and $y = 0$ , generated by a 1 A, 5 kHz current, plotted as a function of $z$ for (a) the unshielded primary coil, (b) the actively shielded coil and (c) the passively shielded coil . . . . . | 84 |

|      |   |    |
|------|---|----|
| 5.18 | The longitudinal component of the fringe field, $B_z$ , at $x = 17.3\text{ cm}$ and $y = 0$ , generated by a $1\text{ A}$ , $1\text{ kHz}$ current, plotted as a function of $z$ for (a) the unshielded primary coil, (b) the actively shielded coil and (c) the passively shielded coil . . . . .  | 85 |
| 5.19 | The longitudinal component of the fringe field, $B_z$ , at $x = -17.3\text{ cm}$ and $y = 0$ , generated by a $1\text{ A}$ , $1\text{ kHz}$ current, plotted as a function of $z$ for (a) the unshielded primary coil, (b) the actively shielded coil and (c) the passively shielded coil . . . . . | 86 |
| 5.20 | The longitudinal component of the fringe field, $B_z$ , at $x = 17.3\text{ cm}$ and $y = 0$ , generated by a $1\text{ A}$ , $5\text{ kHz}$ current, plotted as a function of $z$ for (a) the unshielded primary coil, (b) the actively shielded coil and (c) the passively shielded coil . . . . .  | 87 |
| 5.21 | The longitudinal component of the fringe field, $B_z$ , at $x = -17.3\text{ cm}$ and $y = 0$ , generated by a $1\text{ A}$ , $5\text{ kHz}$ current, plotted as a function of $z$ for (a) the unshielded primary coil, (b) the actively shielded coil and (c) the passively shielded coil . . . . . | 88 |

# Chapter One

## INTRODUCTION

Since its discovery in 1945, the phenomenon of nuclear magnetic resonance (NMR) has been extensively applied in chemistry, physics and biology. However, it was not until 1973 that it was widely appreciated that the proportionality of NMR frequency to the strength of an applied static magnetic field enables the cross sections of objects to be imaged by the application of a magnetic field gradient (Lauterbur 1973, Mansfield and Grannell 1973). It was also realized that these principles could be applied in medicine to produce cross sectional images of the human body that show the spatial distribution of protons and other magnetic nuclei.

The selection of a slice to be imaged involves the application of a pulsed magnetic field gradient in a direction perpendicular to the slice. Moreover, the most successful and widely used technique for forming an image of the slice, namely the two-dimensional Fourier transform (2DFT) method (Kumar *et al.* 1975), requires the application of additional magnetic field gradient pulses, in orthogonal directions within the slice. The time dependent magnetic fields associated with the switching of such gradients induce eddy currents in conducting structures surrounding the gradient coil. These induced eddy currents generate slowly decaying inhomogeneous magnetic fields which cause image artifacts (Henkelman and Bronskill 1987, Robertson 1989).

Another important application of NMR in medicine is NMR spectroscopy in which spectra are obtained from small regions of the human body. Volume localization is achieved, in many cases, using magnetic field gradient pulses. The associated eddy current fields have been found to cause spectral artifacts

(Ordidge and Cresshull 1986).

One way to compensate for the effect of the eddy currents is to modify the shape of the current pulses fed to the gradient coils so as to cancel the eddy current field in the sample space. It has been found in other laboratories (Jehenson *et al.* 1990, Van Vaals and Bergman 1990) and in ours (Robertson 1989) that eddy currents do not always generate uniform gradients. However, this problem can be overcome (Van Vaals and Bergman 1990), at the expense of complexity, by feeding time dependent current pulses to the higher order shim coils with which magnets are equipped in order to improve the homogeneity of the magnetic field. Apart from the complexity, another disadvantage of the pulse shaping approach is that the eddy currents remain in the conducting structures of the magnet, and so does the associated Joule heating which can cause an increased boil-off rate of the cryogens. A possible disadvantage is that the decay of the eddy currents may depend upon the level of the cryogens in the superconducting magnet and, in that case, any compensation scheme would require frequent adjustment to take account of changes in cryogen levels.

An entirely different approach is to prevent the eddy currents occurring in the first place, by magnetically shielding the gradient coil. This can be done by passing a current through a suitably designed shielding coil which surrounds the main gradient coil (Mansfield and Chapman 1986). Chapman *et al.* (1987) and Turner *et al.* (1988) obtained NMR images of greatly improved quality by using such shielded coils. Despite the loss of some sample volume taken up by the shielding, the trend nowadays is for new magnetic resonance imaging (MRI) and magnetic resonance spectroscopy (MRS) systems to be equipped with such shielded gradient coils.

Until recently, longitudinal gradients, *i.e.*,  $G_z = \partial B_z / \partial z$ , where  $z$  is the direction of the main magnetic field, were generated by Maxwell coils (Tanner

1965); orthogonal transverse gradients,  $G_x = \partial B_z / \partial x$  and  $G_y = \partial B_z / \partial y$ , were generated by Golay (saddle) coils (Golay 1958). In an important development, Turner (1988) showed how to design gradient coils which give a more uniform gradient by distributing the current over the surface of a cylinder. Moreover, such coils can be designed to possess the minimum inductance for a fixed coil efficiency (gradient per unit current), this being important in achieving gradient pulses with short rise and fall times.

The project described in this thesis is the design, construction and testing of a cylindrical shielded transverse gradient coil of low inductance and low electrical resistance for a 40 cm bore, 2.35 Tesla animal-size NMR imaging system located at the University of Alberta Hospital. The low electrical resistance, needed for small power dissipation, was achieved by cutting narrow grooves in thick copper sheets, which were rolled to the appropriate radii. The locations of the cuts followed a pattern provided by Turner (1989). The most important part of the work was the development of a method of constructing such a coil.

Basic concepts of NMR and MRI are given in Chapter Two. The theory of magnetic shielding of gradient coils is presented in Chapter Three. Design and construction of a shielded transverse gradient coil are described in Chapter Four. Test results are presented and discussed in Chapter Five.

## Chapter Two

# BASIC CONCEPTS OF NMR AND NMR IMAGING

The theory of NMR has been extensively treated in several excellent texts, ranging from introductory (*e.g.* Farrar and Becker 1971) to very comprehensive (Abragam 1961, Slichter 1978, Morris 1986). In this chapter, we briefly review relevant aspects of the theory of NMR and then describe some basic principles of MRI.

### 2.1 Nuclear magnetic moments and their behavior in a magnetic field

Many nuclei are known to possess a magnetic moment  $\mu$  and an associated spin angular momentum  $\hbar I$ . The two quantities are related by

$$\mu = \gamma \hbar I \quad (2.1)$$

where  $\gamma$  is the magnetogyric ratio which is different for different nuclei, and  $\hbar$  is Planck's constant divided by  $2\pi$ .

In quantum mechanics, an isolated nucleus, placed in a magnetic field of strength  $B_0$  in a direction defined as  $z$ , has  $2I + 1$  discrete energy levels given by

$$E = -\gamma \hbar B_0 m_I \quad (2.2)$$

where  $m_I$  is the quantum number of the  $z$  component of the angular momentum  $\hbar I$  which takes the values  $I, I - 1, \dots, -I$ . Transitions can be induced between these levels by applying an rf magnetic field of angular frequency

$$\omega_0 = \gamma B_0 \quad (2.3)$$

directed at right angles to  $B_0$ .

The equation of motion for the expectation value of the nuclear magnetic moment  $\langle \mu \rangle$ , which is exposed to a magnetic field  $B$ , is

$$\frac{d\langle \mu \rangle}{dt} = \langle \mu \rangle \times \gamma B. \quad (2.4)$$

In a static magnetic field  $B_0$ , the expectation value of the magnetic moment which is inclined at an angle  $\theta$  relative to the magnetic field, precesses about the direction of the field with a frequency given by

$$\omega_0 = -\gamma B_0. \quad (2.5)$$

The interaction energy of the expectation value with the magnetic field increases as the angle  $\theta$  increases from 0 to  $\pi$ . This angle  $\theta$  can be changed by applying an rf magnetic field perpendicular to  $B_0$ .

The above behavior of the expectation value of a magnetic moment in a magnetic field is identical to the behavior predicted by classical mechanics.

## 2.2 Classical description of NMR

In general, the complete treatment of a nuclear spin system requires quantum mechanics. If, however, the system contains only a group of identical spins, in the absence of relaxation, the macroscopic magnetization obeys the equation (Slichter 1978)

$$\frac{dM}{dt} = M \times \gamma B \quad (2.6)$$

where  $M$  is the sum of the nuclear magnetic moments per unit volume. In other words, such a spin system obeys the classical equation of motion. Since most spin systems studied in MRI fall into this category, and the classical description is simple and intuitive, we shall present it here.

In the basic NMR experiment on nuclei with positive  $\gamma$ , the nuclei are exposed to a combination of a steady magnetic field  $B_0$  and a magnetic field  $B_1$  which rotates in a counter-clockwise direction when viewed along the positive  $z$ -axis. Thus one can write

$$B = B_0 + B_1 \quad (2.7)$$

where

$$B_0 = B_0 k \quad (2.8)$$

and

$$B_1 = B_1(i \cos \omega t - j \sin \omega t) \quad (2.9)$$

where  $\omega$  is the angular frequency of the rotating field. (For an NMR experiment on nuclei with negative  $\gamma$ , the magnetic field  $B_1$  must rotate in the opposite sense). To describe an NMR experiment, Eq. 2.6 is not complete, and relaxation effects must be considered. In order to include relaxation, Bloch *et al.* (1946) assumed that both the longitudinal and transverse magnetizations relax exponentially. The longitudinal component returns to the equilibrium static magnetization  $M_0$  with a time constant called  $T_1$ , while the transverse component of the magnetization decays back to its equilibrium value of zero with a time constant called  $T_2$ . This leads to the so-called Bloch equations, namely,

$$\frac{dM_x}{dt} = \gamma(M_y B_0 + M_z B_1 \sin \omega t) - \frac{M_x}{T_2}, \quad (2.10)$$

$$\frac{dM_y}{dt} = \gamma(M_z B_1 \cos \omega t - M_x B_0) - \frac{M_y}{T_2}, \quad (2.11)$$

$$\frac{dM_z}{dt} = -\gamma(M_x B_1 \sin \omega t + M_y B_1 \cos \omega t) - \frac{M_z - M_0}{T_1}. \quad (2.12)$$

To visualize the behavior of the magnetization  $M$  under the influence of  $B_0$  and  $B_1$  more clearly, we introduce a rotating frame  $(x', y', z')$  whose  $z'$ -axis coincides with the corresponding axis of the previous fixed frame, known as the laboratory frame. The rotating frame rotates about its  $z'$ -axis at  $\omega$ , the



frequency of the rotating magnetic field  $B_1$ , and in the same sense as  $B_1$ , so that, in this frame,  $B_1$  is static. Since the axis of rotation coincides with the direction of  $B_0$ ,  $B_0$  will also be static in the rotating frame. If the  $x'$ -axis in the rotating frame is taken along  $B_1$ , Eq. 2.6 becomes

$$\begin{aligned}
 \left(\frac{dM}{dt}\right)_{rot} &= (M \times \gamma B) - (\omega \times M) \\
 &= M \times \gamma \left(B + \frac{\omega}{\gamma}\right) \\
 &= M \times \gamma \left[k' \left(B_0 - \frac{\omega}{\gamma}\right) + i' B_1\right] \\
 &= M \times \gamma B_{eff}
 \end{aligned} \tag{2.13}$$

where

$$B_{eff} = k' \left(B_0 - \frac{\omega}{\gamma}\right) + i' B_1. \tag{2.14}$$

$B_{eff}$  is known as the effective field because of the similarity between Eqs. 2.6 and 2.13.

Eq. 2.13 indicates that, in the rotating frame, the magnetization precesses about a time-independent field  $B_{eff}$  with an angular frequency  $\gamma B_{eff}$ . At resonance,  $\omega$  is equal to  $\gamma B_0$ , and the effective field is given by

$$B_{eff} = i' B_1. \tag{2.15}$$

The magnetization now precesses with an angular frequency  $\gamma B_1$  about  $B_1$  in the rotating frame. If the magnetization is initially parallel to the static field  $B_0$ , as will be the case for spins in equilibrium with the lattice, it will precess in the  $y'$ - $z'$  plane of the rotating frame, always remaining perpendicular to  $B_1$ .

If  $B_1$  is applied as a rectangular pulse of duration  $t_p$ , the magnetization will precess through an angle

$$\theta = \gamma B_1 t_p \tag{2.16}$$

as shown in Figure 2.1a. If  $t_p$  is chosen such that  $\theta = \pi/2$ , the magnetization will

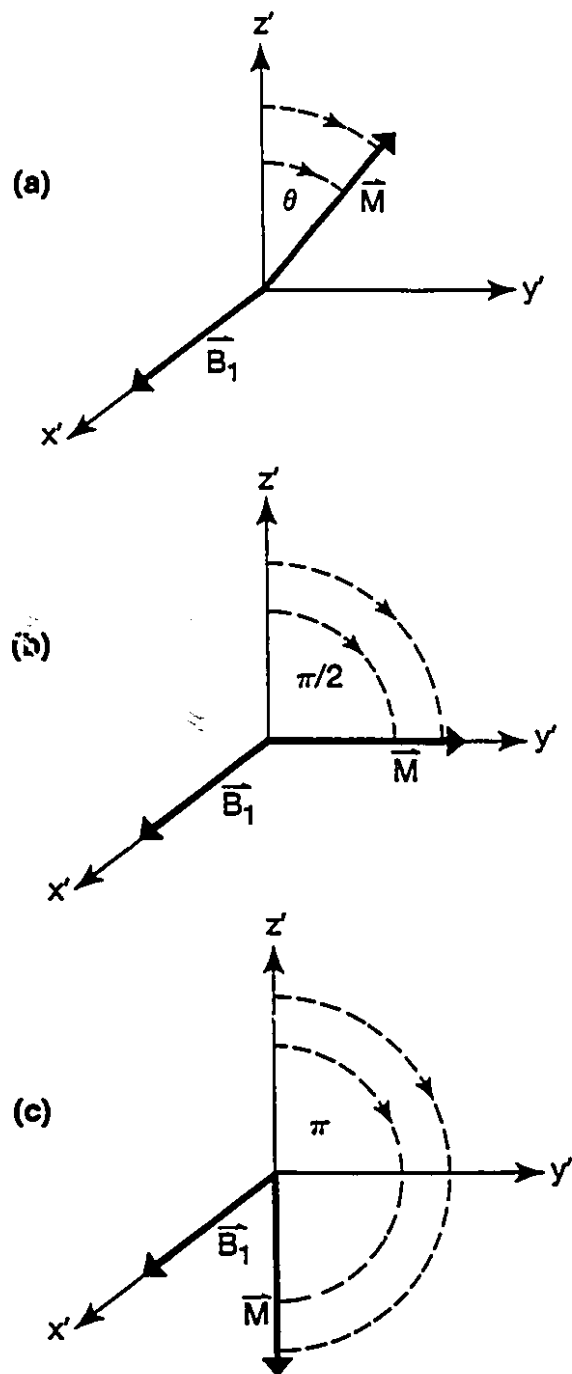


Figure 2.1: Precession of the nuclear magnetization  $M$  (for  $\gamma > 0$ ) in the rotating frame about an “on-resonance”  $B_1$  field through an angle (in radians) of (a)  $\theta$ , (b)  $\pi/2$  and (c)  $\pi$ . The primes here refer to the rotating frame.

be turned from the  $z'$ -axis to the  $y'$ -axis as shown in Figure 2.1b. Such a pulse is referred to as a “90° pulse”. If  $\theta = \pi$ , the magnetization is inverted so as to be antiparallel to the static field  $B_0$ , as shown in Figure 2.1c. Such a pulse is referred to as a “180° pulse”. After a 90° pulse, the magnetization remains stationary in the rotating frame in the absence of relaxation. However, because of the longitudinal and transverse relaxation processes, the magnetization will relax towards its equilibrium value of  $M_0$ . After a 180° pulse, only the longitudinal relaxation occurs, causing the magnetization to relax from  $-M_0$  back along the  $z$ -axis to  $M_0$ .

If the frequency of  $B_1$  is not equal to the resonance frequency  $\gamma B_0$ , a situation called off-resonance, the magnetization will precess about  $B_{eff}$  which is no longer along the  $x'$ -axis of the rotating frame (see Eq. 2.14). In this case, inversion of the magnetization can never be achieved. Moreover, a pulse which would cause a 90° rotation if “on-resonance” will, if applied “off-resonance”, leave some longitudinal magnetization, thereby creating smaller transverse magnetization. While it is possible to adjust an “off-resonance” pulse to rotate the  $z$  magnetization through 90°, it will no longer be directed along the  $y'$ -axis.

## 2.3 Detection of NMR signals

In an NMR spectrometer, the rf magnetic field that excites the spins is generated by applying an rf voltage to a transmitter coil, which is wound in such a way that the rf field is perpendicular to  $B_0$ . That generates a linearly polarized rf field which can be decomposed into two contra-rotating components of equal amplitude. The component which rotates in the same sense as the precessing nuclear magnetic moments is the  $B_1$  referred to in Eq. 2.9. It generates a rotating transverse magnetization, whereas the other rotating component may be neglected near resonance.

The rotating transverse magnetization induces an rf voltage in a so-called receiver coil which is wound with its axis perpendicular to  $\mathcal{B}_0$ . This voltage is subsequently amplified and detected. Because of relaxation, the rotating magnetization decays to zero and so therefore does the rf voltage induced in the coil. This decaying rf voltage is called a free induction decay (FID). In many cases, the same coil serves as both the transmitter and receiver coil.

For practical reasons, the high frequency component of the rf signal is usually removed by phase-sensitive detection in which the rf signal is, in essence, multiplied by a reference signal whose frequency is normally the frequency of the pulse that excites the spins. The resulting signal has two components with frequencies equal to the sum and difference of the rf signal frequency and the reference frequency. A low-pass filter then filters out the high frequency component. By using two phase-sensitive detectors with reference signals differing in phase by  $90^\circ$ , one can distinguish signal frequencies which are higher than the reference frequency, from those which are lower. The use of such phase-sensitive detection is equivalent to observing the motion of the magnetization from a frame rotating at the frequency of the reference signal, instead of from the laboratory frame.

Fourier transformation of the detected FID converts it into a frequency spectrum. Provided the duration of the pulse satisfies the condition

$$t_p \ll (\Delta\nu)^{-1} \quad (2.17)$$

where  $\Delta\nu$  is the width of the NMR spectrum, the Fourier transform of the FID corresponds to the spectrum obtained in a continuous wave (cw) experiment (Slichter 1978) in which a weak rf magnetic field is continuously applied while the frequency or the main magnetic field is swept through the resonance region. Eq. 2.17 implies that the whole spectrum is uniformly excited.

## 2.4 Spin-echo techniques

If the main magnetic field is perfectly homogeneous, the transverse magnetization decays with a time constant  $T_2$ , and so therefore does the corresponding FID. If the magnetic field is not perfectly homogeneous, nuclear spins in different regions of the sample experience different values of the field, and hence precess at different frequencies. This results in a dephasing of the spins, so that the resultant transverse magnetization decays more rapidly to zero. In many cases, the decay is roughly exponential and the decay time is then given the symbol  $T_2^*$ . In that case, one can write

$$\frac{1}{T_2^*} = \frac{1}{T_2} + \frac{1}{2}\gamma\Delta B_0 \quad (2.18)$$

where  $\Delta B_0$  is a measure of the spread in the static field over the sample. For nuclei in liquids and gases, the field inhomogeneity usually largely determines the decay of the transverse magnetization. Hahn (1950), however, discovered that the intrinsic decay of the transverse magnetization, with its time constant  $T_2$ , can be observed in the presence of an inhomogeneous magnetic field by the so-called spin-echo technique.

In a typical spin-echo pulse sequence, a  $90^\circ$  pulse is applied, followed at a time  $\tau$  later by a  $180^\circ$  pulse (the so-called  $90^\circ$ - $\tau$ - $180^\circ$  sequence), as shown in Figure 2.2. Following the  $90^\circ$  pulse, spins experiencing different values of the magnetic field are dephasing, spins with a lower precession frequency lagging behind those with a higher one and *vice versa*. At a time  $t = \tau$ , applying a  $180^\circ$  pulse rotates all the spins so that the spins with a lower precession frequency are now an equal amount ahead of those with a higher one. It follows that all the spins come in phase again at a time  $t = 2\tau$  and form a transverse magnetization with an amplitude governed only by the decay with the characteristic time  $T_2$ . The signal generated is called a spin echo. If the  $180^\circ$  pulse is in phase with the

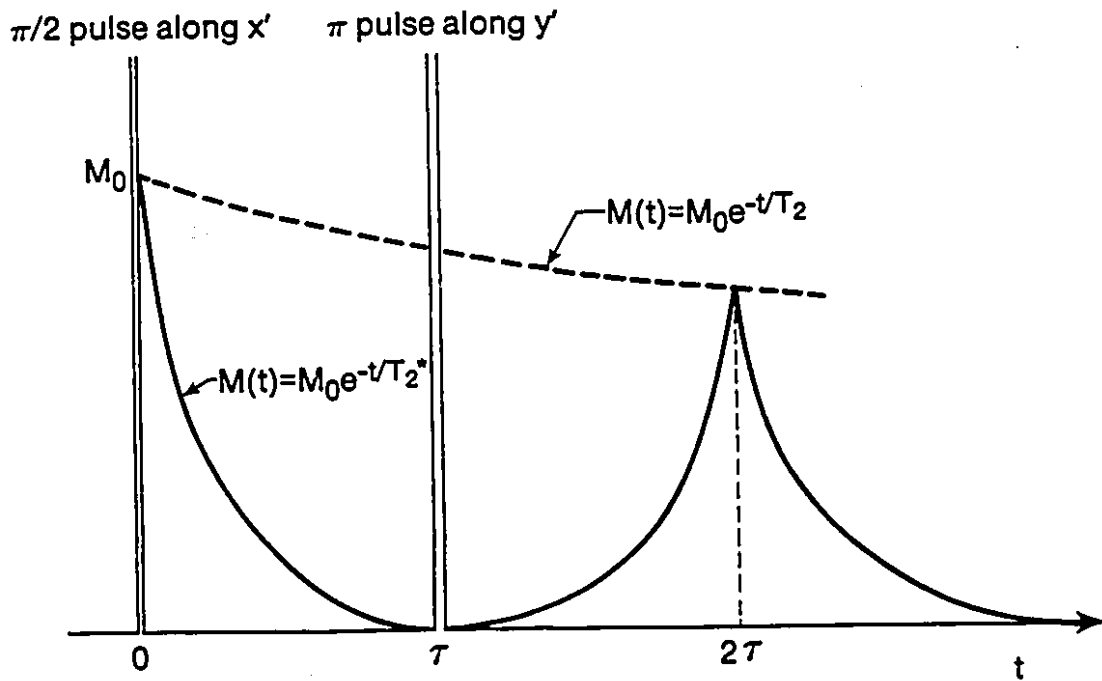


Figure 2.2: A spin-echo experiment. A  $90^\circ$  pulse along the  $x'$ -axis rotates the magnetization to the  $y'$ -axis. The signal arising from this magnetization decays with a characteristic time  $T_2^*$ . At time  $\tau$ , a  $180^\circ$  pulse is applied along the  $y'$ -axis causing the magnetization to refocus at time  $2\tau$ . The magnetization at  $2\tau$  is reduced from its initial value of  $M_0$  because of  $T_2$  processes which are not reversed by the  $180^\circ$  pulse

90° pulse, the spin echo is inverted as compared with the FID. If the phase of the 180° pulse is shifted by 90° relative to the 90° pulse, the spin echo is of the same sign as the FID. The spin echo produced by a 90°– $\tau$ –180° sequence can be considered as two “back to back” free induction decays with their maximum amplitudes at a time  $t = 2\tau$  after the 90° pulse, as shown in Figure 2.2. In this figure, it has been assumed that the phase of the 180° pulse is shifted by 90° relative to the 90° pulse.

Spin-echo techniques were originally developed for measuring spin-spin relaxation times  $T_2$ . Now they are widely used in high-resolution NMR spectroscopy and in magnetic resonance imaging.

## 2.5 NMR imaging

Since NMR imaging was initially proposed in the early 1970s, many imaging methods, such as point, line, planar, and three-dimensional imaging, have been reported. In recent years, two-dimensional Fourier imaging (Kumar *et al.* 1975) has been widely used and adopted in most commercial imaging systems, and so we shall confine ourselves to describing this technique.

As we have seen, the NMR frequency is proportional to the applied static magnetic field. If this static field has a known space dependence, one is able to obtain information about the spatial dependence of nuclear spin density and other NMR parameters, such as relaxation times, from the frequency domain representation of the NMR signal. A spatial dependence of the magnetic field can be achieved by superimposing a uniform magnetic field gradient  $G = \nabla B_z$  on the static magnetic field so that the  $z$  component of the total field is given by

$$B_z(\mathbf{r}) = B_0 + G \cdot \mathbf{r}. \quad (2.19)$$

(The transverse components of the gradient field,  $B_x(\mathbf{r})$  and  $B_y(\mathbf{r})$  are unimportant since they are perpendicular to the large main field  $B_0$ , which is in the longitudinal,  $z$ , direction.)

For two-dimensional imaging, it is necessary to isolate a slice of the object to be imaged. This can be achieved by applying a uniform magnetic field gradient in a direction perpendicular to the slice, say the  $z$  direction, and then using a so-called selective  $90^\circ$  rf pulse which rotates all spins, whose resonance frequencies lie in a narrow frequency range  $\Delta\omega$ , through  $90^\circ$ , but does not excite those outside that range. That is, the frequency profile of the pulse has the shape of a top hat. Therefore, in the presence of a uniform magnetic field gradient  $G_z$ , the spins which are excited lie in a plane of thickness

$$\Delta z = \frac{\Delta\omega}{\gamma G_z} \quad (2.20)$$

normal to the  $z$ -axis and centered at

$$z = \frac{\omega - \gamma B_0}{\gamma G_z} \quad (2.21)$$

where  $\omega$  is the frequency of the rf field.

It is known from Fourier transform theory (*e.g.* Brigham 1974) that a top hat function in the frequency domain corresponds in the time domain to a sinc function which extends out to infinity. Time limited pulses are obviously required in practice. One possibility is to use a gaussian modulated rf pulse, which gives a gaussian profile in the frequency domain (Brigham 1974), and hence in space. A pulse which is closer to the ideal top hat shape is a sinc function in the time domain multiplied by a gaussian function (Hutchison *et al.* 1978). The Fourier transform of this is a gaussian convoluted with a top hat function. Although an ideal  $90^\circ$  selective pulse in the presence of a uniform magnetic field gradient will rotate all spins in a slice normal to the field gradient from the  $z$ -axis into the  $x$ - $y$  plane, the excited spins accumulate different phases at the



end of the slice selection (Morris 1986). However, since the phase distribution is almost proportional to the  $z$  coordinate, the problem can be largely overcome by reversing the direction of the  $z$  gradient immediately after the rf magnetic field is switched off, and leaving the reversed gradient on just long enough for the spins to refocus (Hoult 1979).

After slice selection has been achieved, the location of spins within the slice is encoded into the NMR signal by employing two orthogonal gradients which are perpendicular to the gradient used for the slice selection. If the slice is perpendicular to the  $z$  direction, then a gradient  $G_x$  in the  $x$  direction, say, can be used to encode  $x$  positional information into the frequency of the NMR signal and a gradient  $G_y$  in the  $y$  direction can be used to encode  $y$  positional information into the phase of the signal.

The frequency encoding in the  $x$  direction can, in principle, be achieved by applying only one  $x$  gradient pulse and recording the time domain signal during the pulse. However, dephasing of spins during the finite rise time of the gradient pulse causes serious loss of signal. To overcome this problem, two  $x$  gradient pulses are used as shown in Figure 2.3, in combination with the spin-echo techniques discussed in Section 2.4. The first  $x$  gradient pulse, called the read compensation gradient pulse, causes the spins to dephase. After the gradient is switched off, a non-selective  $180^\circ$  rf pulse is applied, followed by a second  $x$  gradient pulse, the so-called read gradient pulse, which has the same polarity as the first. This causes the spins to rephase and a spin echo to form at a time when the time integral of the read gradient pulse is equal to that of the read compensation gradient pulse. The spin echo can be adjusted to form at a time well after the rise time of the read gradient pulse by choosing an appropriate strength and duration of the read compensation gradient pulse, so that the echo is formed in a constant field gradient. Another important requirement is that

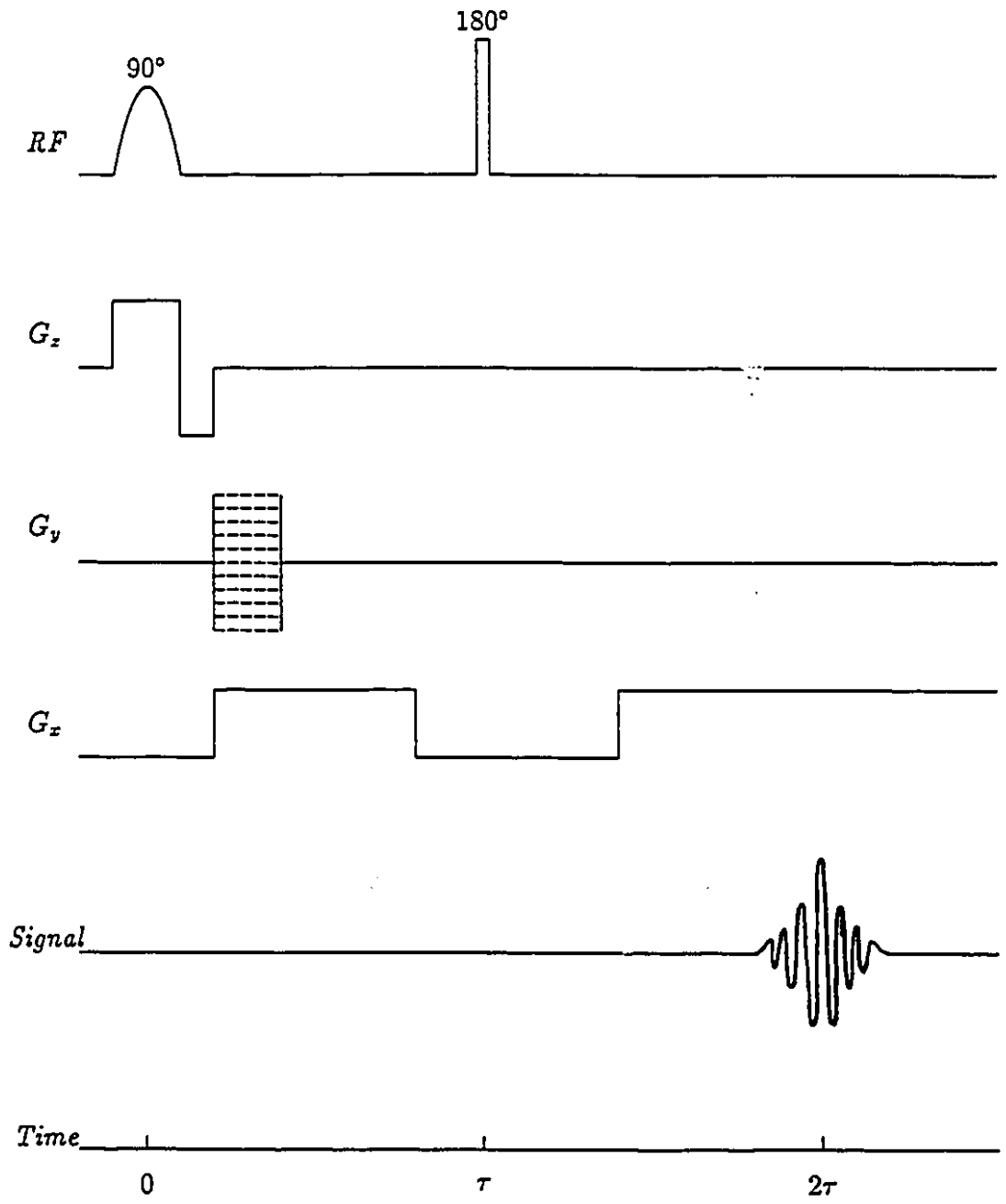


Figure 2.3: A pulse sequence for two-dimensional Fourier imaging

the echo is formed at the same time  $2\tau$  at which the echo is formed in the absence of gradient pulses. This ensures that there is no loss of signal due to an inhomogeneity of the main magnetic field in the  $y$  direction.

The strength of the read gradient must be such that the separation of adjacent channels in the frequency domain, corresponding to the desired spatial resolution, must be greater than the spectral width associated with the field inhomogeneity. The rate at which the echo is sampled must satisfy the Nyquist condition, namely that the dwell time,  $\Delta t$ , be given by

$$\Delta t < \frac{\pi}{\gamma G_x x_{max}} \quad (2.22)$$

where  $x_{max}$  is the extent of the slice in the  $x$  direction. The total acquisition time is then  $n \Delta t$ , where  $n$  is the number of channels in the frequency space. Fourier transformation of the acquired data gives a projection of the slice onto the  $x$ -axis.

To obtain a two-dimensional image, a phase-encoding gradient of amplitude  $G_y$  and duration  $\tau_y$  is applied in the  $y$  direction between the  $90^\circ$  rf pulse and the spin echo, as shown in Figure 2.3. Its effect is to introduce a phase shift,  $\gamma G_y y_i \tau_y$ , to the signal from the spins in the slice whose  $y$  coordinate is  $y_i$ . That is, the  $y$  directional information is encoded into the phase of the echo signal. By incrementing the amplitude of the  $y$  gradient pulse by a small constant amount several times, and repeating the imaging sequence for each increment, a two-dimensional image can be obtained by two-dimensional Fourier transformation of the resulting time domain signal. The required increment in the amplitude of the  $y$  gradient is governed according to the Nyquist condition by the extent of the slice in the  $y$  direction. The number of increments is determined by the desired resolution in the  $y$  direction.

## Chapter Three

# THE THEORY OF MAGNETIC SHIELDING OF GRADIENT COILS IN MRI

To prevent eddy currents from being induced in the conducting structure of an NMR magnet by switched magnetic field gradients, it is necessary to use magnetic shielding so that the magnetic field generated by the gradient coil is essentially zero everywhere outside the coil (Mansfield and Chapman 1986). This can be achieved by surrounding the coil with a conducting shell of sufficient thickness, provided the current in the gradient coil does not possess a DC component. This is called passive shielding (Turner and Bowley 1986). Since this thesis deals with the construction of a gradient coil that will receive current pulses which do have a DC component, we shall confine our discussion to so-called active shielding, in which the shielding is achieved by passing a time-dependent current through an appropriately designed coil wound outside the gradient coil. Also, because of the cylindrical geometry of the magnet in which our coil will be installed, we shall be discussing a shielded gradient coil consisting of two coaxial cylinders.

In this chapter, we shall derive theoretical expressions for the magnetic field generated by a current distributed on the surface of a cylinder. These expressions are then applied to the design of cylindrical coils by the target field approach (Turner 1986) in which the current distribution on the surface of a cylinder, which generates a specified field profile, is determined. An important property of a gradient coil is its inductance since this, together with its resistance, determines the rise and fall times of the gradient pulses. We therefore derive expressions for the inductance of a cylindrical coil and the condition for its

minimization. This enables expressions for the current distribution in shielded transverse and longitudinal gradient coils to be derived. The presentation is based on the theory briefly outlined by Turner and Bowley (1986) and Turner (1986, 1988). Attention is drawn to two errors in the expressions presented by these workers.

### 3.1 The magnetic field generated by a current distributed on the surface of a cylinder

In the following derivation we assume that the frequency of the current is sufficiently low so that displacement currents may be ignored. This assumption is reasonable because the switching rate of the magnetic field gradient in MRI experiments is of the order of a kiloHertz or less.

We shall consider the current confined to the surface of a cylinder, and use a cylindrical coordinate system in which the  $z$ -axis coincides with the axis of the cylinder. The coordinates of a point in space  $(\rho, \phi, z)$  are thus related to its cartesian coordinates  $(x, y, z)$  by

$$\begin{aligned}\rho &= \sqrt{x^2 + y^2} \\ \tan \phi &= \frac{y}{x} \\ z &= z.\end{aligned}\tag{3.1}$$

We suppose that a surface current of density  $\mathbf{J}(\mathbf{r}')$  which vanishes at infinity flows on the surface of a cylinder of infinite length and of radius  $a$ , and that there is no current flowing in the radial direction. The contribution of the current flowing in an area  $a d\phi' dz'$  near a point  $(a, \phi', z')$  to the vector potential  $\mathbf{A}(\mathbf{r})$  at a point  $(\rho, \phi, z)$  is given by

$$d\mathbf{A}(\mathbf{r}) = \frac{\mu_0 \mathbf{J}(\mathbf{r}') a d\phi' dz'}{4\pi |\mathbf{r} - \mathbf{r}'|}\tag{3.2}$$

where

$$\mathbf{r} = \rho \cos \phi \mathbf{i} + \rho \sin \phi \mathbf{j} + z \mathbf{k}$$

$$\mathbf{r}' = a \cos \phi' \mathbf{i} + a \sin \phi' \mathbf{j} + z' \mathbf{k}.$$

The three components of  $dA(\mathbf{r})$  are given by

$$dA_\rho(\mathbf{r}) = \frac{\mu_0 J_{\phi'}(\mathbf{r}') \sin(\phi - \phi') a d\phi' dz'}{4\pi |\mathbf{r} - \mathbf{r}'|} \quad (3.3)$$

$$dA_\phi(\mathbf{r}) = \frac{\mu_0 J_{\phi'}(\mathbf{r}') \cos(\phi - \phi') a d\phi' dz'}{4\pi |\mathbf{r} - \mathbf{r}'|} \quad (3.4)$$

$$dA_z(\mathbf{r}) = \frac{\mu_0 J_{z'}(\mathbf{r}') a d\phi' dz'}{4\pi |\mathbf{r} - \mathbf{r}'|}. \quad (3.5)$$

The components of the vector potential  $A(\mathbf{r})$ , caused by the surface current of density  $J(\mathbf{r}')$  which vanishes at infinity, are therefore given by (Morse and Feshbach 1953a)

$$A_\rho(\mathbf{r}) = \frac{\mu_0 a}{4\pi} \int_{-\pi}^{\pi} d\phi' \sin(\phi - \phi') \int_{-\infty}^{\infty} dz' \frac{J_{\phi'}(\mathbf{r}')}{|\mathbf{r} - \mathbf{r}'|} \quad (3.6)$$

$$A_\phi(\mathbf{r}) = \frac{\mu_0 a}{4\pi} \int_{-\pi}^{\pi} d\phi' \cos(\phi - \phi') \int_{-\infty}^{\infty} dz' \frac{J_{\phi'}(\mathbf{r}')}{|\mathbf{r} - \mathbf{r}'|} \quad (3.7)$$

$$A_z(\mathbf{r}) = \frac{\mu_0 a}{4\pi} \int_{-\pi}^{\pi} d\phi' \int_{-\infty}^{\infty} dz' \frac{J_{z'}(\mathbf{r}')}{|\mathbf{r} - \mathbf{r}'|}. \quad (3.8)$$

To derive the required expression for the current distribution, it is important to use the Green's function (Jackson 1962)

$$\frac{1}{|\mathbf{r} - \mathbf{r}'|} = \frac{2}{\pi} \sum_{m=-\infty}^{\infty} \int_0^{\infty} dk e^{im(\phi-\phi')} \cos k(z-z') I_m(k\rho_{<}) K_m(k\rho_{>}) \quad (3.9)$$

where  $I_m(x)$  and  $K_m(x)$  are the  $m$ th order modified Bessel functions of the first and the second kinds, respectively, and  $\rho_{<}$  is the smaller of  $\rho$  and  $a$ , while  $\rho_{>}$  is the larger of the two quantities. If the trigonometrical function  $\cos k(z-z')$  is expressed in terms of exponential functions, Eq. 3.9 can be written as

$$\begin{aligned} \frac{1}{|\mathbf{r} - \mathbf{r}'|} &= \frac{1}{\pi} \sum_{m=-\infty}^{\infty} \int_0^{\infty} dk e^{im(\phi-\phi')} e^{ik(z-z')} I_m(k\rho_{<}) K_m(k\rho_{>}) \\ &+ \frac{1}{\pi} \sum_{m=-\infty}^{\infty} \int_0^{\infty} dk e^{im(\phi-\phi')} e^{-ik(z-z')} I_m(k\rho_{<}) K_m(k\rho_{>}). \end{aligned}$$

By replacing  $k$  by  $-s$  in the second integral of the above equation, one obtains

$$\begin{aligned} \frac{1}{|\mathbf{r} - \mathbf{r}'|} &= \frac{1}{\pi} \sum_{m=-\infty}^{\infty} \int_0^{\infty} dk e^{im(\phi-\phi')} e^{ik(z-z')} I_m(k\rho_{<}) K_m(k\rho_{>}) \\ &\quad - \frac{1}{\pi} \sum_{m=-\infty}^{\infty} \int_0^{-\infty} ds e^{im(\phi-\phi')} e^{is(z-z')} I_m(-s\rho_{<}) K_m(-s\rho_{>}) \end{aligned}$$

or

$$\begin{aligned} \frac{1}{|\mathbf{r} - \mathbf{r}'|} &= \frac{1}{\pi} \sum_{m=-\infty}^{\infty} \int_0^{\infty} dk e^{im(\phi-\phi')} e^{ik(z-z')} I_m(|k|\rho_{<}) K_m(|k|\rho_{>}) \\ &\quad + \frac{1}{\pi} \sum_{m=-\infty}^{\infty} \int_{-\infty}^0 ds e^{im(\phi-\phi')} e^{is(z-z')} I_m(|s|\rho_{<}) K_m(|s|\rho_{>}) \quad (3.10) \end{aligned}$$

where  $|s|$  and  $|k|$  are the absolute values of  $s$  and  $k$ . In obtaining Eq. 3.10, we have used the identity

$$\int_a^b f(x) dx = - \int_b^a f(x) dx \quad (3.11)$$

and the fact that  $k$  and  $-s$  are always positive. Changing the integration variable  $s$  in the second integral of Eq. 3.10 back to  $k$ , one obtains

$$\begin{aligned} \frac{1}{|\mathbf{r} - \mathbf{r}'|} &= \frac{1}{\pi} \sum_{m=-\infty}^{\infty} \int_0^{\infty} dk e^{im(\phi-\phi')} e^{ik(z-z')} I_m(|k|\rho_{<}) K_m(|k|\rho_{>}) \\ &\quad + \frac{1}{\pi} \sum_{m=-\infty}^{\infty} \int_{-\infty}^0 dk e^{im(\phi-\phi')} e^{ik(z-z')} I_m(|k|\rho_{<}) K_m(|k|\rho_{>}) \end{aligned}$$

which is identical to

$$\frac{1}{|\mathbf{r} - \mathbf{r}'|} = \frac{1}{\pi} \sum_{m=-\infty}^{\infty} \int_{-\infty}^{\infty} dk e^{im(\phi-\phi')} e^{ik(z-z')} I_m(|k|\rho_{<}) K_m(|k|\rho_{>}). \quad (3.12)$$

It should be pointed out that Eq. 3.12 is not the same as Eq. 6 in Turner and Bowley's article (1986) which reads

$$\frac{1}{|\mathbf{r} - \mathbf{r}'|} = \frac{1}{\pi} \sum_{m=-\infty}^{\infty} \int_{-\infty}^{\infty} dk e^{im(\phi-\phi')} e^{ik(z-z')} I_m(k\rho_{<}) K_m(k\rho_{>}). \quad (3.13)$$

In their expression, the arguments of the modified Bessel functions, namely  $k\rho_{<}$  and  $k\rho_{>}$ , are not always positive, which is incorrect according to our derivation of Eq. 3.12.

It is useful to define the Fourier transforms of the components of  $J(\mathbf{r}')$  as follows (Turner and Bowley 1986)

$$J_{\phi}^m(k) = \frac{1}{2\pi} \int_{-\pi}^{\pi} d\phi' e^{-im\phi'} \int_{-\infty}^{\infty} dz' J_{\phi'}(a, \phi', z') e^{-ikz'} \quad (3.14)$$

$$J_z^m(k) = \frac{1}{2\pi} \int_{-\pi}^{\pi} d\phi' e^{-im\phi'} \int_{-\infty}^{\infty} dz' J_z(a, \phi', z') e^{-ikz'}, \quad (3.15)$$

so that the inverse Fourier transforms are

$$J_{\phi'}(a, \phi', z') = \frac{1}{2\pi} \sum_{m=-\infty}^{\infty} \int_{-\infty}^{\infty} dk J_{\phi}^m(k) e^{im\phi'} e^{ikz'} \quad (3.16)$$

$$J_z(a, \phi', z') = \frac{1}{2\pi} \sum_{m=-\infty}^{\infty} \int_{-\infty}^{\infty} dk J_z^m(k) e^{im\phi'} e^{ikz'}. \quad (3.17)$$

By substituting Eq. 3.12 into Eqs. 3.6, 3.7 and 3.8, and using the definitions 3.14 and 3.15, one finds that the components of  $A$  inside the cylinder ( $\rho < a$ ) are

$$A_{\rho}(\mathbf{r}) = \frac{i\mu_0 a}{4\pi} \sum_{m=-\infty}^{\infty} \int_{-\infty}^{\infty} dk J_{\phi}^m(k) e^{im\phi} e^{ikz} [I_{m-1}(|k|\rho) K_{m-1}(|k|a) - I_{m+1}(|k|\rho) K_{m+1}(|k|a)] \quad (3.18)$$

$$A_{\phi}(\mathbf{r}) = \frac{\mu_0 a}{4\pi} \sum_{m=-\infty}^{\infty} \int_{-\infty}^{\infty} dk J_{\phi}^m(k) e^{im\phi} e^{ikz} [I_{m-1}(|k|\rho) K_{m-1}(|k|a) + I_{m+1}(|k|\rho) K_{m+1}(|k|a)] \quad (3.19)$$

$$A_z(\mathbf{r}) = \frac{\mu_0 a}{2\pi} \sum_{m=-\infty}^{\infty} \int_{-\infty}^{\infty} dk J_z^m(k) e^{im\phi} e^{ikz} I_m(|k|\rho) K_m(|k|a). \quad (3.20)$$

One can write similar expressions for the components of  $A$  outside the cylinder ( $\rho > a$ ) by exchanging the positions of  $\rho$  and  $a$  in the integrands in Eqs. 3.18 to 3.20.

In order to obtain the expression for the magnetic field  $B$ , we use Eqs. 3.16 and 3.17 to derive an important relation between  $J_{\phi}^m(k)$  and  $J_z^m(k)$ . In the absence of charge accumulation, the equation of continuity states

$$\nabla' \cdot J(\mathbf{r}') = 0. \quad (3.21)$$

If the current flows only on the surface of a cylinder of radius  $a$ , Eq. 3.21 can be written as

$$\frac{1}{a} \frac{\partial J_{\phi'}}{\partial \phi'} + \frac{\partial J_z'}{\partial z'} = 0. \quad (3.22)$$



Substituting Eqs. 3.16 and 3.17 into Eq. 3.22 yields

$$\frac{i}{2\pi} \sum_{m=-\infty}^{\infty} \int_{-\infty}^{\infty} dk \left[ \frac{m}{a} J_{\phi}^m(k) + k J_z^m(k) \right] e^{im\phi'} e^{ikz'} = 0. \quad (3.23)$$

For Eq. 3.23 to be true, the sum of the two terms in the square brackets must vanish for each value of  $m$ . That is,  $J_{\phi}^m(k)$  and  $J_z^m(k)$  are related as follows

$$J_z^m(k) = -\frac{m}{ka} J_{\phi}^m(k). \quad (3.24)$$

By taking the curl of the vector potential  $A$  and using Eq. 3.24 and the recurrence relations for modified Bessel functions, namely

$$I_{m-1}(x) = I'_m(x) + \frac{m}{x} I_m(x) \quad (3.25)$$

$$I_{m+1}(x) = I'_m(x) - \frac{m}{x} I_m(x) \quad (3.26)$$

$$K_{m-1}(x) = K'_m(x) - \frac{m}{x} K_m(x) \quad (3.27)$$

$$K_{m+1}(x) = -K'_m(x) + \frac{m}{x} K_m(x) \quad (3.28)$$

where  $I'_m(x)$  and  $K'_m(x)$  are respectively derivatives of  $I_m(x)$  and  $K_m(x)$  with respect to  $x$ , the components of the magnetic field  $B$  inside the cylinder can be written as follows

$$B_{\rho}(\mathbf{r}) = \frac{i\mu_0 a}{2\pi} \sum_{m=-\infty}^{\infty} \int_{-\infty}^{\infty} k dk J_{\phi}^m(k) e^{im\phi} e^{ikz} I'_m(|k|\rho) K'_m(|k|a) \quad (3.29)$$

$$B_{\phi}(\mathbf{r}) = -\frac{\mu_0 a}{2\pi \rho} \sum_{m=-\infty}^{\infty} \int_{-\infty}^{\infty} \frac{k}{|k|} dk J_{\phi}^m(k) e^{im\phi} e^{ikz} m I_m(|k|\rho) K'_m(|k|a) \quad (3.30)$$

$$B_z(\mathbf{r}) = -\frac{\mu_0 a}{2\pi} \sum_{m=-\infty}^{\infty} \int_{-\infty}^{\infty} |k| dk J_{\phi}^m(k) e^{im\phi} e^{ikz} I_m(|k|\rho) K'_m(|k|a). \quad (3.31)$$

Again, exchanging the positions of  $\rho$  and  $a$  in the integrands yields the components of  $B$  outside the cylinder.

## 3.2 Magnetic shielding of cylindrical coils

The current confined to the surface of a cylinder of radius  $a$  produces a magnetic field both inside and outside the cylinder. To reduce the magnetic field to zero at

a finite radius outside the cylinder, let us introduce a second current of density  $j(b, \phi'', z'')$ , which is confined to the surface of a cylinder of infinite length and of radius  $b$ , where  $b > a$ . According to the result obtained in Section 3.1, the components of the magnetic field  $B$  outside the cylinder of radius  $b$ , generated by the currents on the surfaces of both cylinders, can be written as

$$B_\rho(\mathbf{r}) = \frac{i\mu_0}{2\pi} \sum_{m=-\infty}^{\infty} \int_{-\infty}^{\infty} k dk \left[ aJ_\phi^m(k)I'_m(|k|a) + bj_\phi^m(k)I'_m(|k|b) \right] e^{im\phi} e^{ikz} K'_m(|k|\rho) \quad (3.32)$$

$$B_\phi(\mathbf{r}) = -\frac{\mu_0}{2\pi\rho} \sum_{m=-\infty}^{\infty} m \int_{-\infty}^{\infty} \frac{k}{|k|} dk \left[ aJ_\phi^m(k)I'_m(|k|a) + bj_\phi^m(k)I'_m(|k|b) \right] e^{im\phi} e^{ikz} K_m(|k|\rho) \quad (3.33)$$

$$B_z(\mathbf{r}) = -\frac{\mu_0}{2\pi} \sum_{m=-\infty}^{\infty} \int_{-\infty}^{\infty} |k| dk \left[ aJ_\phi^m(k)I'_m(|k|a) + bj_\phi^m(k)I'_m(|k|b) \right] e^{im\phi} e^{ikz} K_m(|k|\rho) \quad (3.34)$$

where  $J_\phi^m(k)$  is given by Eq. 3.14, and  $j_\phi^m(k)$  is defined similarly as

$$j_\phi^m(k) = \frac{1}{2\pi} \int_{-\pi}^{\pi} d\phi'' e^{-im\phi''} \int_{-\infty}^{\infty} dz'' j_{\phi''}(b, \phi'', z'') e^{-ikz''}. \quad (3.35)$$

It can be seen from Eqs. 3.32, 3.33 and 3.34 that for the magnetic field everywhere outside the larger cylinder to be zero, it is required that

$$aJ_\phi^m(k)I'_m(|k|a) + bj_\phi^m(k)I'_m(|k|b) = 0 \quad (3.36)$$

for all  $m$ , which leads to

$$j_\phi^m(k) = -\frac{aI'_m(|k|a)}{bI'_m(|k|b)} J_\phi^m(k). \quad (3.37)$$

Using Eqs. 3.24 and 3.37 one obtains a relation between the Fourier transforms of  $J_{z'}(a, \phi', z')$  and  $j_{z''}(b, \phi'', z'')$ , namely

$$j_z^m(k) = -\frac{a^2 I'_m(|k|a)}{b^2 I'_m(|k|b)} J_z^m(k) \quad (3.38)$$

where  $J_z^m(k)$  is given by Eq. 3.15, and  $j_z^m(k)$  is defined as

$$j_z^m(k) = \frac{1}{2\pi} \int_{-\pi}^{\pi} d\phi'' e^{-im\phi''} \int_{-\infty}^{\infty} dz'' j_{z''}(b, \phi'', z'') e^{-ikz''}. \quad (3.39)$$

Eqs. 3.37 and 3.38 can be used to find the current distribution on the outer cylinder that will magnetically shield a coaxial cylindrical coil of smaller diameter which carries a current of known distribution.

Using Eqs. 3.29 to 3.31 and Eq. 3.37, the components of the magnetic field inside the shielded coil are found to be

$$B_\rho(r) = \frac{i\mu_0 a}{2\pi} \sum_{m=-\infty}^{\infty} \int_{-\infty}^{\infty} k dk J_\phi^m(k) e^{im\phi} e^{ikz} \cdot S_m(|k|, a, b) I_m'(|k|\rho) K_m'(|k|a) \quad (3.40)$$

$$B_\phi(r) = -\frac{\mu_0 a}{2\pi\rho} \sum_{m=-\infty}^{\infty} \int_{-\infty}^{\infty} \frac{k}{|k|} dk J_\phi^m(k) e^{im\phi} e^{ikz} \cdot m S_m(|k|, a, b) I_m(|k|\rho) K_m'(|k|a) \quad (3.41)$$

$$B_z(r) = -\frac{\mu_0 a}{2\pi} \sum_{m=-\infty}^{\infty} \int_{-\infty}^{\infty} |k| dk J_\phi^m(k) e^{im\phi} e^{ikz} \cdot S_m(|k|, a, b) I_m(|k|\rho) K_m'(|k|a) \quad (3.42)$$

where

$$S_m(|k|, a, b) = 1 - \frac{I_m'(|k|a) K_m'(|k|b)}{I_m'(|k|b) K_m'(|k|a)}. \quad (3.43)$$

It can be seen that if the factor  $S_m(|k|, a, b)$  is set to unity, Eqs. 3.40, 3.41 and 3.42 become Eqs. 3.29, 3.30 and 3.31, respectively. Since the radius  $b$  is assumed to be greater than the radius  $a$ , both  $I_m'(|k|a)/I_m'(|k|b)$  and  $K_m'(|k|a)/K_m'(|k|b)$  are less than one. Also, since  $I_m'(|k|a)/I_m'(|k|b)$  and  $K_m'(|k|a)/K_m'(|k|b)$  are positive, the factor  $S_m(|k|, a, b)$  falls between 0 and 1. Therefore, shielding a coil, while maintaining the same current distribution in it, reduces the magnetic field inside it. This is reasonable because the magnetic field generated by the current in the inner or primary coil is partially cancelled by that generated by the current in the outer or shielding coil. (We use the term *primary* and *shielding*,

respectively, when referring to the *inner* and *outer* coils. We use *shielded* when referring to the pair connected together.)

The factor  $S_m(|k|, a, b)$  varies with  $b$  for fixed  $k$  and  $a$ . If  $b$  is equal to  $a$ , *i.e.* the shielding coil coincides with the primary coil,  $S_m(|k|, a, b)$  becomes zero and the magnetic field vanishes everywhere in space. In this case, from Eqs.3.37 and 3.38 we know that the required current in the shielding coil has the same distribution as the current in the primary coil, but flows in the opposite sense. If one lets  $b$  go to infinity, which is equivalent to removal of the shielding coil, then  $S_m(|k|, a, b)$  goes to unity,  $j(b, \phi'', z'')$  becomes zero, and the magnetic field given by Eqs. 3.40, 3.41 and 3.42 is identical to that produced by the current in the primary coil as expected.

### 3.3 Minimization of the inductance of a cylindrical coil

In many MRI experiments, it is necessary to switch magnetic field gradients rapidly. The rise and fall times of a magnetic field gradient pulse depends on the ratio of the inductance  $L$  to the resistance  $R$  of the gradient coil which generates the gradient. Since  $R$  must be kept small to ease power supply requirement, the coil should have a low inductance.

In this section, analytical expressions for the inductances of unshielded and shielded coils will be derived. The optimal current density distribution, which minimizes the inductance of a coil and generates a desired magnetic field profile in a certain region, will then be found using the method of variation.

### 3.3.1 Inductance of an unshielded coil

The magnetic energy  $E$  due to a current of density  $\mathcal{J}(\rho, \phi, z)$  is given by

$$E = \frac{1}{2} \int \mathbf{A} \cdot \mathcal{J} \, dv \quad (3.44)$$

where  $\mathbf{A}$  is the vector potential, and the integration is over entire space. For a cylindrical coil where the current is confined to the surface of a cylinder of radius  $a$ , Eq. 3.44 reduces to

$$\begin{aligned} E &= \frac{1}{2} \int_{-\pi}^{\pi} d\phi \int_{-\infty}^{\infty} a \, dz \, \mathbf{A}(a, \phi, z) \cdot \mathbf{J}(a, \phi, z) \\ &= \frac{1}{2} \int_{-\pi}^{\pi} d\phi \int_{-\infty}^{\infty} a \, dz (A_{\phi} J_{\phi} + A_z J_z). \end{aligned} \quad (3.45)$$

On the other hand, for a coil of inductance  $L$ , the magnetic energy due to a total current  $I$  flowing into the coil is given by

$$E = \frac{1}{2} L I^2. \quad (3.46)$$

By equating the right sides of Eqs. 3.45 and 3.46, the inductance of a cylindrical coil of radius  $a$  is found to be given by

$$L = \frac{1}{I^2} \int_{-\pi}^{\pi} d\phi \int_{-\infty}^{\infty} a \, dz (A_{\phi} J_{\phi} + A_z J_z). \quad (3.47)$$

Using Eqs. 3.16, 3.17, 3.19, 3.20 and the recurrence relations for modified Bessel functions, Eqs. 3.25 to 3.28, Eq. 3.47 becomes

$$\begin{aligned} L &= -\frac{\mu_0 a^2}{I^2} \sum_{m=-\infty}^{\infty} \int_{-\infty}^{\infty} dk J_{\phi}^{-m}(-k) J_{\phi}^m(k) \\ &\quad \cdot \left[ I'_m(|k|a) K'_m(|k|a) + \frac{m^2}{k^2 a^2} I_m(|k|a) K_m(|k|a) \right] \\ &\quad + \frac{\mu_0 a^2}{I^2} \sum_{m=-\infty}^{\infty} \int_{-\infty}^{\infty} dk J_z^{-m}(-k) J_z^m(k) I_m(|k|a) K_m(|k|a). \end{aligned} \quad (3.48)$$

In deriving Eq. 3.48, use has also been made of the relations

$$\begin{aligned} \int_{-\pi}^{\pi} d\phi e^{i(m+m')\phi} &= 2\pi \delta_{m', -m} \\ \int_{-\infty}^{\infty} dz e^{i(k+k')z} &= 2\pi \delta(k' + k) \end{aligned}$$

where  $\delta_{m',-m}$  is equal to unity when  $m' = -m$  and is zero otherwise, and  $\delta(k' + k)$  is the  $\delta$ -function. By definition,  $J_\phi^{-m}(-k)$  and  $J_z^{-m}(-k)$  are the complex conjugates of  $J_\phi^m(k)$  and  $J_z^m(k)$ , respectively. Moreover,  $J_\phi^m(k)$  and  $J_z^m(k)$  are related by Eq. 3.24. Therefore, Eq. 3.48 can be simplified and becomes

$$L = -\frac{\mu_0 a^2}{I^2} \sum_{m=-\infty}^{\infty} \int_{-\infty}^{\infty} dk |J_\phi^m(k)|^2 I'_m(|k|a) K'_m(|k|a). \quad (3.49)$$

Turner's expression for the inductance of a cylindrical coil, namely

$$L = -\frac{\mu_0 a^2}{I^2} \sum_{m=-\infty}^{\infty} \int_{-\infty}^{\infty} dk |J_\phi^m(k)|^2 I'_m(ka) K'_m(ka), \quad (3.50)$$

differs from our expression in not taking the modulus of  $k$  in the Bessel functions. However, the modulus *must* be taken in order to evaluate  $K'_m$  in the expression for  $L$ . Eq. 3.49 can be used to compute the inductance of any coil formed by winding a wire on the surface of a cylinder, if the configuration of the wire is known.

### 3.3.2 Inductance of a shielded coil

Consider a cylindrical shielded coil, consisting of a primary cylindrical coil of radius  $a$  surrounded by a coaxial cylindrical shielding coil of radius  $b$ . We assume that the same current  $I$  flows into each coil. Using Eq. 3.47, the inductance of the shielded coil can be written as

$$\begin{aligned} L = & \frac{a}{I^2} \int_{-\pi}^{\pi} d\phi \int_{-\infty}^{\infty} dz [A_\phi^p(a, \phi, z) + A_\phi^s(a, \phi, z)] J_\phi(a, \phi, z) \\ & + \frac{a}{I^2} \int_{-\pi}^{\pi} d\phi \int_{-\infty}^{\infty} dz [A_z^p(a, \phi, z) + A_z^s(a, \phi, z)] J_z(a, \phi, z) \\ & + \frac{b}{I^2} \int_{-\pi}^{\pi} d\phi \int_{-\infty}^{\infty} dz [A_\phi^p(b, \phi, z) + A_\phi^s(b, \phi, z)] j_\phi(b, \phi, z) \\ & + \frac{b}{I^2} \int_{-\pi}^{\pi} d\phi \int_{-\infty}^{\infty} dz [A_z^p(b, \phi, z) + A_z^s(b, \phi, z)] j_z(b, \phi, z) \quad (3.51) \end{aligned}$$

where we have used  $A^p$  and  $A^s$ , respectively, to denote the vector potentials due to the currents in the primary and shielding coils. By regrouping terms on the

right hand side, Eq. 3.51 can be written as

$$\begin{aligned}
L &= \frac{1}{I^2} \int_{-\pi}^{\pi} a d\phi \int_{-\infty}^{\infty} dz \left[ A_{\phi}^p(a, \phi, z) J_{\phi} + A_z^p(a, \phi, z) J_z \right] \\
&+ \frac{1}{I^2} \int_{-\pi}^{\pi} b d\phi \int_{-\infty}^{\infty} dz \left[ A_{\phi}^s(b, \phi, z) j_{\phi} + A_z^s(b, \phi, z) j_z \right] \\
&+ \frac{1}{I^2} \int_{-\pi}^{\pi} a d\phi \int_{-\infty}^{\infty} dz \left[ A_{\phi}^s(a, \phi, z) J_{\phi} + A_z^s(a, \phi, z) J_z \right] \\
&+ \frac{1}{I^2} \int_{-\pi}^{\pi} b d\phi \int_{-\infty}^{\infty} dz \left[ A_{\phi}^p(b, \phi, z) j_{\phi} + A_z^p(b, \phi, z) j_z \right]. \quad (3.52)
\end{aligned}$$

The first two terms on the right hand side of Eq. 3.52 are, respectively, the self inductances of the primary and shielding coils,  $L_p$  and  $L_s$ , say, which can be written as

$$L_p = -\frac{\mu_0 a^2}{I^2} \sum_{m=-\infty}^{\infty} \int_{-\infty}^{\infty} dk |J_{\phi}^m(k)|^2 I'_m(|k|a) K'_m(|k|a) \quad (3.53)$$

$$L_s = -\frac{\mu_0 a^2}{I^2} \sum_{m=-\infty}^{\infty} \int_{-\infty}^{\infty} dk |J_{\phi}^m(k)|^2 \left[ \frac{I'_m(|k|a)}{I'_m(|k|b)} \right]^2 I'_m(|k|b) K'_m(|k|b) \quad (3.54)$$

using Eqs. 3.37 and 3.49. The last two terms on the right hand side of Eq. 3.52 are caused by coupling between the two coils. Using the method by which Eq. 3.49 was derived, one finds that these two terms can be expressed in the form

$$\frac{2\mu_0 a^2}{I^2} \sum_{m=-\infty}^{\infty} \int_{-\infty}^{\infty} dk |J_{\phi}^m(k)|^2 \left[ \frac{I'_m(|k|a)}{I'_m(|k|b)} \right]^2 I'_m(|k|b) K'_m(|k|b). \quad (3.55)$$

It can be seen that this expression is equal to  $-2L_s$ , so that the inductance of the complete shielded coil is given by

$$\begin{aligned}
L &= L_p - L_s \\
&= -\frac{\mu_0 a^2}{I^2} \sum_{m=-\infty}^{\infty} \int_{-\infty}^{\infty} dk |J_{\phi}^m(k)|^2 S_m(|k|, a, b) I'_m(|k|a) K'_m(|k|a) \quad (3.56)
\end{aligned}$$

where  $S_m(|k|, a, b)$  is given by Eq. 3.43. Thus, the inductance of the shielded coil is reduced because of the factor  $S_m(|k|, a, b)$  as compared to the inductance of the unshielded coil. As was shown earlier, the magnetic field in the shielded coil is similarly reduced by the presence of  $S_m(|k|, a, b)$  in Eqs. 3.40 to 3.42.

We note that the current distribution involved in the expressions for the magnetic field and inductance corresponds to closed loops on the surface of a cylinder, since they are based on Eq. 3.22. The problem of approximating a theoretical closed loop current distribution by a current flowing in series through several discrete paths which are not strictly closed, is discussed in Section 4.1.2.

### 3.3.3 Minimization of the inductance of a cylindrical coil

It remains to find the current density distribution in a cylindrical coil which has the minimum inductance and which generates the desired magnetic field profile (not necessarily a uniform gradient) within a volume of interest. Since only the longitudinal component of the magnetic field is important in MRI, we confine ourselves to specifying the values of  $B_z$  at a set of  $N$  points within the volume of interest, which is generally inside the coil. Thus we write

$$B_z(\rho_n, \phi_n, z_n) = B_n \quad (3.57)$$

where  $B_n$ ,  $n = 1, 2, \dots, N$ , are specified values, and the  $\rho_n$  are less than  $a$ , the inner radius of the coil.

We now need an expression which can be used to minimize the inductance subject to the condition 3.57. For this purpose, we define a functional  $\mathcal{F}[J_\phi^m(k), J_\phi^{-m}(-k)]$  by

$$\mathcal{F}[J_\phi^m(k), J_\phi^{-m}(-k)] = L - \frac{1}{I} \sum_{n=1}^N \lambda_n B_z(\rho_n, \phi_n, z_n) \quad (3.58)$$

where  $\lambda_n$  are known as Lagrange multipliers. In Eq. 3.58 we treat  $J_\phi^m(k)$  and its complex conjugate  $J_\phi^{-m}(-k)$  as two separate variables, which is something that Turner (1988) did not do in his derivation. The reason for doing this is that  $J_\phi^m(k)$  is, in general, a complex quantity, so its real and imaginary parts can be considered as independent variables. In other words,  $J_\phi^m(k)$  and its complex



conjugate  $J_\phi^{-m}(-k)$  can be varied independently (Morse and Feshbach 1953b, Landau and Lifshitz 1958).

For a shielded coil,  $B_z(\rho_n, \phi_n, z_n)$  and  $L$  are given by Eqs. 3.42 and 3.56, respectively. For the sake of symmetry, we first write Eq. 3.42 as follows

$$\begin{aligned}
B_z(\rho_n, \phi_n, z_n) = & -\frac{\mu_0 a}{4\pi} \sum_{m=-\infty}^{\infty} \int_{-\infty}^{\infty} |k| dk J_\phi^m(k) e^{im\phi_n} e^{ikz_n} \\
& \cdot S_m(|k|, a, b, ) I_m(|k|\rho_n) K'_m(|k|a) \\
& - \frac{\mu_0 a}{4\pi} \sum_{m=-\infty}^{\infty} \int_{-\infty}^{\infty} |k| dk J_\phi^m(k) e^{im\phi_n} e^{ikz_n} \\
& \cdot S_m(|k|, a, b, ) I_m(|k|\rho_n) K'_m(|k|a). \quad (3.59)
\end{aligned}$$

In the second term on the right hand side of Eq. 3.59, substituting  $-k$  for  $k$  and  $-m$  for  $m$ , noting that  $I_{-m}(x) = I_m(x)$  and  $K_{-m}(x) = K_m(x)$ , and using the identity 3.11, we write  $B_z(\rho_n, \phi_n, z_n)$  in the following symmetric form with respect to  $J_\phi^m(k)$  and its complex conjugate  $J_\phi^{-m}(-k)$

$$\begin{aligned}
B_z(\rho_n, \phi_n, z_n) = & -\frac{\mu_0 a}{4\pi} \sum_{m=-\infty}^{\infty} \int_{-\infty}^{\infty} |k| dk \left[ J_\phi^m(k) e^{im\phi_n} e^{ikz_n} \right. \\
& \left. + J_\phi^{-m}(-k) e^{-im\phi_n} e^{-ikz_n} \right] S_m(|k|, a, b, ) I_m(|k|\rho_n) K'_m(|k|a). \quad (3.60)
\end{aligned}$$

Substituting Eqs. 3.56 and 3.60 into Eq. 3.58 yields

$$\mathcal{F}[J_\phi^m(k), J_\phi^{-m}(-k)] = \sum_{m=-\infty}^{\infty} \int_{-\infty}^{\infty} dk F[J_\phi^m(k), J_\phi^{-m}(-k)] \quad (3.61)$$

where  $F[J_\phi^m(k), J_\phi^{-m}(-k)]$  is defined as

$$\begin{aligned}
F[J_\phi^m(k), J_\phi^{-m}(-k)] = & -\frac{\mu_0 a^2}{I^2} J_\phi^m(k) J_\phi^{-m}(-k) I'_m(|k|a) K'_m(|k|a) S_m(|k|, a, b) \\
& + \frac{\mu_0 a}{4\pi I} \sum_{n=1}^N |k| \left[ J_\phi^m(k) e^{im\phi_n} e^{ikz_n} + J_\phi^{-m}(-k) e^{-im\phi_n} e^{-ikz_n} \right] \\
& \cdot S_m(|k|, a, b) I_m(|k|\rho_n) K'_m(|k|a). \quad (3.62)
\end{aligned}$$

For  $\mathcal{F}[J_\phi^m(k), J_\phi^{-m}(-k)]$  to be a minimum, it is required that its first variation be zero, which leads to Euler's equations

$$\frac{\partial F}{\partial J_\phi^m(k)} = 0 \quad \text{and} \quad \frac{\partial F}{\partial J_\phi^{-m}(-k)} = 0. \quad (3.63)$$

Substituting Eq. 3.62 into Euler's equations, one obtains

$$-\frac{\mu_0 a^2}{I^2} J_\phi^{-m}(-k) S_m(|k|, a, l) I'_m(|k|a) K'_m(|k|a) + \frac{\mu_0 a}{4\pi I} \sum_{n=1}^N |k| e^{im\phi_n} e^{ikz_n} S_m(|k|, a, b) I_m(|k|\rho_n) K'_m(|k|a) = 0 \quad (3.64)$$

and

$$-\frac{\mu_0 a^2}{I^2} J_\phi^m(k) S_m(|k|, a, b) I'_m(|k|a) K'_m(|k|a) + \frac{\mu_0 a}{4\pi I} \sum_{n=1}^N |k| e^{-im\phi_n} e^{-ikz_n} S_m(|k|, a, b) I_m(|k|\rho_n) K'_m(|k|a) = 0. \quad (3.65)$$

Eqs. 3.64 and 3.65 both lead to the following expression for the optimal  $J_\phi^m(k)$

$$J_\phi^m(k) = \frac{|k|I}{4\pi I'_m(|k|a)} \sum_{n=1}^N \lambda_n e^{-im\phi_n} e^{-ikz_n} I_m(|k|\rho_n). \quad (3.66)$$

Substituting Eq. 3.66 back into Eq. 3.42 at the points at which the magnetic field was specified, we obtain

$$B_z(\rho_l, \phi_l, z_l) = -\frac{\mu_0 I}{8\pi^2} \sum_{n=1}^N \lambda_n \left[ \sum_{m=-\infty}^{\infty} \int_{-\infty}^{\infty} k^2 dk \frac{K'_m(|k|a)}{I'_m(|k|a)} \cdot I_m(|k|\rho_n) I_m(|k|\rho_l) S_m(|k|, a, b) e^{im(\phi_l - \phi_n)} e^{ik(z_l - z_n)} \right] \quad (3.67)$$

where  $l = 1, 2, \dots, N$ . The expression 3.67 contains a set of  $N$  simultaneous equations with  $N$  unknowns  $\lambda_n$ . Solving the simultaneous equations for  $\lambda_n$ , one can determine the current density  $J(a, \phi, z)$  and  $j(b, \phi, z)$  using Eqs. 3.16, 3.17, 3.24, 3.37 and 3.66.

It should be pointed out that Eqs. 3.66 and 3.67 are different from the corresponding expressions for the optimal  $J_\phi^m(k)$  and  $B_z(\rho_n, \phi_n, z_n)$  given by Turner (1988), namely

$$J_\phi^m(k) = \frac{kI}{4\pi I'_m(ka)} \sum_{n=1}^N \lambda_n e^{im\phi_n} e^{ikz_n} I_m(k\rho_n) \quad (3.68)$$

and

$$B_z(\rho_l, \phi_l, z_l) = -\frac{\mu_0 I}{8\pi^2} \sum_{n=1}^N \lambda_n \left[ \sum_{m=-\infty}^{\infty} \int_{-\infty}^{\infty} k^2 dk \frac{K'_m(ka)}{I'_m(ka)} \cdot I_m(k\rho_n) I_m(k\rho_l) S_m(k, a, b) e^{im(\phi_l + \phi_n)} e^{ik(z_l + z_n)} \right] \quad (3.69)$$

where

$$S_m(k, a, b) = 1 - \frac{I'_m(ka)K'_m(kb)}{I'_m(kb)K'_m(ka)}. \quad (3.70)$$

Firstly, Turner's expressions do not include the modulus of  $k$ . However, as noted earlier, the modulus must be taken in order to evaluate  $K'_m$  in the expression for  $B_z(\rho_l, \phi_l, z_l)$ . Secondly, the arguments of the exponential functions involving  $\phi_n$  and  $z_n$  in Eqs. 3.68 and 3.69 have the wrong sign. This stems from an unwarranted assumption that the  $J_\phi^m(k)$  are real. Nevertheless, Turner's expressions will give correct answers in cases where the desired magnetic field possesses certain spatial symmetry and provided the modulus of  $k$  is taken where necessary. For example, if the desired field profile is a uniform gradient in the  $x$  direction, Turner's expressions will give the correct current distribution and field gradient. If the desired field profile is a uniform gradient in the  $y$  or  $z$  direction, they will give the correct current distribution, but the gradient is of wrong sign.

To evaluate the inductance  $L$  of a shielded coil, one substitutes Eq. 3.66 back into Eq. 3.56 and obtains

$$L = -\frac{\mu_0 a^2}{I} \sum_{m=-\infty}^{\infty} \int_{-\infty}^{\infty} dk \left[ \frac{|k|I}{4\pi a I'_m(|k|a)} \right]^2 \sum_{n=1}^N \sum_{n'=1}^N \lambda_n \lambda_{n'} e^{im(\phi_n - \phi_{n'})} e^{ik(z_n - z_{n'})} \\ \cdot S_m(|k|, a, b) I_m(|k|\rho_n) I_m(|k|\rho_{n'}) I'_m(|k|a) K'_m(|k|a)$$

which can also be written as

$$L = \frac{1}{2I} \sum_{n=1}^N \lambda_n \left[ -\frac{\mu_0 I}{8\pi^2} \sum_{n'=1}^N \lambda_{n'} \sum_{m=-\infty}^{\infty} \int_{-\infty}^{\infty} k^2 dk \frac{K'_m(|k|a)}{I'_m(|k|a)} \right. \\ \left. \cdot I_m(|k|\rho_n) I_m(|k|\rho_{n'}) S_m(|k|, a, b) e^{im(\phi_n - \phi_{n'})} e^{ik(z_n - z_{n'})} \right]. \quad (3.71)$$

By comparing Eq. 3.71 with Eq. 3.67, it can be seen that the terms within the square brackets on the right hand side of Eq. 3.71 are simply equal to  $B_z(\rho_n, \phi_n, z_n)$ , the specified magnetic field at the point  $(\rho_n, \phi_n, z_n)$ , whose value is  $B_n$ . Therefore, the minimum inductance of the shielded coil is given by a very

simple expression, which is

$$L = \frac{1}{2I} \sum_{n=1}^N \lambda_n B_n. \quad (3.72)$$

Such an equation is not restricted to the shielded coil. It applies equally well to an unshielded coil, where the specified values of the magnetic field  $B_n$  and the current  $I$  are the same as for the shielded coil. In that case, the values of the Lagrange multipliers  $\lambda_n$  will be different.

### 3.4 Shielded gradient coils of minimum inductance

The results obtained in Section 3.3 are quite general. In this section, we apply the results to shielded coils which generate uniform magnetic field gradients.

#### 3.4.1 A longitudinal gradient coil of minimum inductance

The magnetic field generated by a longitudinal gradient coil is independent of the azimuthal angle  $\phi$ . Thus only the  $m = 0$  term exists in the expression 3.67, and the axial component of the current density vanishes according to Eq. 3.24. Since the axial component of the magnetic field is antisymmetric about the  $z = 0$  plane, the azimuthal component of the current density must also be antisymmetric about that plane. That is, the current density is an odd function of  $z$ . The Fourier transform of the current density must have the same symmetry property with respect to  $k$ . By taking the above constraints into account, it follows from the expressions 3.67 and 3.66, respectively, that the magnetic field at a specified point within the coil is given by

$$B_z(\rho_l, \phi_l, z_l) = \frac{\mu_0 I}{4\pi^2} \sum_{n=1}^N \lambda_n \int_0^\infty k^2 dk \frac{K_1(ka)}{I_1(ka)} S_0(k, a, b) \cdot I_0(k\rho_l) I_0(k\rho_n) \sin kz_l \sin kz_n. \quad (3.73)$$

and the Fourier transform of the current density in the primary coil is given by

$$J_{\phi}^0(k) = -\frac{i|k|I}{4\pi a I_1(|k|a)} \sum_{n=1}^N \lambda_n I_0(|k|\rho_n) \sin kz_n. \quad (3.74)$$

The Fourier transform of the current density in the shielding coil,  $j_{\phi}^0(k)$  can be found using Eqs. 3.37 and 3.74. The current densities in the primary and shielding coils are found by inverse Fourier transformation of  $J_{\phi}^0(k)$  and  $j_{\phi}^0(k)$ , respectively.

While it is possible to design a longitudinal gradient coil merely by specifying the magnetic field at a set of points along the  $z$ -axis (where  $x = y = 0$ ), a more uniform gradient should be obtained by specifying the magnetic field at points on the surfaces of two, or more, cylinders coaxial with the coil (Turner 1988).

### 3.4.2 A transverse gradient coil of minimum inductance

Since the magnetic field associated with a uniform transverse gradient is directly proportional to  $x$  for the  $x$  gradient or to  $y$  for the  $y$  gradient, and since  $x = \rho \cos \phi$  and  $y = \rho \sin \phi$ , only the  $m = \pm 1$  terms exist in the expression 3.67. We shall derive expressions for the magnetic field at a specified point within the coil and for the Fourier transform of the current density for an  $x$  gradient coil. A  $y$  gradient coil can be obtained simply by rotating the  $x$  gradient coil through  $90^\circ$  about  $z$ -axis.

The axial component of the magnetic field generated by the coil in the region enclosed by the coil is directly proportional to  $x$ , hence to  $\cos \phi$ . By taking the symmetry property about the  $z$  coordinate of the magnetic field, the expressions 3.66 and 3.67 become

$$J_{\phi}^{\pm 1}(k) = \frac{|k|I}{4\pi a I_1'(|k|a)} \sum_{n=1}^N \lambda_n I_1(|k|\rho_n) \cos \phi_n \cos kz_n \quad (3.75)$$

and

$$B_z(\rho_l, \phi_l, z_l) = -\frac{\mu_0 I}{2\pi} \cos \phi_l \sum_{n=1}^N \lambda_n \cos \phi_n \int_0^\infty k^2 dk \frac{K_1'(ka)}{I_1'(ka)} S_1(k, a, b) \cdot I_1(k\rho_l) I_1(k\rho_n) \cos kz_l \cos kz_n. \quad (3.76)$$

The Fourier transform of the axial component of the current density is obtained using Eq. 3.24, the result being

$$J_z^{\pm 1}(k) = \mp \frac{|k|}{4\pi a^2 k I_1'(|k|a)} \sum_{n=1}^N \lambda_n I_1(|k|\rho_n) \cos \phi_n \cos kz_n. \quad (3.77)$$

It can be shown from Eqs. 3.75 and 3.77 that the azimuthal component of the current distribution  $J_\phi$  is an even function of both  $z$  and  $\phi$  but changes sign with respect to the transformation  $\phi$  to  $\pi - \phi$ . On the other hand,  $J_z$  is an odd function of both  $z$  and  $\phi$ , and is invariant with respect to the transformation  $\phi$  to  $\pi - \phi$ . It follows that a transverse gradient coil consists of four identical quadrants connected in such a way that the current flows in the opposite sense in adjacent quadrants when viewed from outside the coil.

While it is possible to design an  $x$  gradient coil merely by specifying the magnetic field at a set of points along the  $x$ -axis (where  $y = z = 0$ ), a more uniform gradient should be obtained by specifying the magnetic field at points on the surfaces of two, or more, cylinders coaxial with the coil (Turner 1988).

## Chapter Four

# DESIGN AND CONSTRUCTION OF A SHIELDED TRANSVERSE GRADIENT COIL

### 4.1 Design considerations

#### 4.1.1 Coil dimensions

The shielded transverse gradient coil was designed to be installed in a 40 cm bore, 2.35 T superconducting magnet, which forms part of an animal-size NMR imaging system manufactured by Bruker Medizintechnik in Silberstriefen, Germany. This system is part of the University of Alberta's *in vivo* NMR facility and is located in the University of Alberta Hospital. Existing shim coils and unshielded gradient coils with an inner diameter (ID) of 35 cm are situated in the magnet bore. Since the shim coils must be left in place to provide the required main field homogeneity, the new  $x$ ,  $y$  and  $z$  shielded gradient coils must fit inside a diameter of 35 cm. The coil that was built was the innermost one which we call the  $x$  gradient coil. To allow room for the  $y$  and  $z$  gradient coils which will be constructed later, the diameter of the  $x$  shielding coil was chosen to be 31.6 cm. As the ratio of the radius of the primary coil to the radius of the shielding coil approaches unity, the magnetic field within the coil approaches zero because of the opposing magnetic fields generated by the currents in the two coils. That would cause the gradient to vanish. On the other hand, if the radius of the primary coil is much less than the radius of the shielding coil, there would be little available sample space. In order to be able to accommodate animals as large as cats, without unduly sacrificing gradient strength, the diameter of the  $x$  primary coil was chosen to be 23.6 cm.

#### 4.1.2 Selection of the type of conducting paths

As was stated in Section 2.5, the resolution of an NMR image is limited by the strength of the magnetic field gradient, a large magnetic field gradient being needed to obtain a detailed image. In practice, the usable gradient strength generated by a gradient coil is largely dependent upon the power dissipated within it by Joule heating. This is because excessive temperatures cannot be tolerated and because the size of the power supply is largely determined by the power dissipation in the coil. Thus, a useful "figure of merit" for a gradient coil is the gradient strength which corresponds to a fixed power dissipation within it. For a coil with a given number of turns, the gradient strength is proportional to the current and so it is advantageous to reduce the resistance of the coil, in order to achieve a higher current for the same Joule heating.

Since the theoretical current distribution in the primary coil is confined to the surface of a cylinder, the equation of continuity (Eq. 3.22) implies that the current flows in closed loops on the surface of the cylinder. It follows that the current distribution in each quadrant has a well defined center and a well defined edge which may extend out to infinity in some directions. In practice, it is necessary to approximate this current distribution by discrete current paths and a convenient way of achieving this is to connect these discrete paths in series. This can be done by winding a coil with wire, which is essentially everywhere parallel to the required distribution of the current flow, the separation between adjacent turns being such as to produce the required current distribution.

Copper is an obvious choice for the conducting material of the coil, because of its low resistivity. The resistance can be reduced by using wire of large diameter. However, there is a limit to the diameter of wire that can be used since, if this is excessive, valuable sample space will be lost.



If the number of turns of wire,  $\mathcal{N}$ , is varied while keeping the wire diameter fixed, it can be shown that the “figure of merit” is proportional to  $\sqrt{\mathcal{N}}$ . The optimal coil design using wire therefore requires as many turns as possible to be wound until adjacent turns touch in the region of maximum theoretical current density.

Since the theoretical current density is far from uniform, there will be many areas on the cylinder which are not occupied by the wire. It is obvious therefore that constructing the coil out of a continuous sheet which is cut to provide the same number of turns will have a lower resistance than will a coil wound with wire whose diameter is equal to the thickness of the sheet. It was therefore decided to construct the coil using copper sheets of uniform thickness, rolled on to a cylindrical former and cut to provide the required conducting paths.

The dependence of the “figure of merit” on the number of turns is different for a coil cut out of a uniform sheet than it is for a coil wound with wire. The resistance of the coil is proportional to  $\mathcal{N}^2$ , provided the cuts take up negligible area and skin depth effects are ignored. (The length of the conducting path is proportional to  $\mathcal{N}$ , whereas the width is inversely proportional to  $\mathcal{N}$ .) Thus, the current  $I$ , which flows in each turn, will vary as  $1/\mathcal{N}$  for a fixed power dissipation in the coil. It can be seen from Eqs. 3.29 to 3.31 that the magnetic field and hence gradient generated by the coil is proportional to  $J_\phi^m(k)$ , the Fourier transform of  $J_\phi(a, \phi, z)$ , for a given form of current distribution. However, the current density  $J(a, \phi, z)$  is related to  $I$  by the relation

$$\left| \int J(a, \phi, z) \cdot (\mathbf{n} \times d\mathbf{r}) \right| = \mathcal{N}I \quad (4.1)$$

where the line integral is taken from the center of the pattern of the quadrant to the edge, and  $\mathbf{n}$  is a unit vector perpendicular to the surface in which the current flows. Thus, the gradient generated by the coil is proportional to  $\mathcal{N}I$ . But since

the current  $I$  is inversely proportional to  $\mathcal{N}$  for a fixed power dissipation, the “figure of merit” is *independent* of the number of turns.

It is also interesting to examine the dependence of the  $L/R$  ratio of a gradient coil, constructed out of a sheet, on the number of turns  $\mathcal{N}$ . It can be seen from Eq. 3.49 that the inductance is proportional to  $(J_{\phi}^m(k)/I)^2$ , which, from Eq. 4.1, is proportional to  $\mathcal{N}^2$ . Thus,  $L/R$  is independent of  $\mathcal{N}$ .

An often quoted property of a gradient coil is its coil efficiency, namely the gradient generated by unit current. Since the gradient is proportional to  $\mathcal{N}I$ , it follows that the coil efficiency is proportional to  $\mathcal{N}$ .

To summarize, changing the number of turns constructed out of a sheet will change the coil efficiency and the resistance of the coil, which in turn may affect the choice of gradient power supply. However, it does not affect the gradient which corresponds to a given power dissipation, nor does it affect the  $L/R$  ratio, which determines the rise and fall times of gradient pulses.

It may appear, therefore, that the choice of the number of turns is arbitrary. However, that is not the case because other factors need to be taken into account. The number of turns cannot be very small since, in that case, the actual discrete current distribution would be a poor approximation to the continuous theoretical distribution. Moreover, because of the skin effect, high frequency components of the current will tend to flow around the outer edge of each conducting path, instead of being uniformly distributed across it. On the other hand, the number of turns should not be too large since, in that case, excessive area will be taken up by the cuts. Moreover, machining the cuts would be very time consuming and expensive.

As a compromise, the number of turns in each quadrant of our primary coil was chosen to be twenty-two, which corresponds to a minimum width of

about 5 mm for the conducting paths. Two quadrants of our primary coil are shown in Figure 4.1, where the curves indicate the locations of the spiral cuts which define the conducting paths. The angled cuts shown in the figure are the means whereby the loops are connected in series.

The four quadrants of the primary coil are connected in series, to ensure that the same current flows in all of them. As discussed in Section 3.4.2, the quadrants must be connected in such a way that the current flows in the opposite sense in adjacent quadrants when viewed from outside the coil.

If all four quadrants of the shielding coil are connected in series, and the primary and shielding coils are connected in series with each other, there will be only eleven turns in each quadrant of the shielding coil, corresponding to a minimum width of about 11 mm because of the lower current density needed in that coil. To provide a better approximation to the desired current distribution, the two halves of the shielding coil (on either side of the cylinder) are connected in parallel, thereby increasing the number of turns to 22 and reducing the minimum width of the conducting paths to 5.5 mm. We note that in this case the coil has to be symmetric, otherwise the same current may not flow in all quadrants.

The locations of the cuts in the primary and shielding coils were kindly provided by Turner (1989) in the form of a series of closely spaced coordinates  $(a\phi, z)$  and  $(b\phi, z)$ . In order to avoid an oscillatory behavior in the current density, the Fourier transform of the current density was apodized with a gaussian function of the form,  $\exp(-2k^2h^2)$  (Turner 1988), where  $h$  is chosen to give the appropriate degree of apodization.

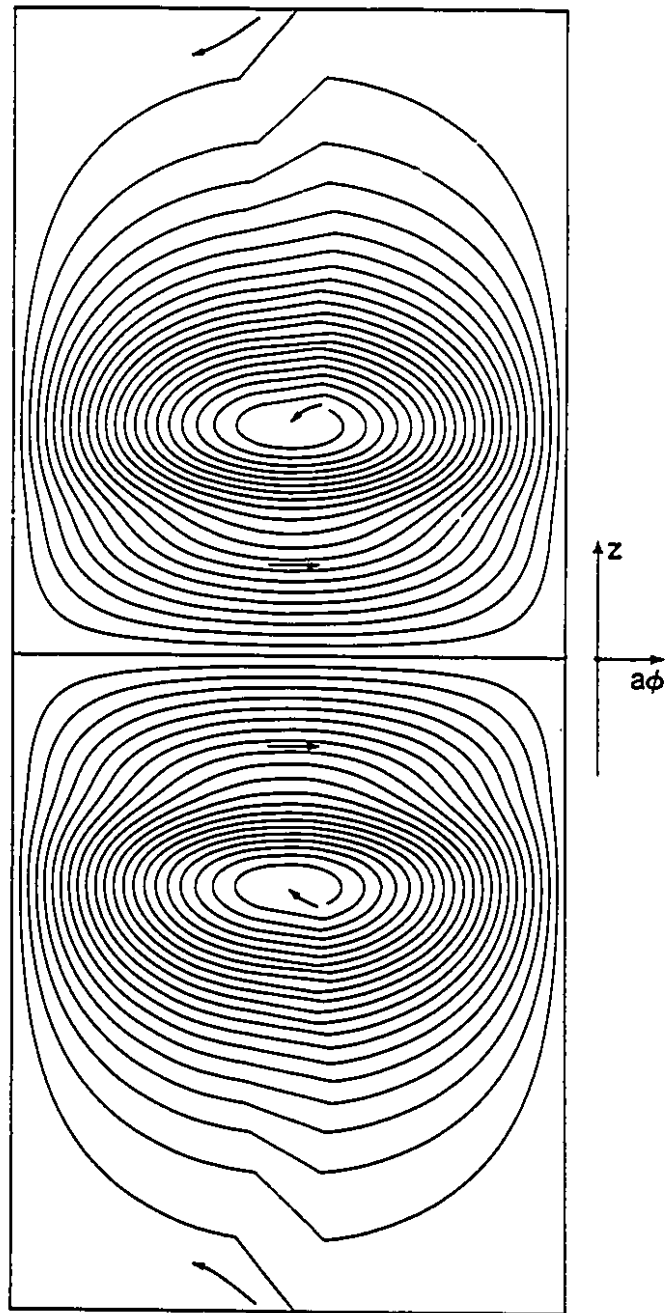


Figure 4.1: Pattern showing the locations of the spiral cuts in two quadrants of the primary coil. For clarity, the origin of the coordinate system is displaced from the center of the pattern to one side. The currents must flow in the opposite sense in adjacent quadrants, as indicated by the arrows.

### 4.1.3 Mechanical stresses on the coil and former

When the gradient coil is installed in the 2.35  $T$  main magnet, the conductors comprising the coil will experience a mechanical force per unit length given by  $I\hat{l} \times B$ , where  $\hat{l}$  is the unit vector indicating the direction of the current  $I$  and  $B$  is 2.35  $T$  in the  $z$  direction. The force will be in the radial direction, either inward or outward depending upon the direction of the current. It can be seen in Figure 4.2 that the forces are distributed in such a way as to bend the primary and shielding coils in the opposite sense. However, the forces on the shielding coil are substantially smaller than those on the primary coil because of the smaller current distribution, so that cancellation of the stresses cannot be achieved by firmly bonding the primary and shielding coils together.

If the current  $I$  is 200  $A$  (the maximum value anticipated), the maximum force per unit length on the conducting paths will be 470  $N/m$ . Given that the minimum width of the conducting paths is about 4  $mm$  because of the width of the cuts, the maximum force per unit area on the conducting paths will be about  $1.2 \times 10^5 N/m^2$ . As can be seen in Figure 4.2, the force will tend to pull the conductors away from the former in some places. In others, the former will be compressed.

Because of the large mechanical stresses, an adhesive with high mechanical strength must be used to bond the copper conductors to the formers of the primary and shielding coils. In addition, the formers should be mechanically strong enough to withstand the stresses. It was therefore decided that the cylindrical formers would be made of fiberglass, 6  $mm$  thick. Since the current in the gradient coil is pulsed, the force acting on the coil will change rapidly, tending to cause a mechanical vibration. Such a vibration would result in an oscillation of the field gradient, which would in turn affect the NMR signal. However, it is felt that 6  $mm$  thick fiberglass formers should not vibrate unduly. If they

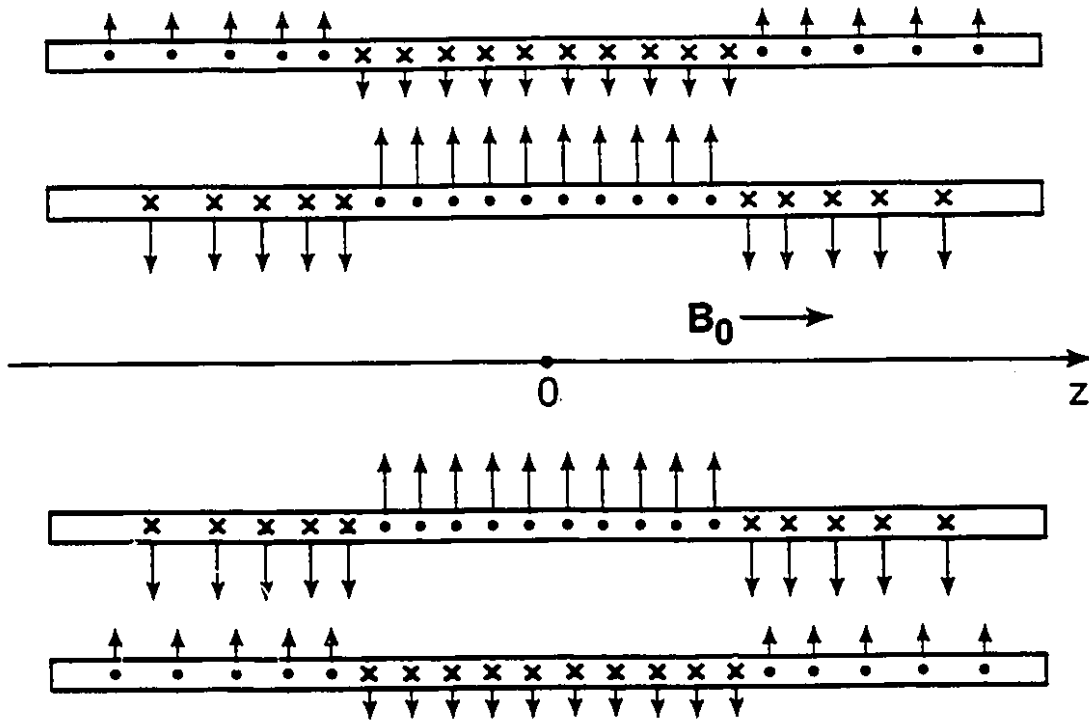


Figure 4.2: Cross section of the shielded transverse gradient coil in the  $x$ - $z$  plane, showing the mechanical forces acting on it when installed in the magnet. The dots indicate the current flowing out of the paper, while the symbol ( $\times$ ) indicates the current flowing into the paper. The arrows indicate the direction of the forces.

did, supports would have to be placed at appropriate locations to reduce the vibration.

#### 4.1.4 Estimate of the temperature rise in the coil due to Joule heating

It is anticipated that the  $y$  and  $z$  gradient coils will be bonded to the outside of the  $x$  gradient coil, each coil being separated by a 4 mm thickness of fiberglass and adhesive. Since each coil is 2 mm thick, and since the innermost or  $x$  gradient coil is bonded to a 6 mm thick fiberglass former, we consider a worst case scenario in which a conductor is embedded 19 mm deep in fiberglass, and can only lose heat by conduction in one direction through the 19 mm of fiberglass.

If a round wire of diameter  $D$  is embedded with its center at a depth  $d$  in a semi-infinite insulating slab, the rate of dissipation of heat per unit length of wire,  $q$ , is related, in the steady state, to the temperature  $T_H$  at the surface of the wire and the temperature  $T_L$  at the surface of the slab, by the relation (Kreith and Bohn 1986)

$$q = S\kappa(T_H - T_L). \quad (4.2)$$

Here  $\kappa$  is the thermal conductivity of the insulating medium and  $S$  is a dimensionless shape factor given by

$$S = 2\pi \left[ \cosh^{-1}(2d/D) \right]^{-1}. \quad (4.3)$$

While this expression refers to plane geometry, it should be a reasonable approximation for our cylindrical geometry. Since our copper conductors are 2 mm thick and the narrowest width of the conducting paths is 4 mm, the smallest cross sectional area is 8 mm<sup>2</sup>. We therefore assume an effective diameter of 3 mm. Substituting  $d = 19$  mm and  $D = 3$  mm into Eq. 4.3, one finds that the shape factor  $S$  is 1.9.

The rate of heat dissipated per unit length  $q$  can be calculated using the equation

$$q = I^2 r \quad (4.4)$$

where  $r$  is the resistance per unit length of the wire, which is  $2.5 \times 10^{-3} \Omega/m$  if the resistivity is  $2.0 \times 10^{-8} \Omega \cdot m$  (the resistivity of copper at a temperature of  $60^\circ C$ ). For the power supply which will be used to drive the shielded gradient coils, the maximum continuous current delivered is 90 A. Using Eq. 4.4 we find that  $q$  for such a current is 20 W/m.

For fiberglass, which was used as the material of the formers of our coil, the thermal conductivity  $\kappa$  is about  $0.25 \text{ W/m}^\circ C$ . Substituting the values of  $\kappa$ ,  $S$  and  $q$  into Eq. 4.2, and assuming that  $T_L$  is equal to  $25^\circ C$ , we find the temperature at the surface of the wire,  $T_H$ , to be  $68^\circ C$ . Since the turns of each coil are close to one another, the actual temperature on the surface of the copper sheets in the coil will probably be higher than the calculated value, and could well approach  $100^\circ C$ . Fiberglass can easily withstand such temperatures, but many adhesives do not. It is therefore important to choose an adhesive that has good high temperature properties.

## 4.2 Construction of the coil

Cold-rolled, hard-temper copper was used in sheet form to construct the coil, because it can be machined more easily than other varieties of copper. Each quadrant of the primary coil consisted of a 432 mm by 369 mm by 3.2 mm (17" by 14.5" by (1/8)") sheet, which was held flat on a vacuum table on a vertical CNC milling machine. The required pattern was milled to a depth of 2.54 mm (0.1") using 1.6 mm ((1/16)") diameter solid two-flute tungsten carbide end mill cutters (#SEM-062-2), thereby leaving a residual thickness of 0.63 mm (0.025") of copper at the bottom of each groove. Each quadrant of the shielding coil was



similarly prepared by milling the required pattern in a 535 *mm* by 495 *mm* by 3.2 *mm* (21.1" by 19.5" by (1/8)") sheet of copper.

Each quadrant of the primary coil was sandwiched between two sheets of #12 gauge (2.75 *mm*, 0.11" thick) steel satincoat and rolled into a semi-cylinder of radius 118 *mm* (4.65") on a hydraulic pressure roller located in the Technical Services Fabrication Shop. The purpose of the steel was to ensure that the copper did not buckle at the grooves during the rolling process. Each quadrant of the shielding coil was similarly rolled into a semi-cylinder of radius 158 *mm* (6.22").

Copper leads, 100 *mm* by 10 *mm* by 2 *mm*, were welded to the outer edges of two quadrants to provide input and output connections to the primary coil. Two copper collars, 6 *mm* (0.236") in diameter and 4 *mm* (0.157") long, were welded to the inner surfaces of the other two quadrants, near the outer edges to allow electrical connection to be made between the two halves of the coil. Identical copper collars were also welded to the centers of the spiral pattern on the inner surfaces of all four quadrants to allow connection to be made between the quadrants in each half of the coil. In case of the shielding coil, two copper collars were welded to the inner surface of each quadrant, one at the center and another near the outer edge, to allow the quadrants on each side to be connected in series and the two sides to be connected in parallel.

The cylindrical former of the primary coil was a fiberglass tube, manufactured by the Triple M Fiberglass Co. in Edmonton, which was turned down to a thickness of 6 *mm* (0.236") and an outer diameter (OD) of 232 *mm* (9.14"). The cylindrical former for the shielding coil, made by the same company, was similarly turned down to a thickness of 6 *mm* (0.236") and an OD of 314 *mm* (12.36"). Four longitudinal grooves and one circumferential groove of 6 *mm* (0.236") wide and 2.1 *mm* (0.084") deep were machined on the inner surface of

each former to accommodate rectangular copper leads, 6 mm (0.236") wide and 1.6 mm ((1/16)") thick, which connect the various quadrants of each coil. Holes were drilled through each former to accommodate the 6 mm (0.236") diameter copper collars referred to above.

The primary coil was the first to be assembled. The copper quadrants and formers were degreased using a solution of detergent, and then washed with acetone or toluene. Because of the strength tests described in Section 5.1, the copper quadrants were immersed in an etching solution for 1 to 1.5 minutes, rinsed in cold deionized water immediately after being etched, and then dried with compressed air (Mahoney 1990). The etching solution consists of 15 parts by weight (*pbw*) of 42% aqueous FeCl<sub>2</sub> solution, 30 *pbw* of concentrated HNO<sub>3</sub> (*s.g.* 1.41) and 197 *pbw* of deionized water. PC-7 epoxy adhesive, chosen on the basis of tests described in Chapter Five, was applied to the outside of the former and the inside of the copper quadrants, care being taken to fill all the grooves. The quadrants were then clamped into position on the former using flexible hose-clamps, until the adhesive had cured.

The primary coil was then placed on a lathe and the excess copper was removed to expose the grooves. Some of the copper was ground off using a power driven belt-sander. However, it was found that the quadrants of the primary coil were "out of round" by up to about 1 mm, because of an uneven application of the PC-7 epoxy adhesive and because the flexibility of the hose-clamps. Thus, a substantial amount of copper had to be removed by hand filing, a time-consuming process.

To avoid similar problems with the shielding coil, several circumferential rows of nylon spacers were screwed into the outer surface of the fiberglass former so that they protruded 0.76 mm (0.03") above the surface of the former, this being judged to be the optimum thickness of the epoxy layer. Since PC-7 epoxy is

very viscous, several equally spaced 1.6 mm ((1/16)') diameter relief holes were drilled through the fiberglass former to allow excess epoxy to flow away from the bond area. PC-7 epoxy adhesive was then spread uniformly on the outer surface of the former and the inner surface of the copper quadrants. The quadrants were clamped into position using rigid cylindrical aluminum clamps which forced the quadrants on to the spacers. This procedure ensured coaxial geometry so that the outer surface of the shielding coil was almost exactly circular. That, in turn, allowed the excess copper to be ground off by the power driven belt-sander.

Finally, the leads were glued into the grooves on the inside of the formers and were soft-soldered to the copper collars to complete the electrical connections of the coils.

Two acrylic rings were constructed to form spacers which would maintain a coaxial geometry of the primary and shielding coils.

A photograph of the assembled shielded gradient coil is shown in Figure 4.3.

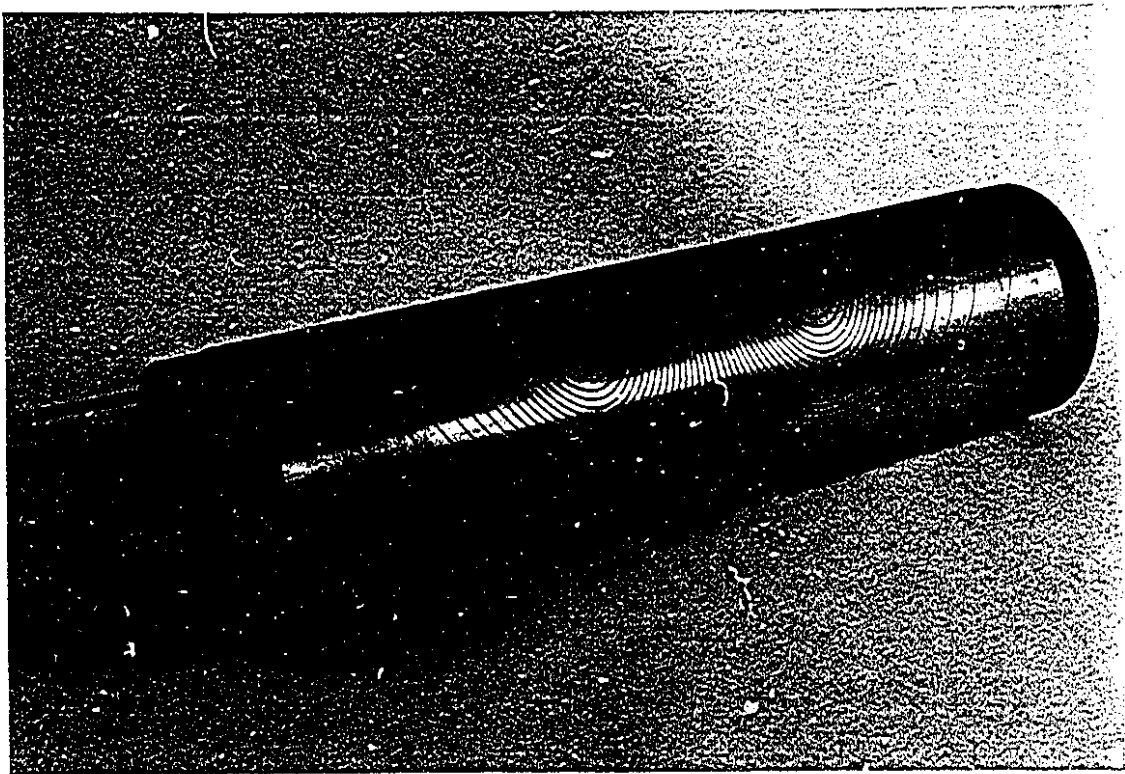


Figure 4.3: A photograph of the shielded transverse gradient coil.

## Chapter Five

# TESTING OF THE SHIELDED TRANSVERSE GRADIENT COIL

### 5.1 Selection of epoxy for bonding copper and fiberglass

The mechanical strength of bonded joints between copper and fiberglass was measured using a 50,000 *lb* universal test machine located in the Department of Mechanical Engineering at the University of Alberta. A tested set consisted of flat copper and fiberglass plates bonded over an area of  $6.45 \times 10^{-3} \text{ m}^2$  (10 square inches).

The surfaces of the fiberglass and copper plates were prepared by abrading with coarse sandpaper, rinsing with water, and then degreasing with toluene or acetone. Immediately after surface preparation, fiberglass and copper plates were bonded using each of the following five epoxy adhesives in turn: K-POXY, PC-7, 83HA4, DEVCON-F and ARALDITE. The fiberglass was bolted firmly to the base of the test machine and the copper was pulled upward slowly until the bond was destroyed. The maximum strength of the bond was taken to be the maximum force registered by the machine divided by the bonded area.

DEVCON-F and 83HA4 were tested once, and the corresponding maximum strengths of the bonded joints were  $2.6 \times 10^5 \text{ N/m}^2$  and  $3.4 \times 10^5 \text{ N/m}^2$ . ARALDITE was tested twice, the maximum strengths being  $2.0 \times 10^5 \text{ N/m}^2$  and  $3.5 \times 10^5 \text{ N/m}^2$  for the two tests. The maximum strengths of the K-PCXY bonded joints varied widely in nine tests, ranging from  $1.3 \times 10^5 \text{ N/m}^2$  to  $6.1 \times 10^5 \text{ N/m}^2$ . In all these cases, the failure of the bond occurred at the epoxy and copper interface. When the surface of the copper was sanded smooth and

then etched as described in Section 4.2 instead of being abraded, the strengths of two K-POXY bonded joints were  $5.5 \times 10^5 \text{ N/m}^2$  and  $6.1 \times 10^5 \text{ N/m}^2$ . However, when heated at  $120^\circ\text{C}$  for 24 hours before being tested, two other similar K-POXY bonded joints had low strengths, values of  $2.1 \times 10^5 \text{ N/m}^2$  and  $2.3 \times 10^5 \text{ N/m}^2$  being found. Failure again occurred at the epoxy to copper interface.

Bonds made with PC-7 epoxy were consistently strong for the two surface preparation procedures and for different thermal treatments. Table 5.1 gives the maximum strengths of the PC-7 epoxy bonded joints. In the first three tests, the copper was abraded and cleaned as described earlier. In the fourth and fifth tests, the surface preparation procedure was the same except that the bonds were heated at  $90^\circ\text{C}$  for 24 hours before being tested. In the last two tests, the copper plates were etched using the etching solution described in Section 4.2, and the bonds were heated at  $120^\circ\text{C}$  for 24 hours before being tested. In all bonds made with PC-7 epoxy, failure occurred due to separation of the fiberglass layers, and not at the epoxy to copper interface.

It can be seen that the values of the maximum strength in Table 5.1 are at least 3.6 times greater than the maximum stress on the copper conductor calculated in Section 4.1.3. It is concluded that the PC-7 epoxy is by far the best of the adhesives tested for bonding the copper quadrants to the fiberglass formers in our coil.

## 5.2 Measurement of the electrical resistance of the shielded coil

The electrical resistances of the primary coil alone, the shielding coil alone and the complete shielded coil were measured, in turn, by passing a DC current of approximately 4 A through them and measuring the voltage developed using a

Table 5.1: Mechanical strength of the PC-7 epoxy bonded joint between copper and fiberglass. In Tests 1 to 5, the surfaces of the copper plates were abraded with sandpaper, while in Tests 6 and 7 the copper plates were etched. Before being tested, the bonds were heated for 24 hours at 90°C for Tests 4 and 5, and at 120°C for Tests 6 and 7.

| Test | Maximum Strength of the PC-7<br>Epoxy Bonded Joint ( $10^5 N/m^2$ ) |
|------|---|
| 1    | 5.0   |
| 2    | 4.3   |
| 3    | 4.5   |
| 4    | 4.5   |
| 5    | 5.0   |
| 6    | 4.3   |
| 7    | 5.5   |

four-terminal method to avoid errors due to the resistance of connecting leads. To avoid errors due to thermal EMF's, measurements were repeated with the direction of the current reversed.

The results of measurements on the resistances of the primary coil alone, the shielding coil alone and the complete shielded coil are presented in Table 5.2.

Table 5.2: Resistances of the primary coil alone, the shielding coil alone and the complete shielded coil. The estimated errors in each case are  $\pm 0.1 \text{ m}\Omega$ .

|                          | Primary coil | Shielding coil | Shielded coil |
|--------------------------|--------------|----------------|---------------|
| Resistance ( $m\Omega$ ) | 83.3         | 23.0           | 115.9         |

As described in Section 4.2, the coils were constructed by grinding off a thin layer of copper until the milled grooves were exposed. The uniformity of the grinding process was checked by measuring the resistance of each quadrant in the primary and shielding coils. The results are given in Table 5.3. It can be seen that the resistances of the individual quadrants in each coil are in quite good agreement with each other, showing that the quadrants are of fairly uniform thickness.

The resistances of the two branches of the shielding coil including the leads, which are connected in parallel, were also measured and those results are given in Table 5.4. The resistances of the two branches of the shielding coil are essentially the same, indicating that any errors arising from different currents flowing in the two branches of the shielding coil should be very small.



Table 5.3: Resistances of individual quadrants of the primary and shielding coils. In each coil, quadrants 1 and 3 are on the same side of the former, while quadrants 2 and 4 are on the other side and opposite, respectively, to quadrants 1 and 3. The estimated errors are  $\pm 0.1 \text{ m}\Omega$ .

|          | Resistance ( $m\Omega$ ) |                |
|----------|--------------------------|----------------|
| Quadrant | Primary coil             | Shielding coil |
| 1        | 19.2                     | 21.3           |
| 2        | 19.4                     | 22.0           |
| 3        | 19.8                     | 20.6           |
| 4        | 18.9                     | 20.3           |

Table 5.4: Resistances of the two branches of the shielding coil. Branch 1 consists of quadrants 1 and 3, and branch 2 consists of quadrants 2 and 4. The estimated errors are  $\pm 0.1 \text{ m}\Omega$ .

| Branch | Resistance ( $m\Omega$ ) |
|--------|--------------------------|
| 1      | 45.8                     |
| 2      | 45.9                     |

### 5.3 Measurement of the inductance and AC resistance of the shielded coil

The inductance  $L$  and the AC resistance  $R_L$  of the shielded coil were measured by passing a known AC current  $I$  of frequency  $\nu$  through the coil and a resistance  $R$  connected in series with it, as shown in Figure 5.1. The voltage  $V$  developed across the whole circuit was fed into an EG&G 5208 lock-in analyzer and the voltage  $V_{ref}$  developed across the resistance  $R$  was used as the reference voltage for the analyzer. The inductance  $L$  and the AC resistance  $R_L$  were then found from the relations

$$L = \frac{1}{2\pi\nu} \frac{V}{I} \sin \theta \quad (5.1)$$

$$R_L = \frac{V \cos \theta - V_{ref}}{I} \quad (5.2)$$

where  $\theta$  is the phase difference between  $V$  and  $V_{ref}$  as measured by the lock-in analyzer. A noninductive  $0.5 \Omega$  resistor was used as the resistance  $R$  and the measurements were carried out at three frequencies:  $500 \text{ Hz}$ ,  $1 \text{ kHz}$  and  $5 \text{ kHz}$ . The primary coil alone, the shielding coil alone and the complete shielded coil were all measured in turn and the results are presented in Tables 5.5 to 5.7.

Important features to note here are that the AC resistances of the primary, shielding and shielded coils increase considerably as the frequency is increased from  $500 \text{ Hz}$  to  $5 \text{ kHz}$ . This frequency dependence is due to skin depth effects and the proximity effect. Firstly, as the frequency of the current flowing through each conducting path is increased, the current tends to flow on the surface, resulting in a decrease of the effective cross sectional area through which the current flows. That increases the AC resistance of each coil. Secondly, additional eddy currents are induced in each conducting path by the radial component of the magnetic field generated by the current in other conducting paths on the same coil. This effect is important in our case because of the wide conducting

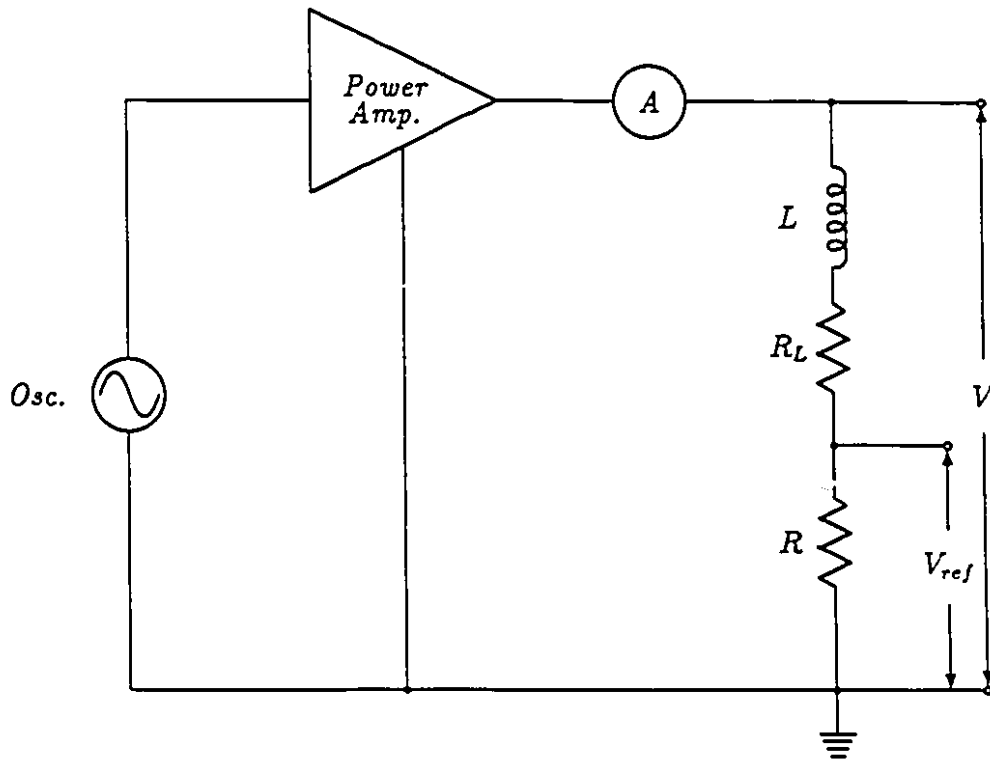


Figure 5.1: The circuit for the measurement of the coil inductance.  $L$  and  $R_L$  are the inductance and resistance of the coil, respectively.

Table 5.5: Dependence of the inductance,  $L_p$ , and AC resistance,  $R_L$ , of the primary coil on the frequency,  $\nu$ , of the current flowing through it. The estimated errors for the inductance and AC resistance are  $\pm 1 \mu H$  and  $\pm 1 m\Omega$ , respectively.

| $\nu$ (Hz) | $L_p$ ( $\mu H$ ) | $R_L$ ( $\Omega$ ) |
|------------|-------------------|--------------------|
| 500        | 314               | 0.112              |
| 1000       | 309               | 0.153              |
| 5000       | 298               | 1.090              |

Table 5.6: Dependence of the inductance,  $L_s$ , and AC resistance,  $R_L$ , of the shielding coil on the frequency,  $\nu$ , of the current flowing through it. The estimated errors for the inductance and AC resistance are  $\pm 1 \mu H$  and  $\pm 1 m\Omega$ , respectively.

| $\nu$ (Hz) | $L_s$ ( $\mu H$ ) | $R_L$ ( $\Omega$ ) |
|------------|-------------------|--------------------|
| 500        | 113               | 0.032              |
| 1000       | 114               | 0.052              |
| 5000       | 107               | 0.380              |

Table 5.7: Dependence of the inductance,  $L$ , and AC resistance,  $R_L$ , of the shielded coil on the frequency,  $\nu$ , of the current flowing through it. The estimated errors for the inductance and AC resistance are  $\pm 1 \mu H$  and  $\pm 1 m\Omega$ , respectively.  $L_p$  and  $L_s$  are the inductances of the primary and shielding coils, respectively.

| $\nu$ (Hz) | $L$ ( $\mu H$ ) | $L_p - L_s$ ( $\mu H$ ) | $R_L$ ( $\Omega$ ) |
|------------|-----------------|-------------------------|--------------------|
| 500        | 196             | 201                     | 0.149              |
| 1000       | 196             | 195                     | 0.169              |
| 5000       | 188             | 191                     | 0.738              |

paths and the close proximity of adjacent conducting paths. Thirdly, a similar eddy current will be caused by the magnetic field generated by the other coil. That this is occurring in our case can be seen by noting that the AC resistance at 5 kHz of the complete shielded coil is *smaller* than that of the primary coil alone. That occurs because the magnetic fields generated by the primary and shielding coils tend to cancel each other.

It can be seen that the inductances of the primary, shielding and shielded coils decrease slightly with increasing frequency. This is believed to be because the eddy currents induced in the coils, especially those flowing in the central elliptical region of each quadrant (see Figure 4.1), produce a magnetic field which opposes the field produced by the input current, thereby reducing the magnetic flux intercepted by each of the coils. Since the inductance of a coil is a measure of the magnetic flux threading it, the inductances of our coils decrease as the frequency is increased.

It can also be seen in Table 5.7 that  $L_p - L_s$ , the difference between the inductances of the primary coil alone and the shielding coil alone, is very close to the value of the inductance of the shielded coil at each frequency, in agreement with the theoretical result given by Eq. 3.56.

The measurements were repeated with the shielding coil disconnected from the primary coil, and shorted out to mimic passive shielding (Turner and Bowley 1986). The inductance and the AC resistance of the passively shielded coil are shown in Table 5.8.

By comparing the results in Table 5.7 with those in Table 5.8, it can be seen that the inductance is almost the same at each frequency for active and passive shielding. The AC resistance, on the other hand, seems to be slightly smaller in the case of passive shielding than for active shielding, presumably because the skin depth is not much smaller than the thickness of the copper

Table 5.8: Dependence of the inductance,  $L$ , and AC resistance,  $R_L$ , of the shielded coil on the frequency  $\nu$  when the shielding coil is disconnected and shorted so as to mimic passive shielding. The estimated errors for the inductance and AC resistance are  $\pm 1 \mu H$  and  $\pm 1 m\Omega$ , respectively.

| $\nu$ (Hz) | $L$ ( $\mu H$ ) | $R_L$ ( $\Omega$ ) |
|------------|-----------------|--------------------|
| 500        | 197             | 0.139              |
| 1000       | 196             | 0.168              |
| 5000       | 188             | 0.716              |

conductors. Thus, the current induced in the shielding coil in the case of passive shielding is less than it is in the case of active shielding.

#### 5.4 Measurement of the magnetic field generated by the shielded transverse gradient coil

The spatial dependences of the magnetic fields generated by the primary coil and the shielded coil were measured at interior and exterior points. This was done by feeding a sinusoidal current through the coil and measuring the voltage induced in a small cylindrical search coil, placed at various points.

#### 5.4.1 Determination of the magnetic field strength from the voltage induced in the search coil

The voltage induced in a coil by a time dependent magnetic field  $B(t)$  is given by

$$V(t) = -\frac{d\Phi(t)}{dt} \quad (5.3)$$

where  $\Phi$  is the magnetic flux linkage. If  $B(t)$  within the coil is uniform, Eq. 5.3 becomes

$$V(t) = -AN\frac{dB(t)}{dt} \quad (5.4)$$

where the product  $AN$  is the area-turns of the coil. If the voltage induced in the coil is sinusoidal with a frequency  $\nu$ , the magnetic field which induces it must have the same wave form. Then the amplitudes of the voltage and field, denoted respectively as  $V$  and  $B$ , are related by

$$V = 2\pi\nu ANB \quad (5.5)$$

which can be also written as

$$B = \frac{V}{2\pi\nu AN}. \quad (5.6)$$

#### 5.4.2 Description of the search coil and measurement of its area-turns

A cylindrical search coil, approximately 10 *mm* in length and diameter, was wound with 100 turns of #32 gauge copper wire.

The area-turns of the search coil was measured using a fluxmeter manufactured by the Cambridge Instrument Company. The search coil was placed in a uniform magnetic field of 0.672 *T* provided by an NMR magnet, the axis of the coil being parallel to the field. The change in the reading of the fluxmeter, when

the search coil was removed from the magnetic field, was found to be  $6.10 \times 10^{-3}$  weber-turns. It follows that the area-turns of the search coil is  $9.08 \times 10^{-3} \text{ m}^2$ . The calibration of the fluxmeter was checked using another search coil of known area-turns. (Its geometry, however, was unsuitable for measuring the magnetic field generated by our gradient coil.)

#### 5.4.3 The magnetic field profile inside the unshielded primary coil

The longitudinal component of the magnetic field,  $B_z$ , inside the unshielded primary coil was measured at  $y = 0, \pm 5 \text{ cm}$  and various values of  $x$  and  $z$ , by feeding a 1 A, 1 kHz current through the coil. The voltage induced in the search coil was measured using a Hewlett-Packard 3410A AC microvoltmeter. The calibration of the microvoltmeter was later checked using an EG&G lock-in analyzer. It was also found using the analyzer that the voltage induced in the search coil was in phase (or antiphase) with the voltage across the primary coil.

The measured values of  $B_z$  are plotted in Figures 5.2 to 5.4, as a function of  $z$  at  $x = \pm 5 \text{ cm}$  and at  $y = 5 \text{ cm}, 0$  and  $-5 \text{ cm}$ , respectively.

It can be seen that  $B_z$  falls off quite rapidly with increasing  $|z|$ . Moreover, the behavior is fairly symmetric about  $z = 0$  at  $x = \pm 5 \text{ cm}, y = 0$ , but is quite asymmetric about  $z = 0$  at  $x = \pm 5 \text{ cm}, y = 5 \text{ cm}$  and  $x = \pm 5 \text{ cm}, y = -5 \text{ cm}$ . The lack of symmetry is believed to be due to the axis of the search coil not being exactly parallel to the  $z$ -axis in these measurements. The coil therefore picked up a transverse component as well as the longitudinal component of the magnetic field.

In order to check the uniformity of the field gradient, the method of linear regression was used to fit the data of  $B_z$  as a function of  $x$  at  $y = 0, \pm 5 \text{ cm}$  and at  $z = -6.3 \text{ cm}, -0.3 \text{ cm}$  and  $5.7 \text{ cm}$ . The slopes and intercepts of the resulting



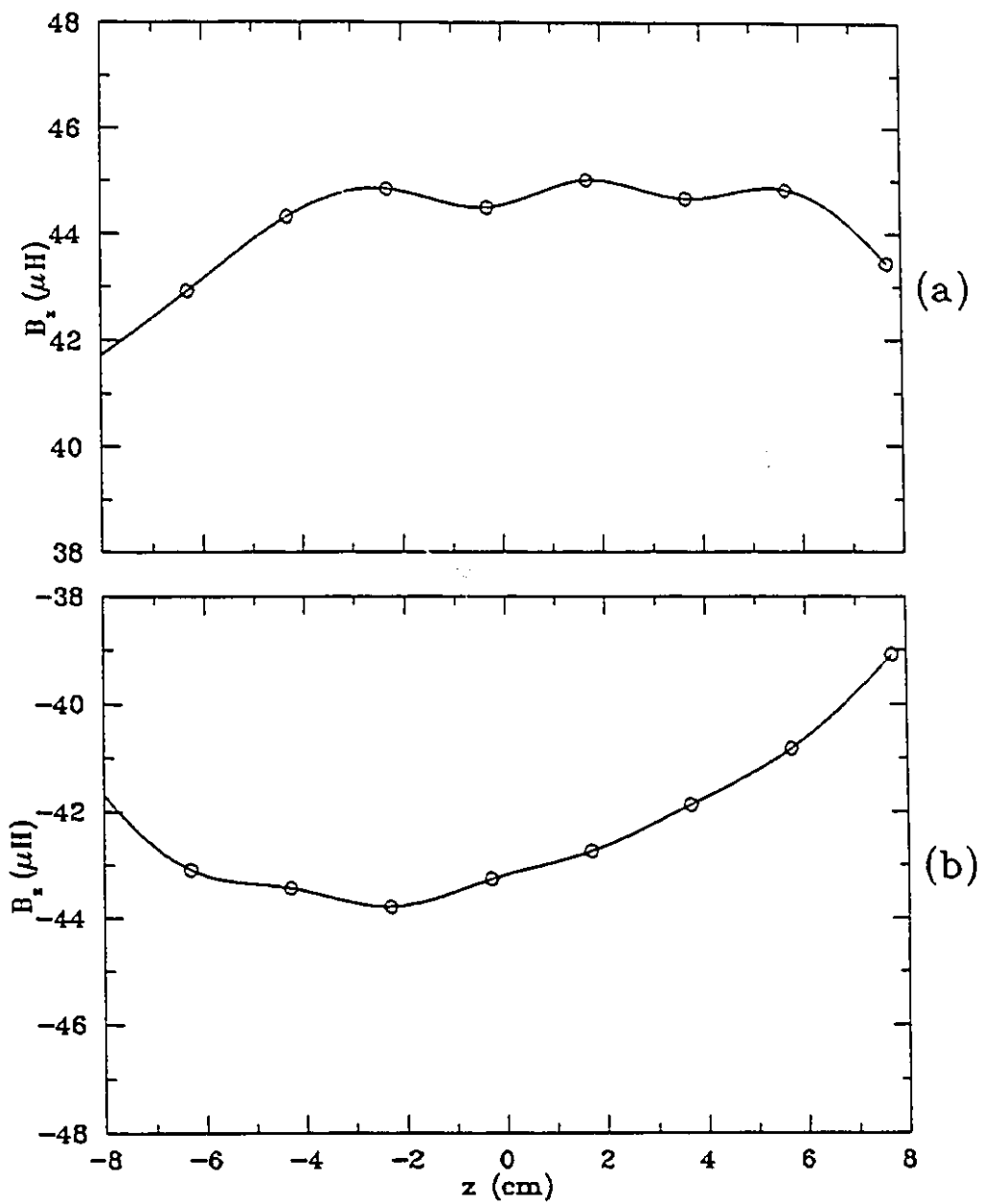


Figure 5.2: The longitudinal component of the magnetic field,  $B_z$ , generated by a 1 A, 1 kHz current passing through the unshielded primary coil, plotted as a function of  $z$  at (a)  $x = 5 \text{ cm}$  and  $y = 5 \text{ cm}$ , and (b)  $x = -5 \text{ cm}$  and  $y = 5 \text{ cm}$ .

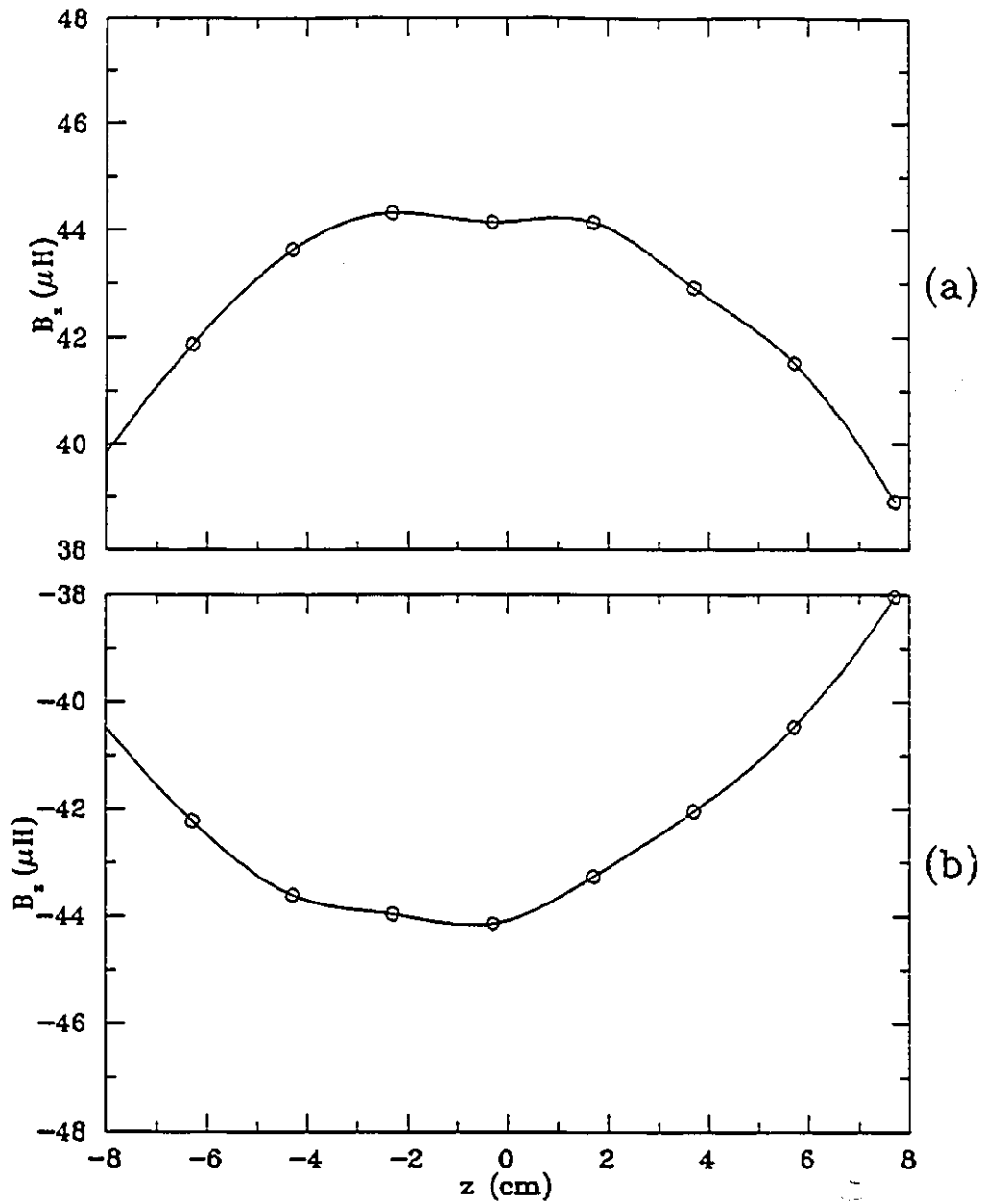


Figure 5.3: The longitudinal component of the magnetic field,  $B_z$ , generated by a 1 A, 1 kHz current passing through the unshielded primary coil, plotted as a function of  $z$  at (a)  $x = 5 \text{ cm}$  and  $y = 0$ , and (b)  $x = -5 \text{ cm}$  and  $y = 0$ .

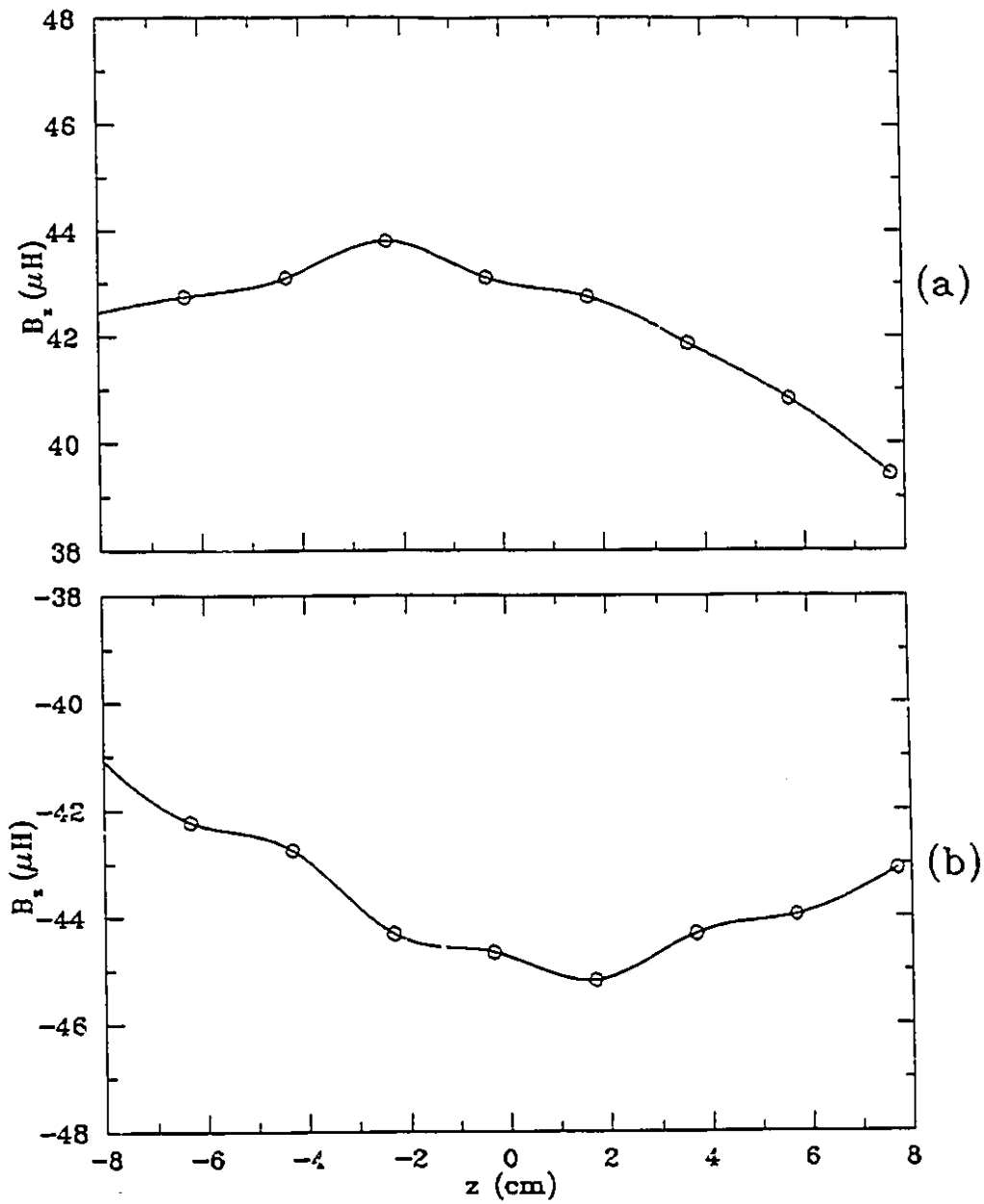


Figure 5.4: The longitudinal component of the magnetic field,  $B_z$ , generated by a 1 A, 1 kHz current passing through the unshielded primary coil, plotted as a function of  $z$  at (a)  $x = 5$  cm and  $y = -5$  cm, and (b)  $x = -5$  cm and  $y = -5$  cm.

best fits are listed in Tables 5.9 and 5.10, respectively. Figure 5.5 shows a plot of  $B_z$  as a function of  $x$  at  $y = 0$  and  $z = -0.3$  cm. The straight line in the figure represents the best fit to the data obtained by linear regression.

It can be seen that  $B_z$  is proportional to  $x$  in the region  $|x| \leq 5$  cm. The slopes of the straight lines at  $z = -6.3$  cm and at  $z = 5.7$  cm are smaller than those at  $z = -0.3$  cm, indicating that  $B_z$  falls off on both sides of  $z = 0$ , which is consistent with the data shown in Figures 5.2 to 5.4. Along the  $y$  direction, the slopes of the straight lines are similar at  $z = -6.3$  cm and at  $z = -0.3$  cm, but are not so similar at  $z = 5.7$  cm. Since the magnetic field  $B_z$  was generated by a 1 A current, the average value of the slopes is the coil efficiency of the primary coil alone, which is  $8.5 \times 10^{-4}$  T/m · A.

#### 5.4.4 The magnetic field profile inside the shielded coil

The longitudinal component of the magnetic field  $B_z$  inside the shielded coil was measured at  $y = 0, \pm 5$  cm and at various values of  $x$  and  $z$  by feeding a 1 A AC current through coil. For these measurements, a more rigid support was used to maintain the axis of the search coil parallel to the  $z$ -axis, to avoid the problem encountered in measuring the magnetic field profile inside the primary coil. In this case, measurements were made at two frequencies, namely 1 kHz and 5 kHz. The 1 kHz data are shown in Figures 5.6 to 5.8 as a function of  $z$  at  $x = \pm 5$  cm and  $y = 0, \pm 5$  cm. The 5 kHz data are shown in Figures 5.9 to 5.11.

It can be seen that  $B_z$  is much more uniform along the  $z$  direction for the shielded coil than for the primary coil alone, in the range  $|z| \leq 5$  cm. This is as expected since the shielded coil was designed to produce a uniform gradient whereas the primary coil and the shielding coil separately were not (Turner 1990). It can also be seen that the magnetic field generated by the 1 A, 1 kHz

Table 5.9: The slopes of the best fits to the data of  $B_z$  as a function of  $x$  at  $y = 0, \pm 5 \text{ cm}$  and at  $z = -6.3 \text{ cm}, -0.3 \text{ cm}$  and  $5.7 \text{ cm}$  for a  $1 \text{ A}, 1 \text{ kHz}$  current passing through the unshielded primary coil.

|                       | Slope ( $\times 10^{-4} \text{ T/m}$ ) |                 |                    |
|-----------------------|--|-----------------|--------------------|
|                       | $y = -5 \text{ cm}$                    | $y = 0$         | $y = 5 \text{ cm}$ |
| $z = -6.3 \text{ cm}$ | $8.43 \pm 0.07$                        | $8.36 \pm 0.06$ | $8.53 \pm 0.09$    |
| $z = -0.3 \text{ cm}$ | $8.79 \pm 0.06$                        | $8.80 \pm 0.03$ | $8.77 \pm 0.05$    |
| $z = 5.7 \text{ cm}$  | $8.41 \pm 0.09$                        | $8.13 \pm 0.07$ | $8.5 \pm 0.1$      |

Table 5.10: The intercepts of the best fits to the data of  $B_z$  as a function of  $x$  at  $y = 0, \pm 5 \text{ cm}$  and at  $z = -6.3 \text{ cm}, -0.3 \text{ cm}$  and  $5.7 \text{ cm}$  for a  $1 \text{ A}, 1 \text{ kHz}$  current passing through the unshielded primary coil.

|                       | Intercept ( $\mu\text{T}$ ) |                |                    |
|-----------------------|-----------------------------|----------------|--------------------|
|                       | $y = -5 \text{ cm}$         | $y = 0$        | $y = 5 \text{ cm}$ |
| $z = -6.3 \text{ cm}$ | $0.2 \pm 0.2$               | $-0.1 \pm 0.2$ | $-0.4 \pm 0.3$     |
| $z = -0.3 \text{ cm}$ | $-0.3 \pm 0.2$              | $0.2 \pm 0.1$  | $0.2 \pm 0.2$      |
| $z = 5.7 \text{ cm}$  | $-0.9 \pm 0.3$              | $0.3 \pm 0.2$  | $1.1 \pm 0.4$      |

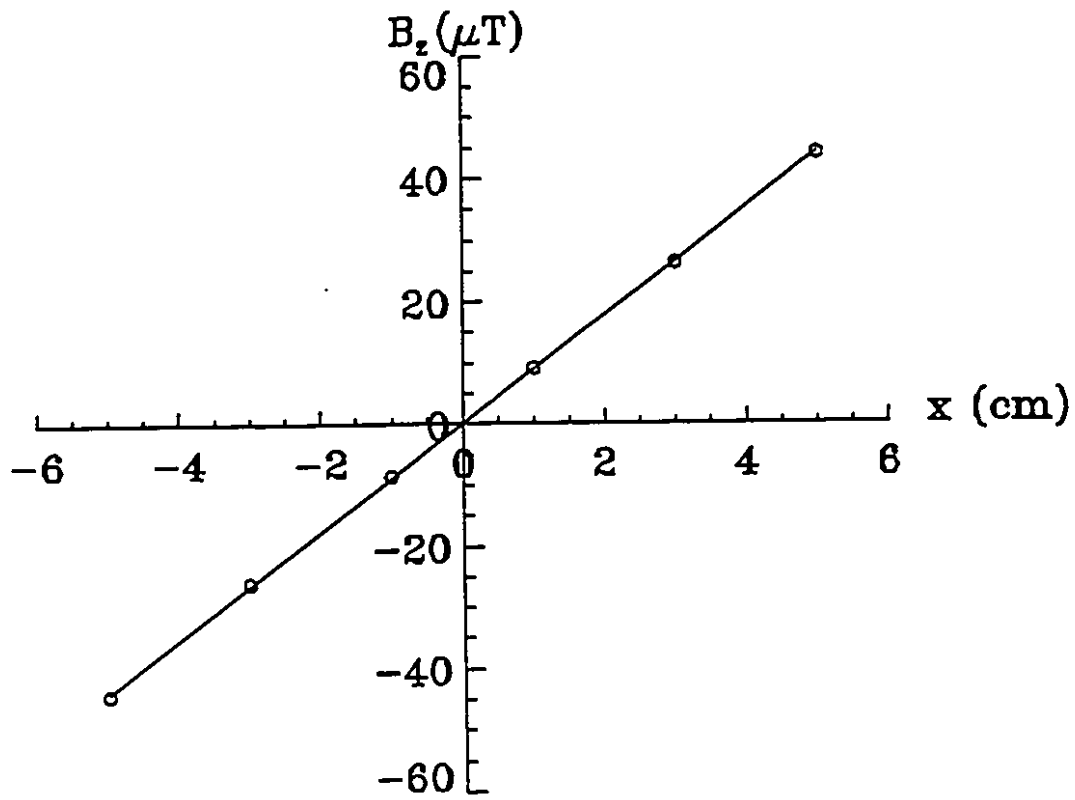


Figure 5.5: The longitudinal component of the magnetic field,  $B_z$ , generated by a 1 A, 1 kHz current passing through the unshielded primary coil, plotted as a function of  $x$  at  $y = 0$  and  $z = -0.3$  cm.

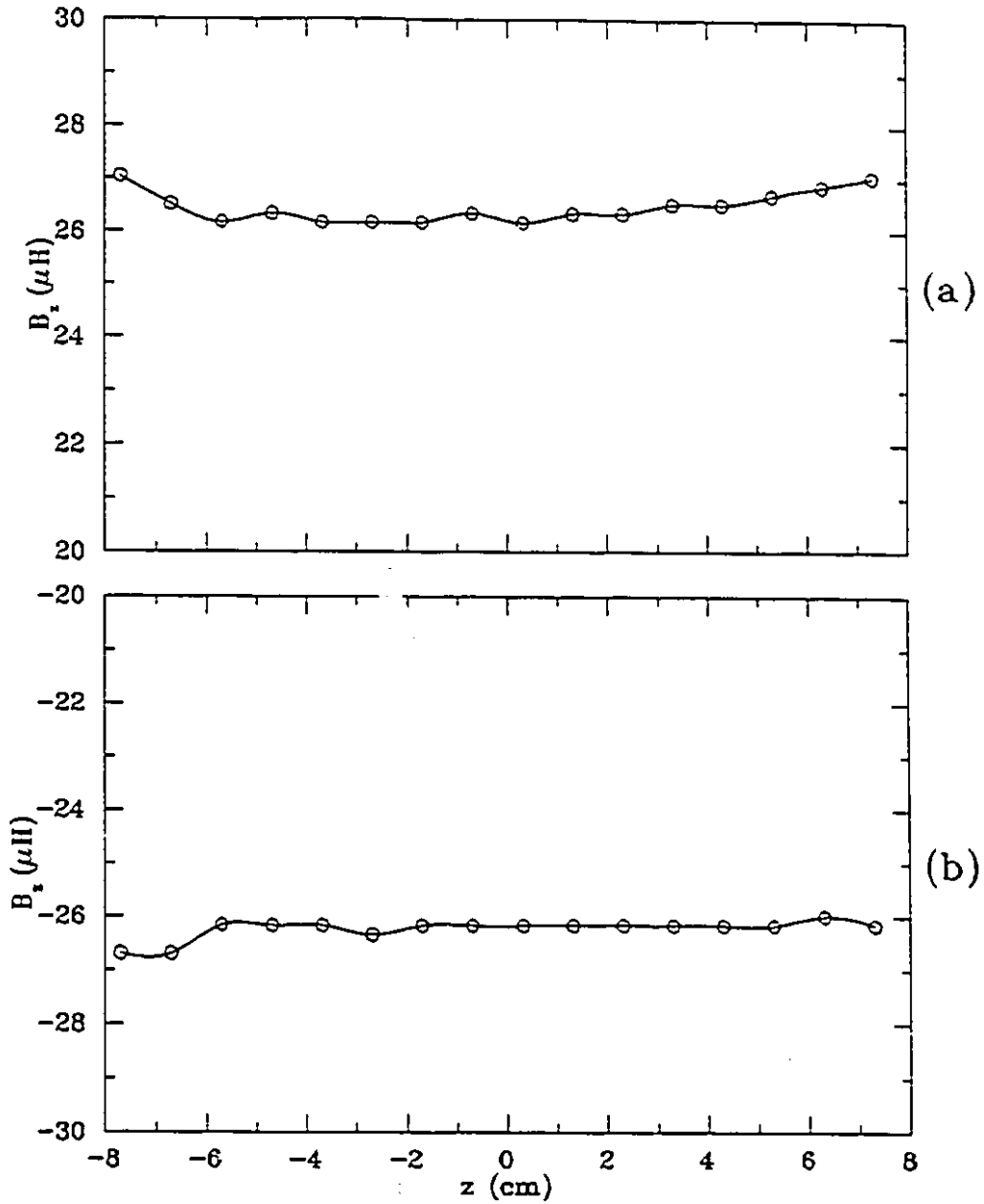


Figure 5.6: The longitudinal component of the magnetic field,  $B_z$ , generated by a 1 A, 1 kHz current passing through the shielded coil, plotted as a function of  $z$  at (a)  $x = 5 \text{ cm}$  and  $y = 5 \text{ cm}$ , and (b)  $x = -5 \text{ cm}$  and  $y = 5 \text{ cm}$ .

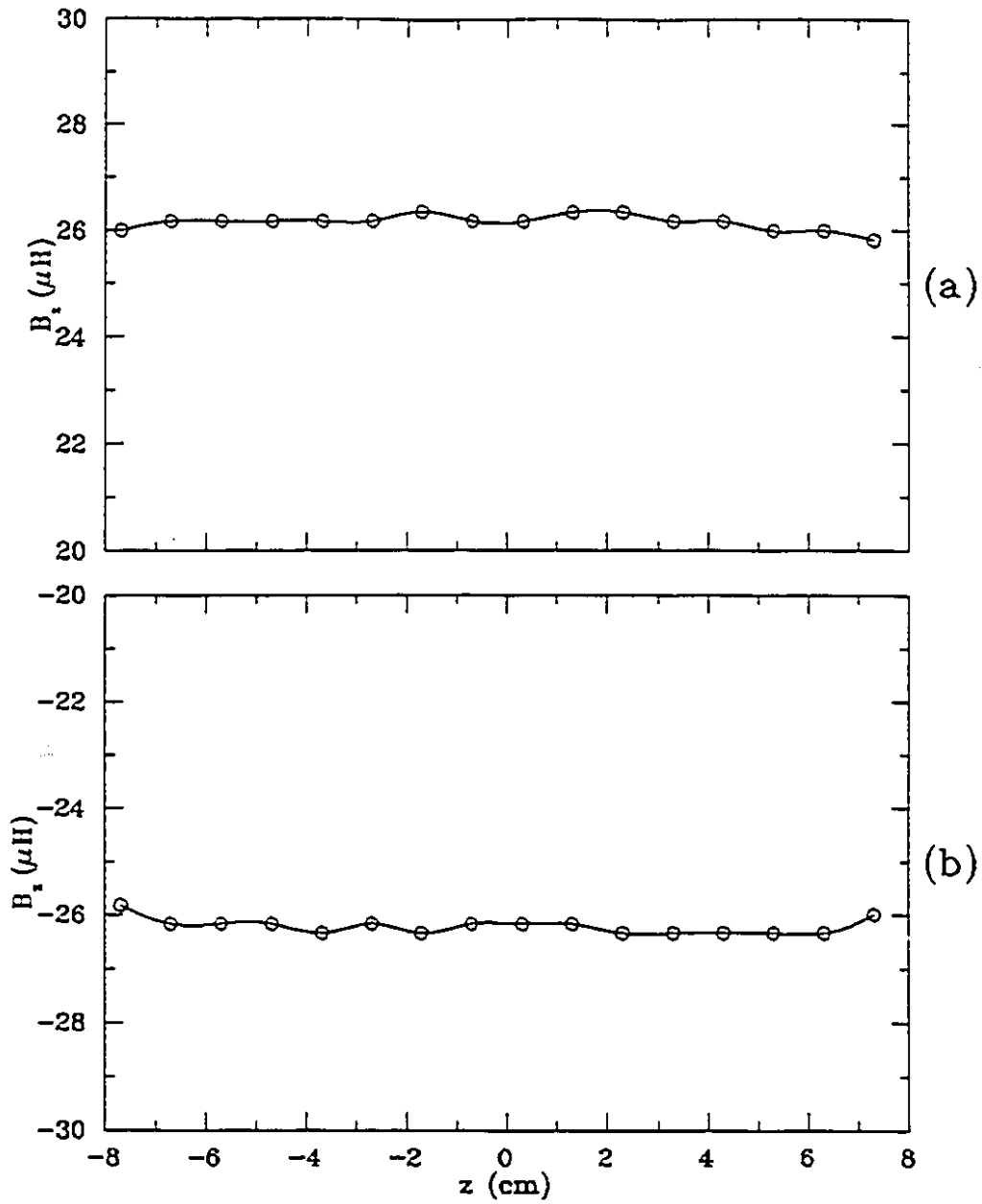


Figure 5.7: The longitudinal component of the magnetic field,  $B_z$ , generated by a 1 A, 1 kHz current passing through the shielded coil, plotted as a function of  $z$  at (a)  $x = 5 \text{ cm}$  and  $y = 0$ , and (b)  $x = -5 \text{ cm}$  and  $y = 0$ .



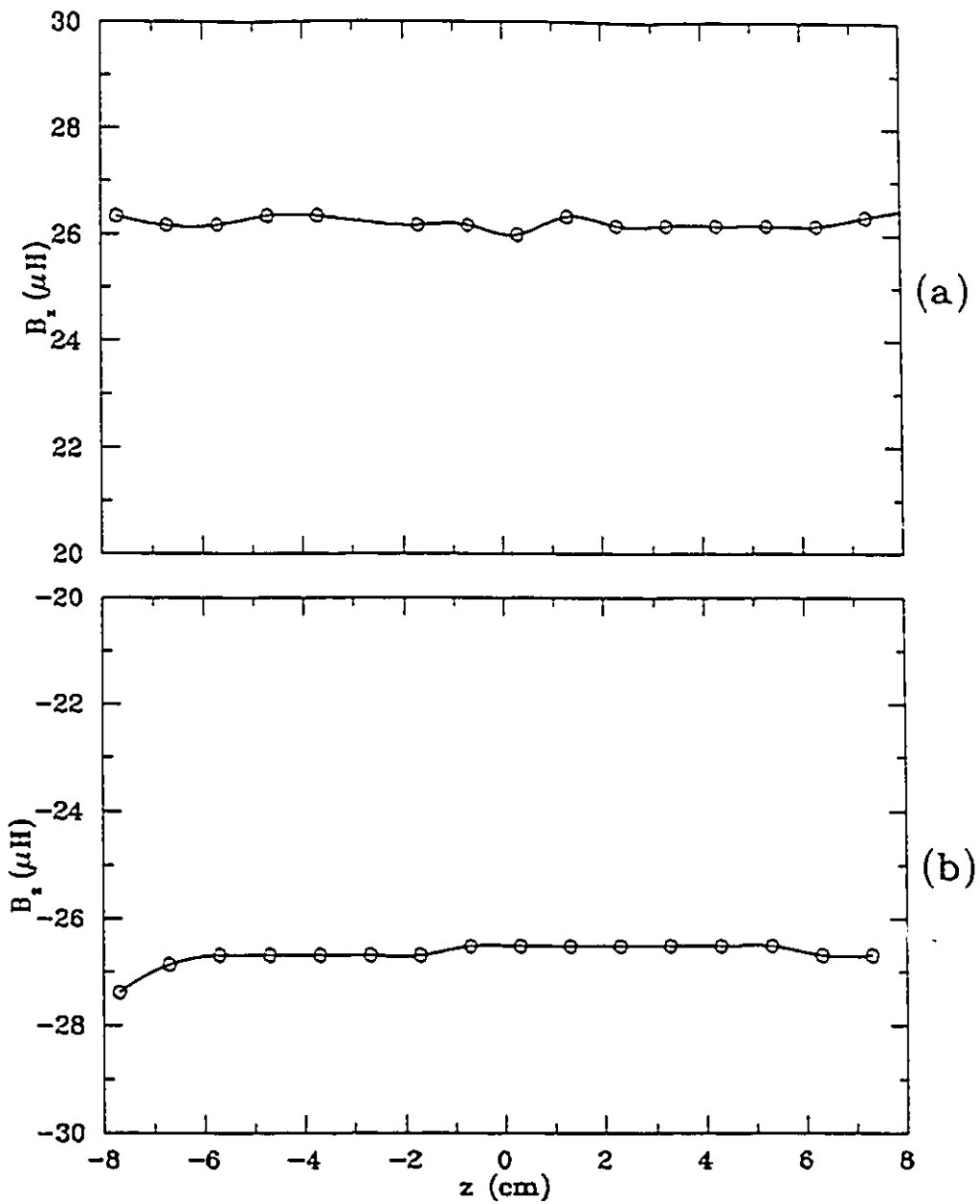


Figure 5.8: The longitudinal component of the magnetic field,  $B_z$ , generated by a 1 A, 1 kHz current passing through the shielded coil, plotted as a function of  $z$  at (a)  $x = 5 \text{ cm}$  and  $y = -5 \text{ cm}$ , and (b)  $x = -5 \text{ cm}$  and  $y = -5 \text{ cm}$ .

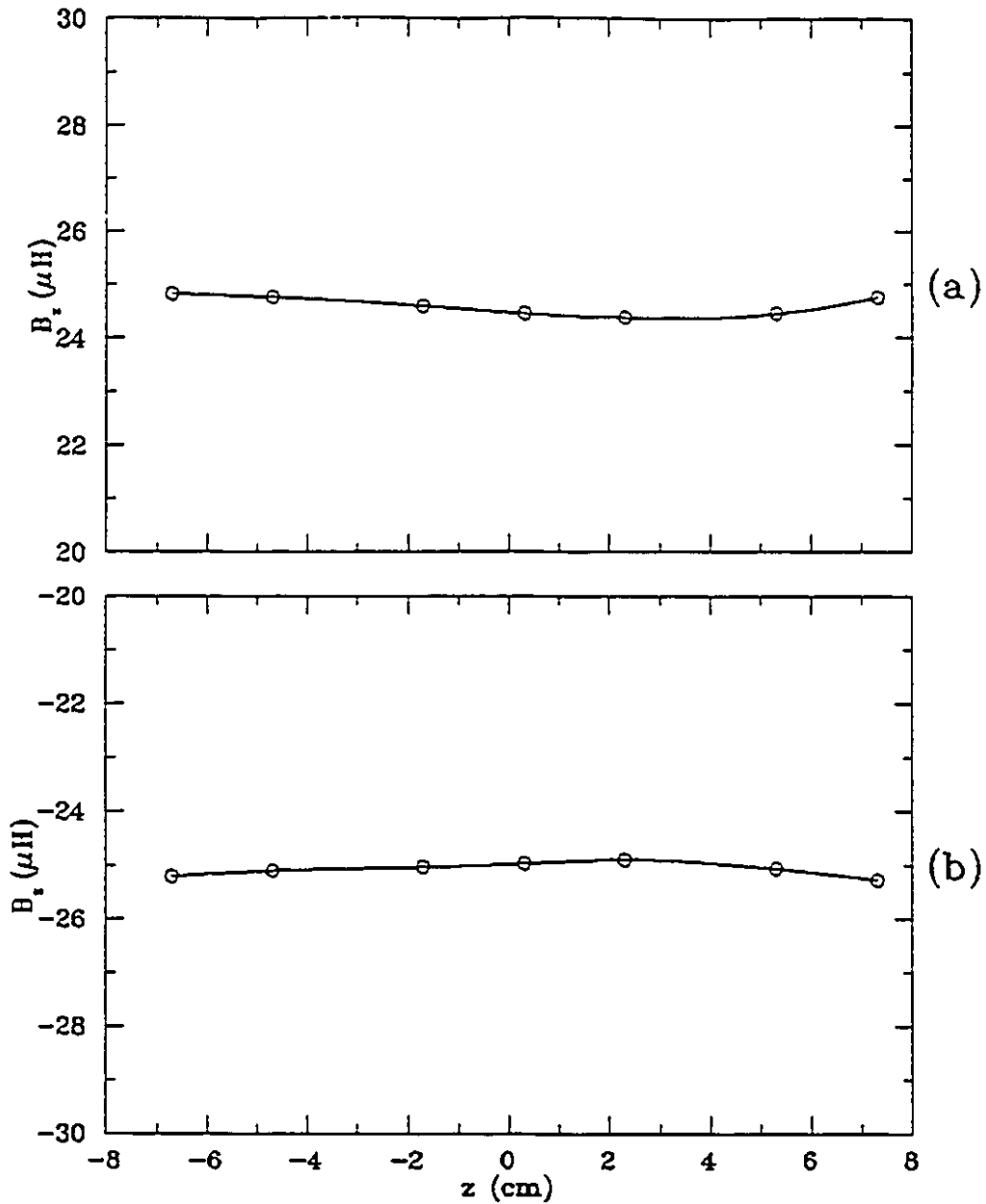


Figure 5.9: The longitudinal component of the magnetic field,  $B_z$ , generated by a 1 A, 5 kHz current passing through the shielded coil, plotted as a function of  $z$  at (a)  $x = 5 \text{ cm}$  and  $y = 5 \text{ cm}$ , and (b)  $x = -5 \text{ cm}$  and  $y = 5 \text{ cm}$ .

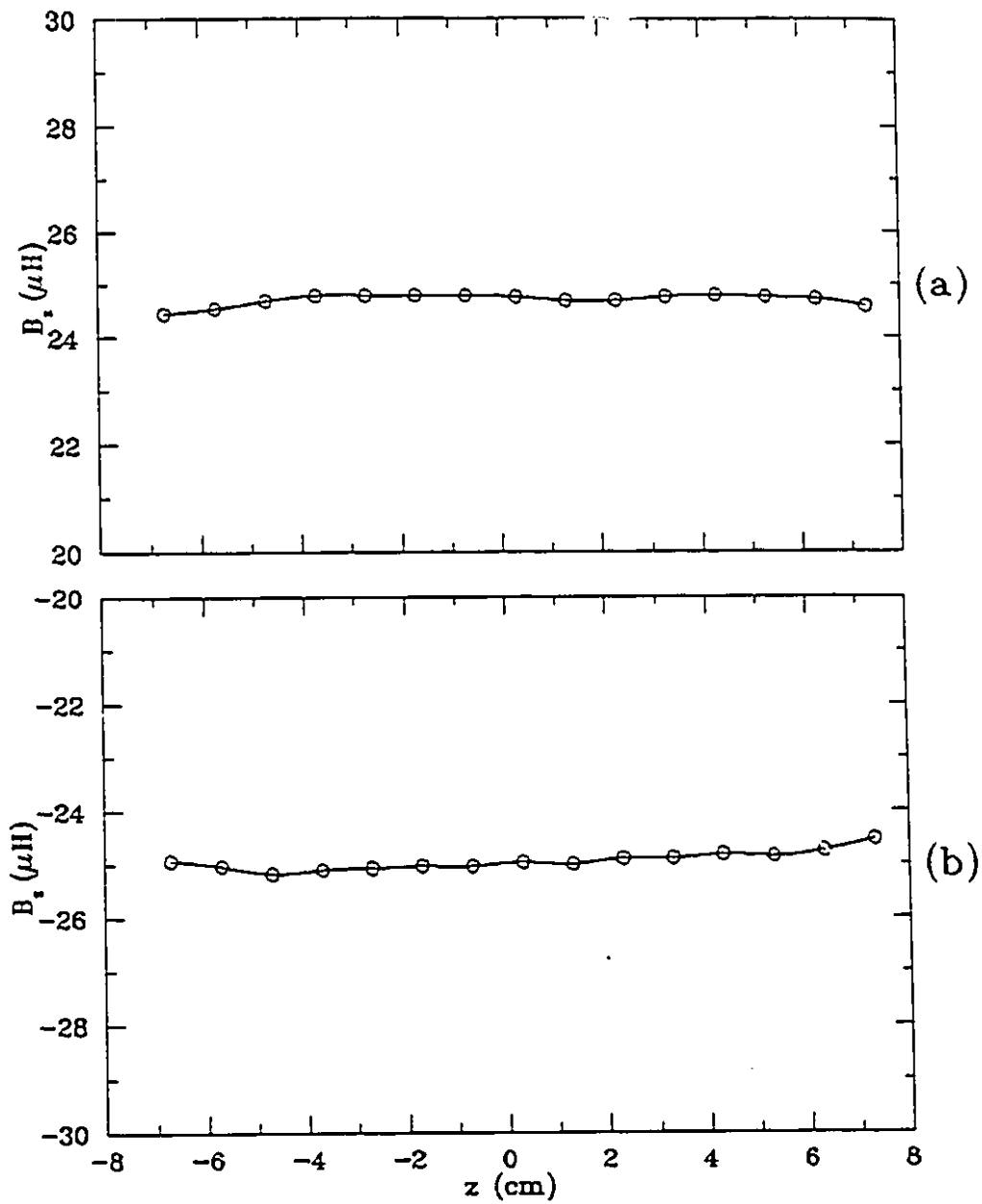


Figure 5.10: The longitudinal component of the magnetic field,  $B_z$ , generated by a 1 A, 5 kHz current passing through the shielded coil, plotted as a function of  $z$  at (a)  $x = 5 \text{ cm}$  and  $y = 0$ , and (b)  $x = -5 \text{ cm}$  and  $y = 0$ .

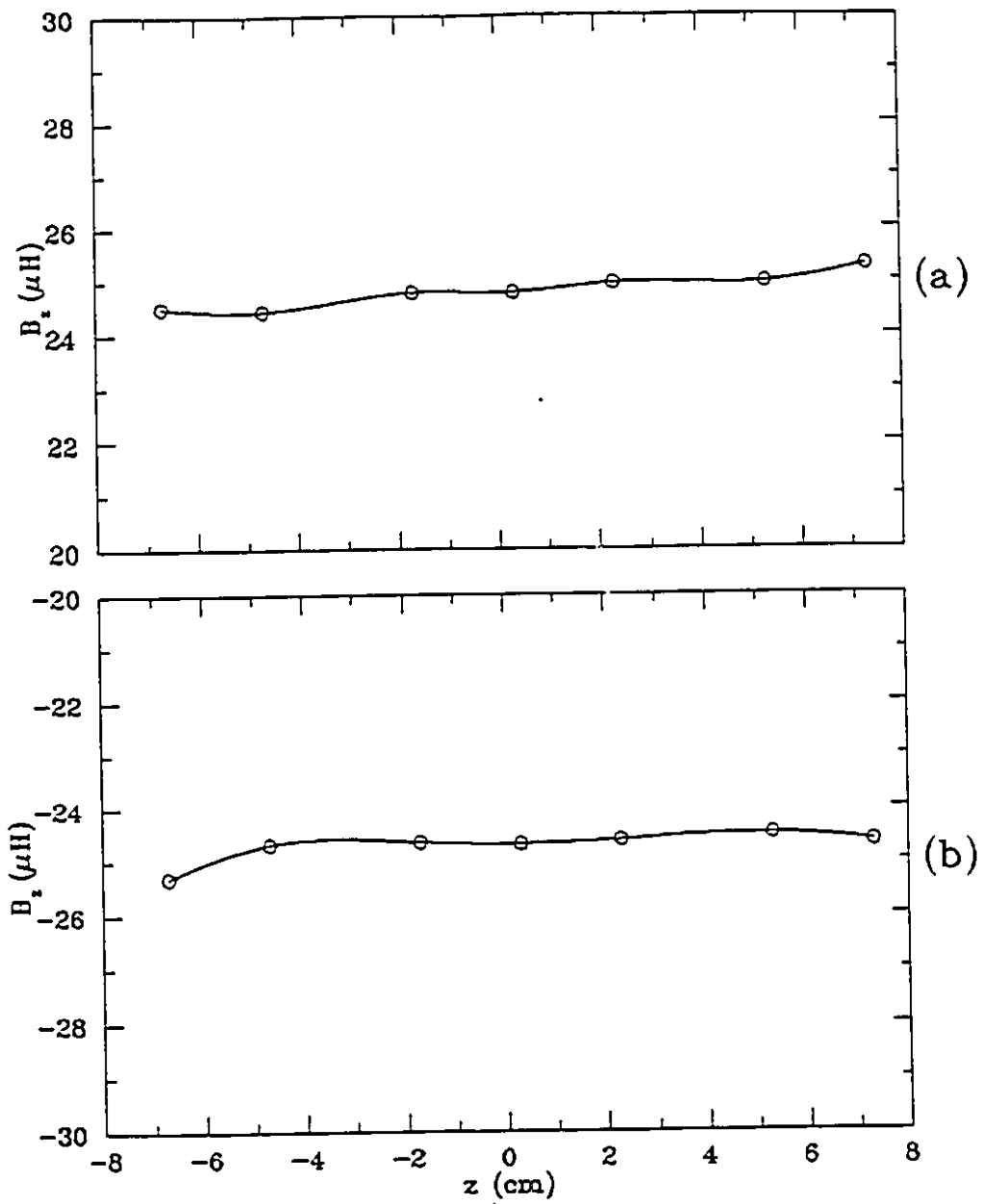


Figure 5.11: The longitudinal component of the magnetic field,  $B_z$ , generated by a 1 A, 5 kHz current passing through the shielded coil, plotted as a function of  $z$  at (a)  $x = 5$  cm and  $y = -5$  cm, and (b)  $x = -5$  cm and  $y = -5$  cm.

current is greater than that generated by the 1 A, 5 kHz current at the same positions. This is because larger eddy currents are generated in the coil at 5 kHz than at 1 kHz.

The method of linear regression was used to fit the data of  $B_z$  as a function of  $x$  at  $y = 0, \pm 5$  cm and at  $z = -4.7$  cm, 0.3 cm and 5.3 cm. The slopes and intercepts of the resulting best fits are listed in Tables 5.11 to 5.14, respectively. Figures 5.12 and 5.13 show plots of  $B_z$  as a function of  $x$  at  $y = 0$  and  $z = 0.3$  cm for the 1 kHz and 5 kHz currents, respectively. The straight lines in these figures represent the best fits to the data obtained by linear regression.

It can be seen that  $B_z$  is proportional to  $x$  in the region  $|x| \leq 5$  cm. Moreover, as can be seen in Tables 5.11 and 5.13, the slopes are essentially the same at all the locations investigated for a given frequency, showing that the gradient is indeed very uniform as desired. The coil efficiencies at 1 kHz and at 5 kHz are  $5.3 \times 10^{-4}$  T/m · A and  $5.0 \times 10^{-4}$  T/m · A, respectively, i.e. the coil efficiency decreases by 6 per cent when the frequency is increased from 1 kHz to 5 kHz, again because of eddy currents.

It can be seen that the errors in the slopes and intercepts are larger in the case for the primary coil alone than for the shielded coil because of the more uniform gradient in the latter case.

#### 5.4.5 Shielding performance of the shielded coil

The unshielded case was first investigated by removing the shielding coil and measuring  $B_x$  as a function of  $z$  at  $x = \pm 18.5$  cm and  $y = 0$  and measuring  $B_z$  as a function of  $z$  at  $x = \pm 17.3$  cm and  $y = 0$ . These measurements were made at both 1 kHz and 5 kHz. The shielded case was then investigated by reconnecting the shielding coil and repeating the measurements of  $B_x$  and  $B_z$  at

Table 5.11: The slopes of the best fits to the data of  $B_z$  as a function of  $x$  at  $y = 0, \pm 5 \text{ cm}$  and at  $z = -4.7 \text{ cm}, 0.3 \text{ cm}$  and  $5.3 \text{ cm}$  for a  $1 \text{ A}, 1 \text{ kHz}$  current passing through the shielded coil.

|                       | Slope ( $\times 10^{-4} \text{ T/m}$ ) |                   |                    |
|-----------------------|--|-------------------|--------------------|
|                       | $y = -5 \text{ cm}$                    | $y = 0$           | $y = 5 \text{ cm}$ |
| $z = -4.7 \text{ cm}$ | $5.30 \pm 0.03$                        | $5.22 \pm 0.02$   | $5.26 \pm 0.01$    |
| $z = 0.3 \text{ cm}$  | $5.25 \pm 0.01$                        | $5.235 \pm 0.005$ | $5.24 \pm 0.01$    |
| $z = 5.3 \text{ cm}$  | $5.26 \pm 0.01$                        | $5.24 \pm 0.02$   | $5.26 \pm 0.03$    |

Table 5.12: The intercepts of the best fits to the data of  $B_z$  as a function of  $x$  at  $y = 0, \pm 5 \text{ cm}$  and at  $z = -4.7 \text{ cm}, 0.3 \text{ cm}$  and  $5.3 \text{ cm}$  for a  $1 \text{ A}, 1 \text{ kHz}$  current passing through the shielded coil.

|                       | Intercept ( $\mu\text{T}$ ) |                  |                    |
|-----------------------|-----------------------------|------------------|--------------------|
|                       | $y = -5 \text{ cm}$         | $y = 0$          | $y = 5 \text{ cm}$ |
| $z = -4.7 \text{ cm}$ | $-0.3 \pm 0.1$              | $-0.04 \pm 0.07$ | $0.03 \pm 0.04$    |
| $z = 0.3 \text{ cm}$  | $-0.16 \pm 0.05$            | $-0.01 \pm 0.02$ | $0.04 \pm 0.03$    |
| $z = 5.3 \text{ cm}$  | $-0.07 \pm 0.06$            | $-0.04 \pm 0.06$ | $0.1 \pm 0.1$      |

Table 5.13: The slopes of the best fits to the data of  $B_z$  as a function of  $x$  at  $y = 0, \pm 5 \text{ cm}$  and at  $z = -4.7 \text{ cm}, 0.3 \text{ cm}$  and  $5.3 \text{ cm}$  for a  $1 \text{ A}, 5 \text{ kHz}$  current passing through the shielded coil.

|                       | Slope ( $\times 10^{-4} \text{ T/m}$ ) |                   |                    |
|-----------------------|--|-------------------|--------------------|
|                       | $y = -5 \text{ cm}$                    | $y = 0$           | $y = 5 \text{ cm}$ |
| $z = -4.7 \text{ cm}$ | $4.94 \pm 0.02$                        | $5.00 \pm 0.01$   | $4.97 \pm 0.02$    |
| $z = 0.3 \text{ cm}$  | $4.94 \pm 0.01$                        | $4.978 \pm 0.008$ | $4.93 \pm 0.01$    |
| $z = 5.3 \text{ cm}$  | $4.94 \pm 0.02$                        | $4.94 \pm 0.01$   | $4.93 \pm 0.02$    |

Table 5.14: The intercepts of the best fits to the data of  $B_z$  as a function of  $x$  at  $y = 0, \pm 5 \text{ cm}$  and at  $z = -4.7 \text{ cm}, 0.3 \text{ cm}$  and  $5.3 \text{ cm}$  for a  $1 \text{ A}, 5 \text{ kHz}$  current passing through the shielded coil.

|                       | Intercept ( $\mu\text{T}$ ) |                  |                    |
|-----------------------|-----------------------------|------------------|--------------------|
|                       | $y = -5 \text{ cm}$         | $y = 0$          | $y = 5 \text{ cm}$ |
| $z = -4.7 \text{ cm}$ | $-0.11 \pm 0.07$            | $-0.18 \pm 0.05$ | $-0.14 \pm 0.06$   |
| $z = 0.3 \text{ cm}$  | $0.08 \pm 0.04$             | $-0.07 \pm 0.03$ | $-0.20 \pm 0.05$   |
| $z = 5.3 \text{ cm}$  | $0.15 \pm 0.05$             | $-0.06 \pm 0.05$ | $-0.21 \pm 0.7$    |

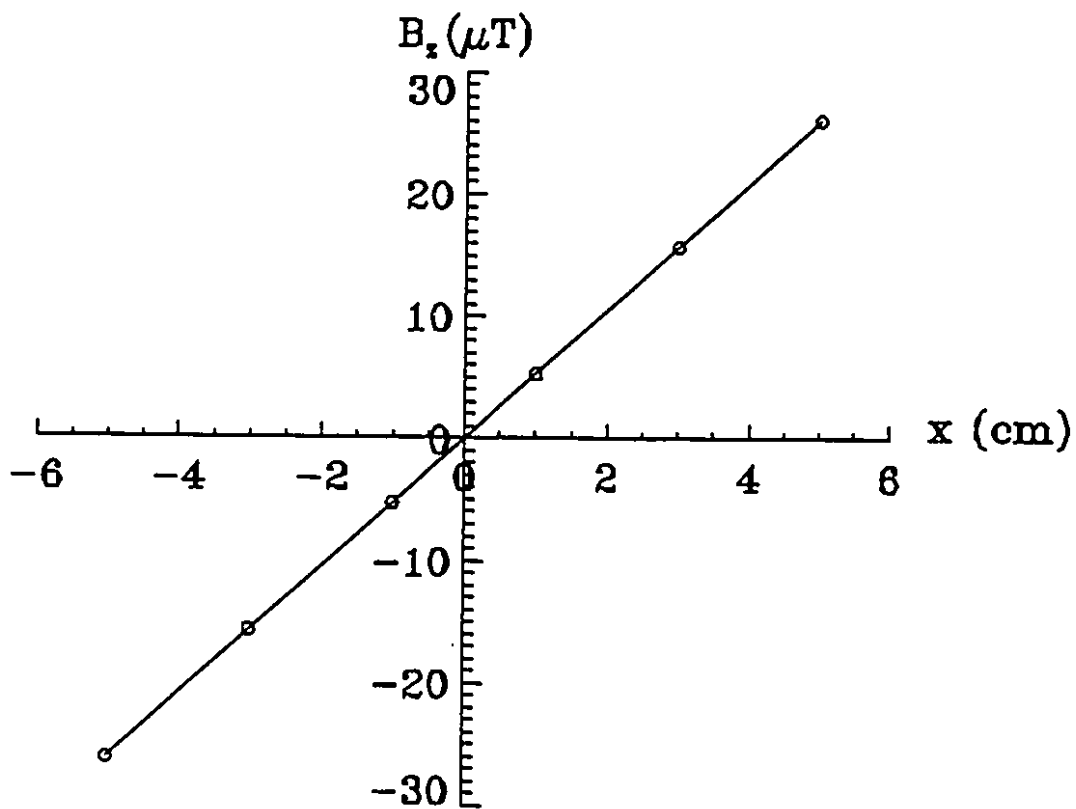


Figure 5.12: The longitudinal component of the magnetic field,  $B_z$ , generated by a 1 A, 1 kHz current passing through the shielded coil, plotted as a function of  $x$  at  $y = 0$  and  $z = 0.3$  cm.



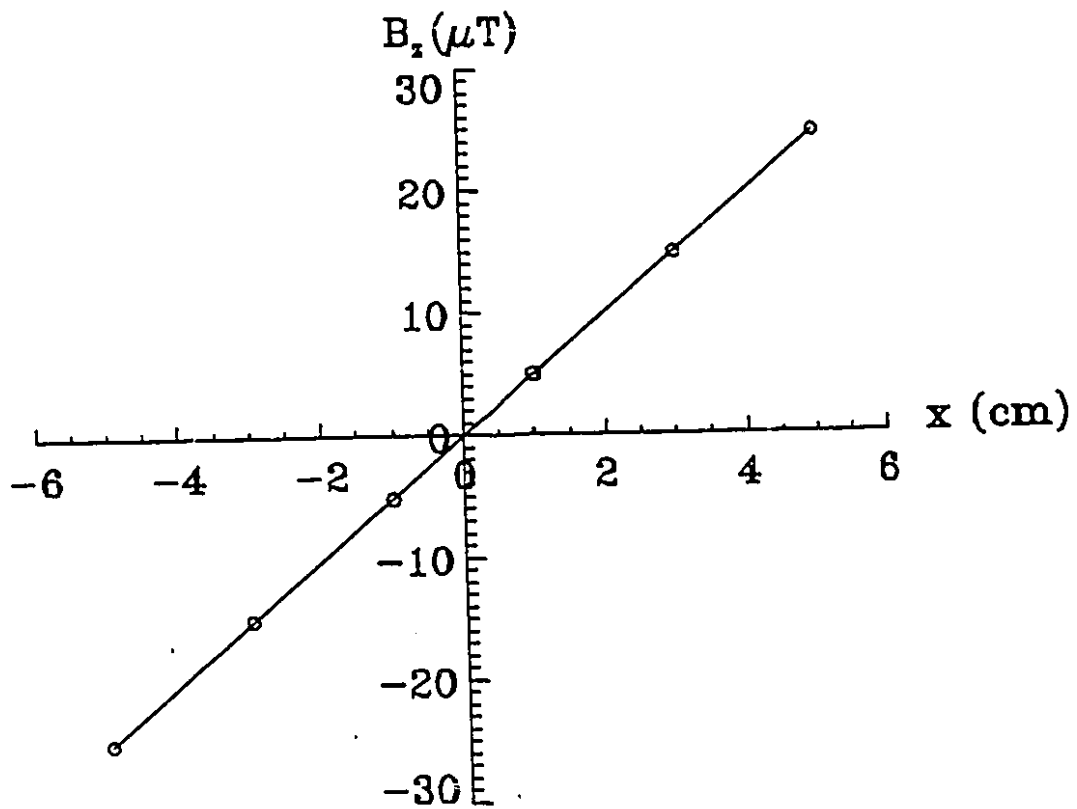


Figure 5.13: The longitudinal component of the magnetic field,  $B_z$ , generated by a 1 A, 5 kHz current passing through the shielded coil, plotted as a function of  $x$  at  $y = 0$  and  $z = 0.3 \text{ cm}$ .

the same locations as before ( which are 2.7 *cm outside* the shielding coil for  $B_x$  and 1.5 *cm outside* the shielding coil for  $B_z$ ).

To obtain additional information about the shielding performance, the shielding coil was disconnected from the primary coil and shorted out to mimic passive shielding (Turner and Bowley 1986). The above measurements were again repeated.

The various data sets are shown in Figures 5.14 to 5.21.

An important feature to note here is that the fringe field generated by the shielded coil has not only a component in phase with the magnetic field generated by the unshielded coil, but also a quadrature component, which is attributed to resistive losses associated with eddy currents. The quadrature component is largest near  $z = \pm 16$  *cm*, *i.e.* near the centers of the spiral windings, indicating that the eddy currents flow mainly in the elliptical conducting regions located at the center of each spiral (see Figure 4.1). This problem could be alleviated by removing some of the material from these elliptical regions.

The in-phase component of the fringe field consists of two parts, one being associated with the inductive part of the impedance of the elliptical sections and the other due to imperfections in the configuration of the shielding coil. The reactance of the elliptical sections is naturally larger at 5 *kHz* than at 1 *kHz*, which accounts for the smaller quadrature component measured at 5 *kHz* than at 1 *kHz*.

Comparison of graphs (a) and (b) in Figures 5.14 to 5.21 shows that the shielding is less than ideal. For example, the maximum in-phase components of the  $B_x$  field for the shielded coil is about 2% of the maximum  $B_x$  field in the absence of shielding. However, this is really equivalent to about 3% for a given gradient strength because of the reduced coil efficiency of the shielded

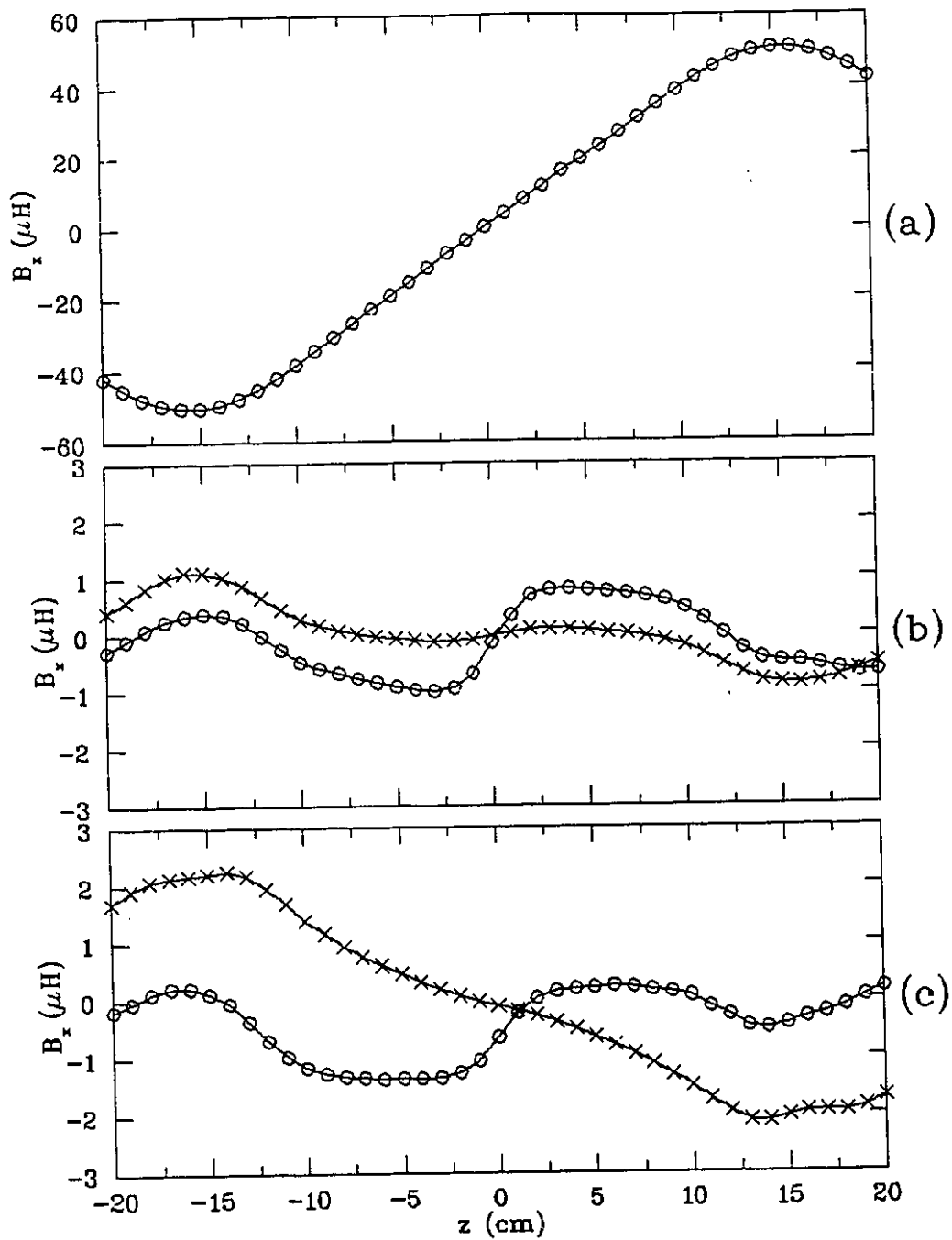


Figure 5.14: The transverse component of the fringe field,  $B_x$ , at  $x = 18.5$  cm and  $y = 0$ , generated by a 1 A, 1 kHz current, plotted as a function of  $z$  for (a) the unshielded primary coil, (b) the actively shielded coil and (c) the passively shielded coil. In (b) and (c), the in-phase and quadrature components are represented by (o) and ( $\times$ ), respectively.

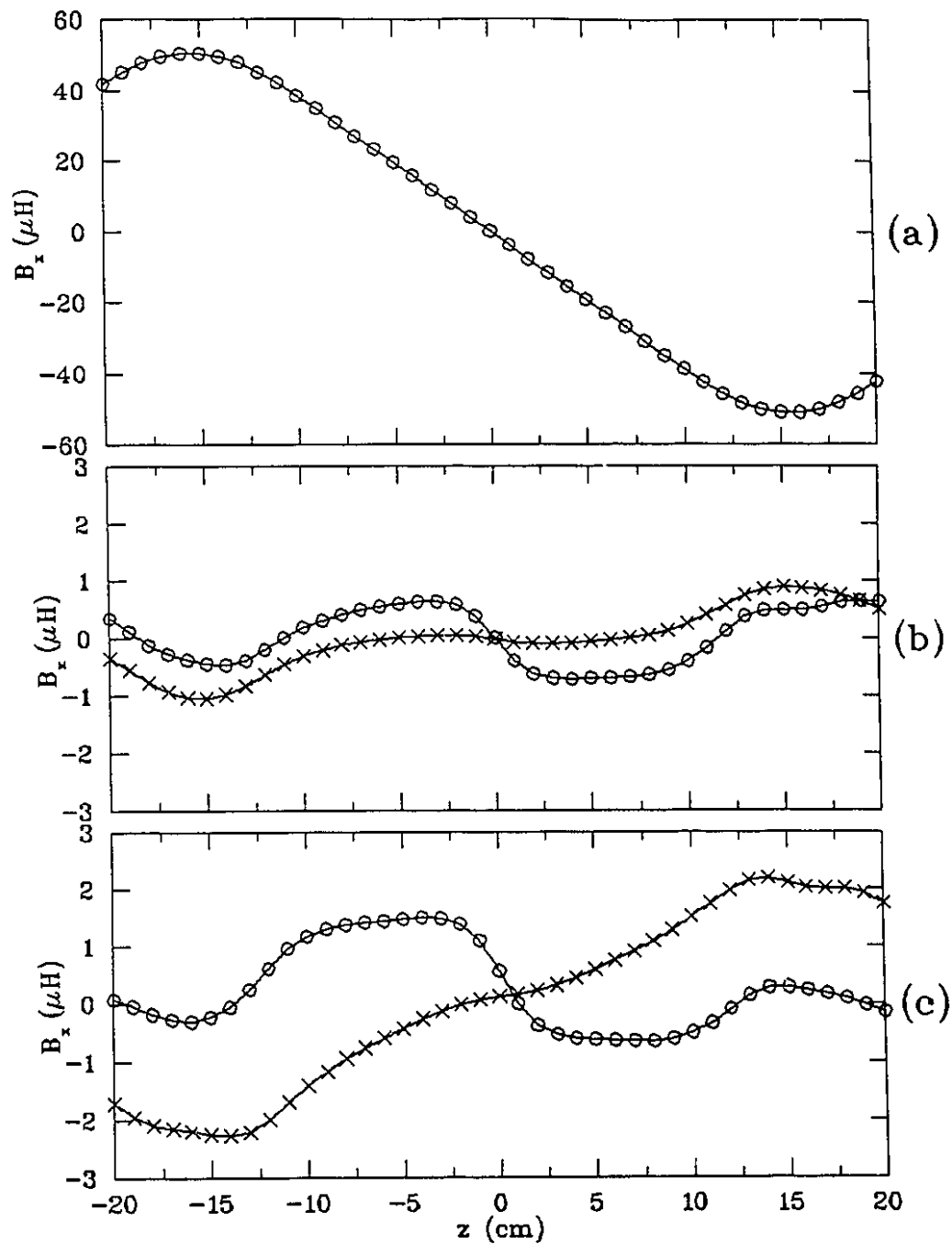


Figure 5.15: The transverse component of the fringe field,  $B_x$ , at  $x = -18.5$  cm and  $y = 0$ , generated by a 1 A, 1 kHz current, plotted as a function of  $z$  for (a) the unshielded primary coil, (b) the actively shielded coil and (c) the passively shielded coil. In (b) and (c), the in-phase and quadrature components are represented by (o) and ( $\times$ ), respectively.

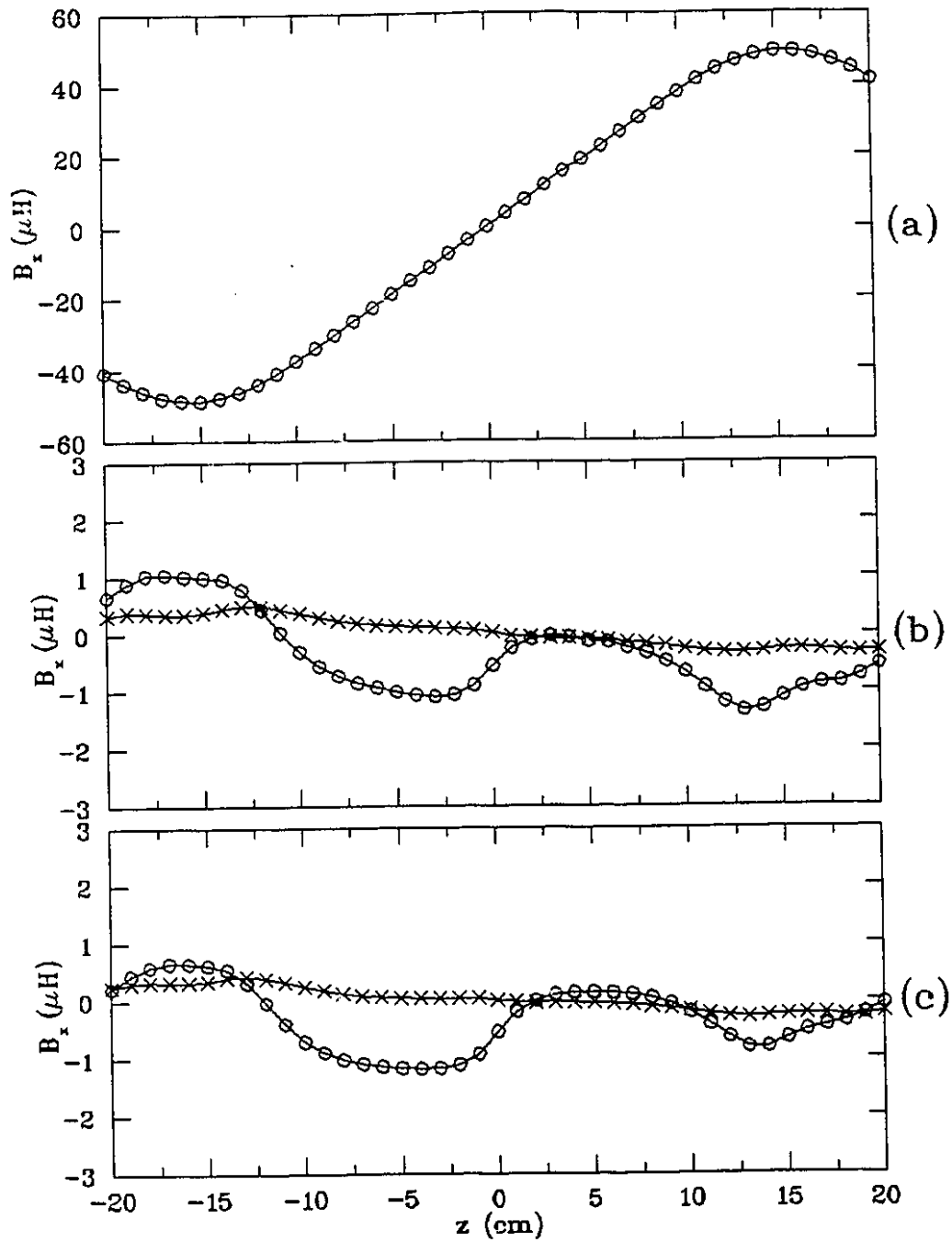


Figure 5.16: The transverse component of the fringe field,  $B_x$ , at  $x = 18.5$  cm and  $y = 0$ , generated by a 1 A, 5 kHz current, plotted as a function of  $z$  for (a) the unshielded primary coil, (b) the actively shielded coil and (c) the passively shielded coil. In (b) and (c), the in-phase and quadrature components are represented by (o) and ( $\times$ ), respectively.

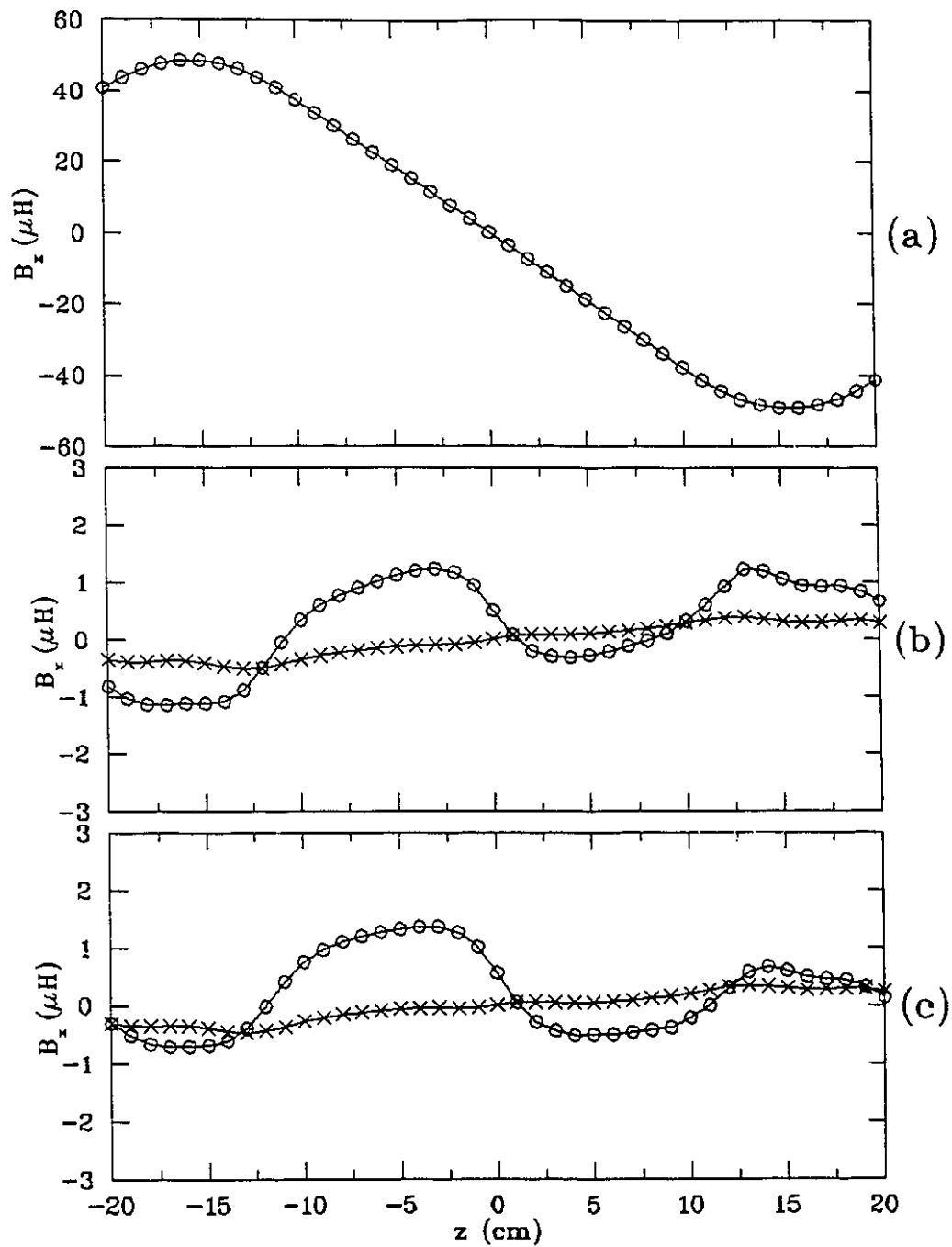


Figure 5.17: The transverse component of the fringe field,  $B_z$ , at  $x = -18.5$  cm and  $y = 0$ , generated by a 1 A, 5 kHz current, plotted as a function of  $z$  for (a) the unshielded primary coil, (b) the actively shielded coil and (c) the passively shielded coil. In (b) and (c), the in-phase and quadrature components are represented by (o) and ( $\times$ ), respectively.

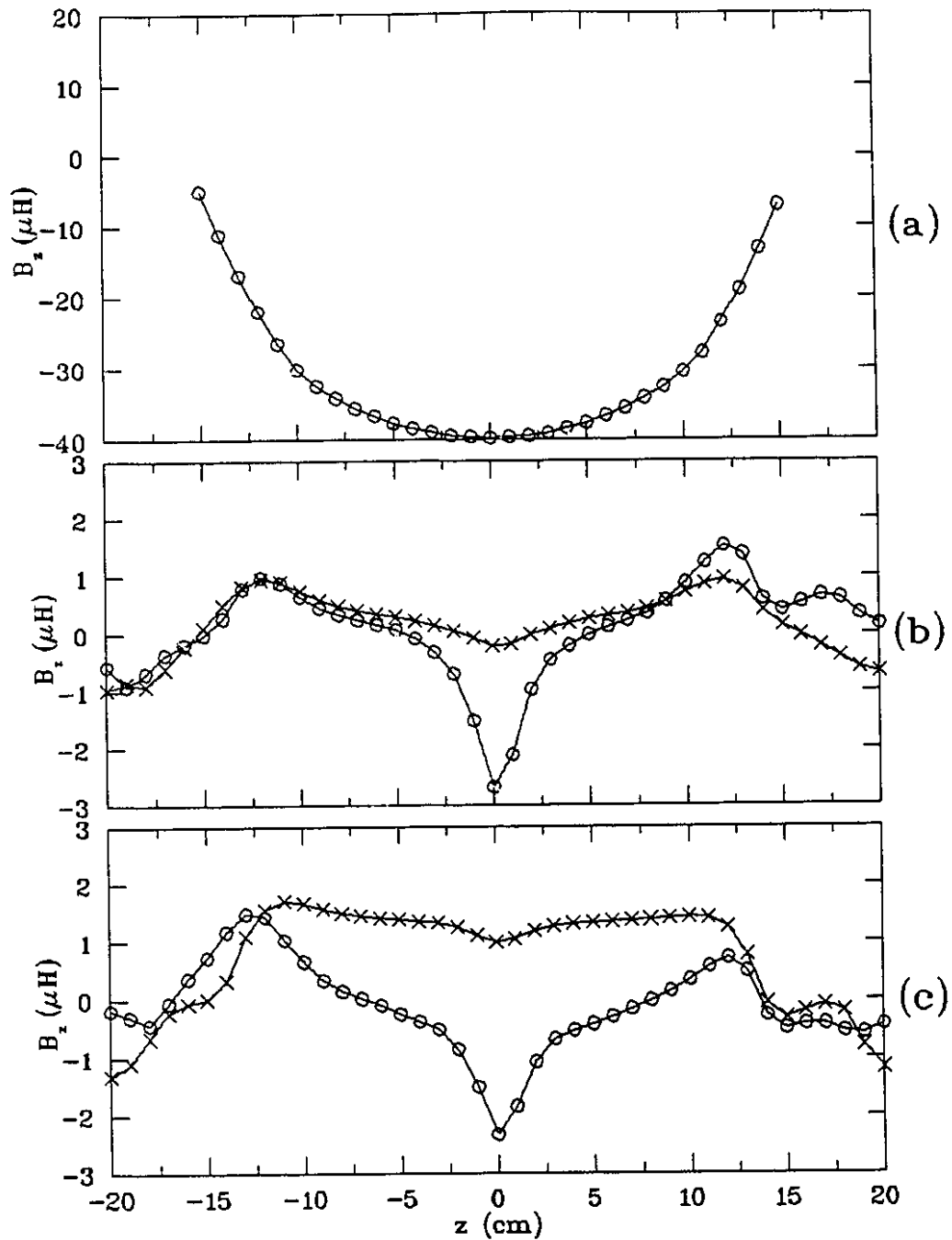


Figure 5.18: The longitudinal component of the fringe field,  $B_z$ , at  $x = 17.3$  cm and  $y = 0$ , generated by a 1 A, 1 kHz current, plotted as a function of  $z$  for (a) the unshielded primary coil, (b) the actively shielded coil and (c) the passively shielded coil. In (b) and (c), the in-phase and quadrature components are represented by (o) and ( $\times$ ), respectively.

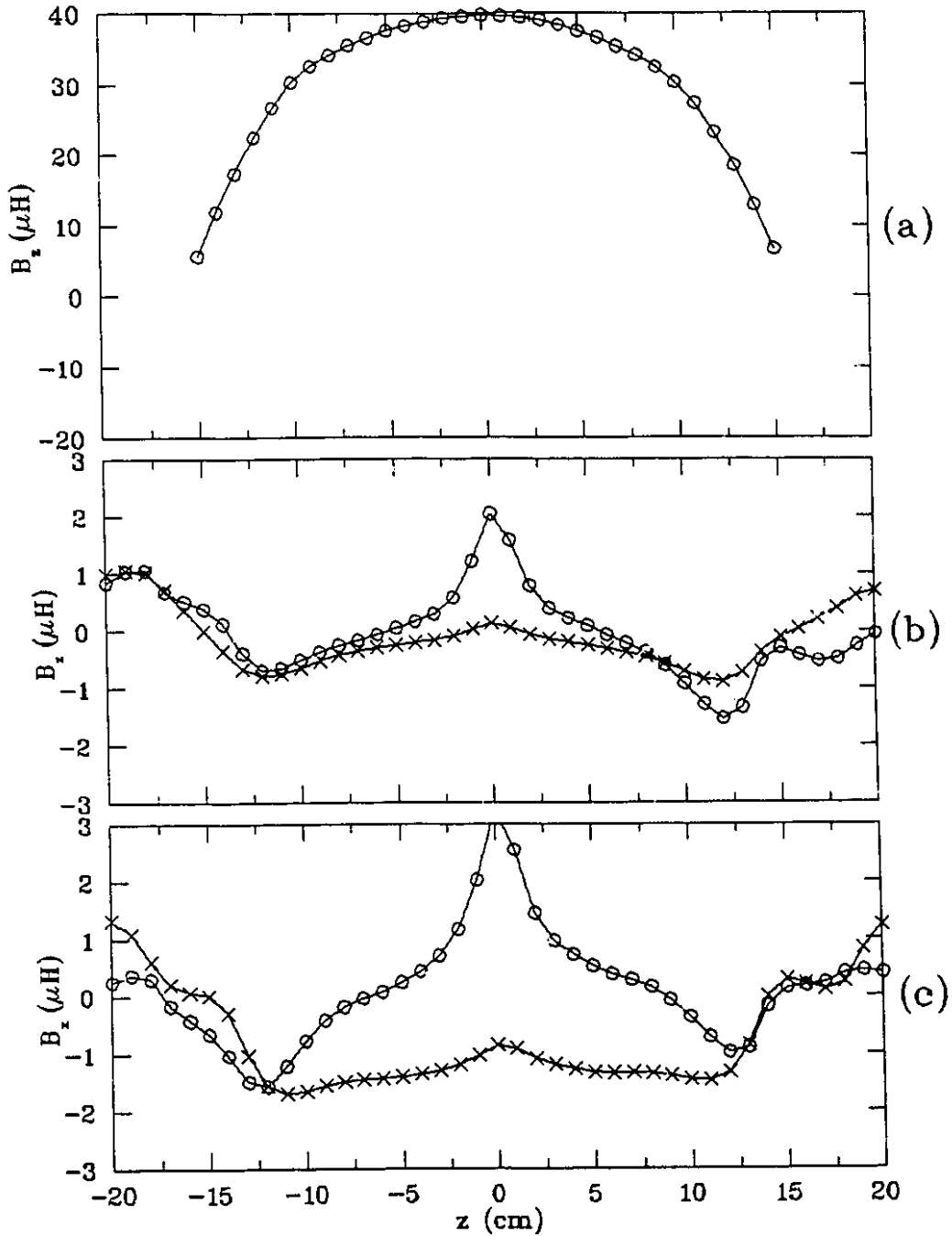


Figure 5.19: The longitudinal component of the fringe field,  $B_z$ , at  $x = -17.3$  cm and  $y = 0$ , generated by a 1 A, 1 kHz current, plotted as a function of  $z$  for (a) the unshielded primary coil, (b) the actively shielded coil and (c) the passively shielded coil. In (b) and (c), the in-phase and quadrature components are represented by (o) and (x), respectively.



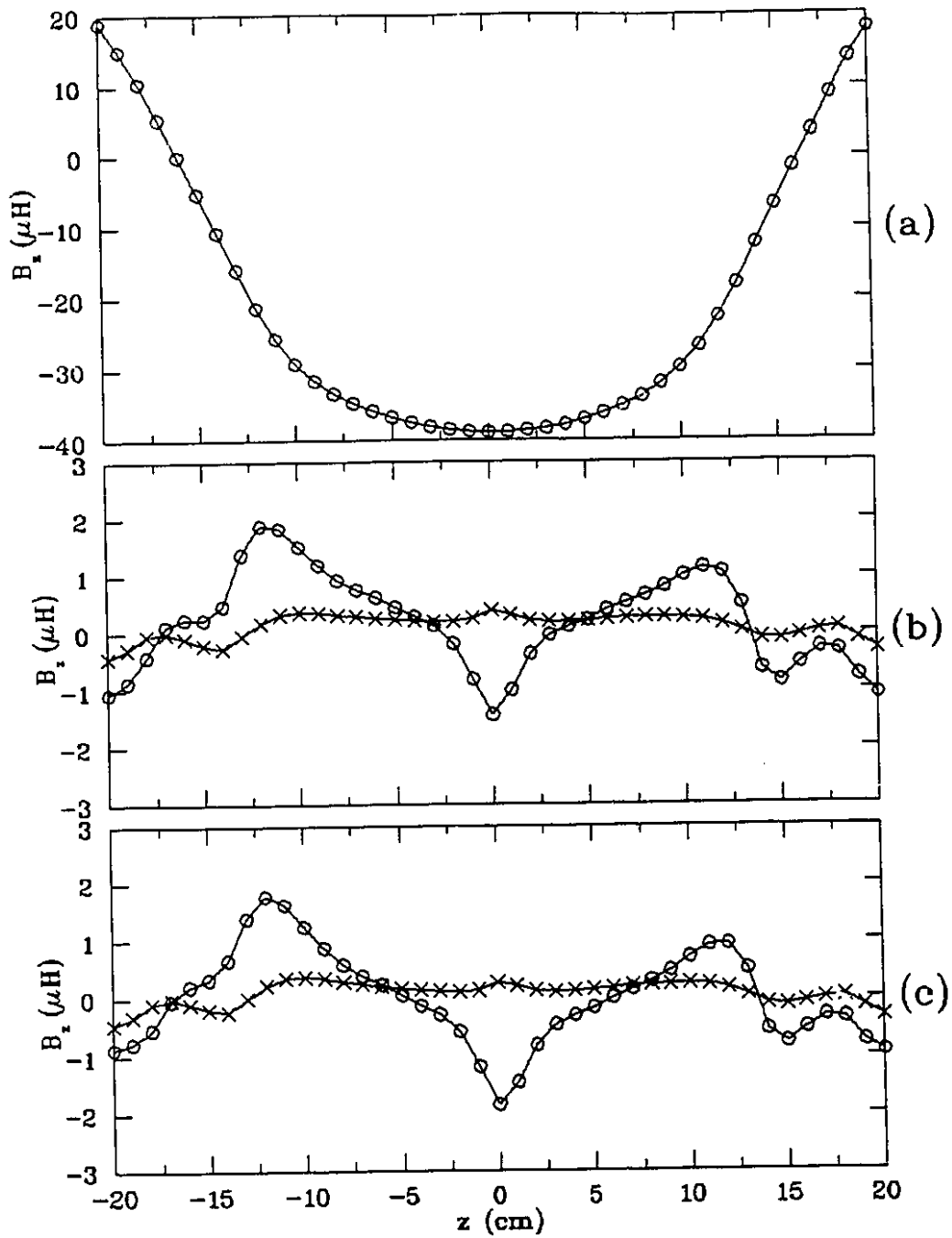


Figure 5.20: The longitudinal component of the fringe field,  $B_z$ , at  $x = 17.3$  cm and  $y = 0$ , generated by a 1 A, 5 kHz current, plotted as a function of  $z$  for (a) the unshielded primary coil, (b) the actively shielded coil and (c) the passively shielded coil. In (b) and (c), the in-phase and quadrature components are represented by (o) and ( $\times$ ), respectively.

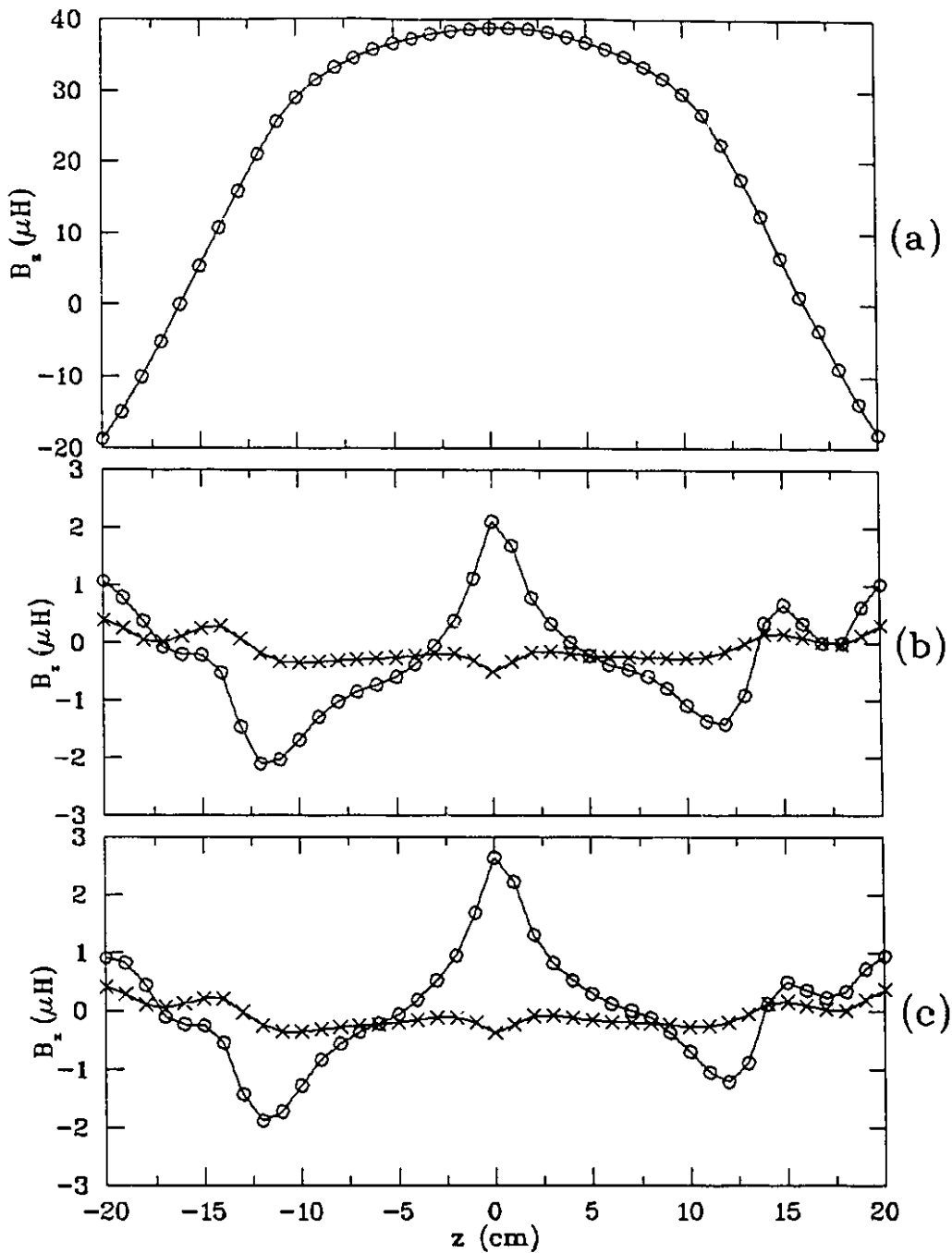


Figure 5.21: The longitudinal component of the fringe field,  $B_z$ , at  $x = -17.3$  cm and  $y = 0$ , generated by a 1 A, 5 kHz current, plotted as a function of  $z$  for (a) the unshielded primary coil, (b) the actively shielded coil and (c) the passively shielded coil. In (b) and (c), the in-phase and quadrature components are represented by (o) and ( $\times$ ), respectively.

coil. It can be seen that the in-phase component of the residual fringe field for the shielded coil near  $z = 0$  is of the same sign as the fringe field in the unshielded case, showing that there is insufficient shielding in that region. On the other hand, the opposite is the case near  $z = \pm 16$  cm, showing that there is overcompensation in that region. The imperfect shielding is possibly because of the “missing” current that should be flowing where the cuts are located. The cuts are about 1.6 mm wide, a significant proportion of the minimum width of the conducting path (4 mm).

Comparison of graphs (b) and (c) in Figures 5.14 to 5.21 shows that the behavior is very similar in the case of active and passive shielding. That indicates that the cuts are essentially parallel to the direction of the eddy current flow in the case of ideal passive shielding, from which it can be deduced that the cuts in the shielding coil are essentially everywhere parallel to the desired direction and that they are appropriately spaced to match the desired current density.

A further test of the effectiveness of the shielding provided by the coil can be made, after installation in the magnet, by direct observation of NMR, for example, by studying the shape of the projection image of a square sliced phantom as described by Robertson (1989).

## BIBLIOGRAPHY

- Abraham, A. (1961). *The Principles of Nuclear Magnetism*. Clarendon Press, Oxford.
- Bloch, F., Hansen, W.W., and Packard, M.E. (1946). *Phys. Rev.* **69**, 127.
- Brigham, E.O. (1974). *The Fast Fourier Transform*. Prentice-Hall, Englewood Cliffs, New Jersey.
- Chapman, B., Turner, R., Ordidge, R.J., Doyle, M., Cawley, M., Coxon, R., Glover, P., and Mansfield, P. (1987). *Magn. Reson. Med.* **5**, 246.
- Farrar, T.C., and Becker, E.D. (1971). *Pulse and Fourier Transform NMR*. Academic Press, New York.
- Golay, M.J.E. (1958). *Rev. Sci. Instrum.* **29**, 313.
- Hahn, E.L. (1950). *Phys. Rev.* **80**, 580.
- Henkelman, R.M., and Bronskill, M.J. (1987). *Rev. Magn. Reson. Med.* **2**, 1.
- Hoult, D.I. (1979). *J. Magn. Reson.* **35**, 69.
- Hutchison, J.M.S., Sutherland, R.J., and Mallard, J.R. (1978). *J. Phys. E: Sci. Instrum.* **11**, 217.
- Jackson, J.D. (1962). *Classical Electrodynamics*, pp. 84–86. Wiley, New York.
- Jehenson, P., Westphal, M., and Schuff, N. (1990). *J. Magn. Reson.* **90**, 264.
- Kreith, F., and Bohn, M.S. (1986). *Principles of Heat Transfer*, pp. 89–92. Harper & Row, New York.
- Kumar, A., Welte, D., and Ernst, R.R. (1975). *J. Magn. Reson.* **18**, 69.
- Landau, L.D., and Lifshitz, E.M. (1958). *Quantum Mechanics*, p. 55. Pergamon Press, London.
- Lauterbur, P.C. (1973). *Nature, Lond.* **242**, 190.

- Mahoney, C.L. (1990). *Handbook of Adhesives*, Skeist, I., ed., p. 74. Van Nostrand Reinhold, New York.
- Mansfield, P., and Chapman, B. (1986). *J. Phys. E: Sci. Instrum.* **19**, 540.
- Mansfield, P., and Grannell, P.K. (1973). *J. Phys. C: Solid State Phys.* **6**, L422.
- Morris, P.G. (1986). *Nuclear Magnetic Resonance Imaging in Medicine and Biology*. Clarendon Press, Oxford.
- Morse, P.M., and Feshbach, H. (1953a). *Methods of Theoretical Physics*, Vol. 1, pp. 38–39. McGraw-Hill, New York.
- Morse, P.M., and Feshbach, H. (1953b). *Methods of Theoretical Physics*, Vol. 1, p. 314. McGraw-Hill, New York.
- Ordidge, R.J., and Cresshull, I.D. (1986). *J. Magn. Reson.* **69**, 151.
- Robertson, S. (1989). *M.Sc. Thesis*, University of Alberta, Edmonton, Alberta.
- Slichter, C.P. (1978). *The Principles of Magnetic Resonance*. Springer-Verlag, New York.
- Tanner, I.E. (1965). *Rev. Sci. Instrum.* **36**, 1086.
- Turner, R. (1986). *J. Phys. D: Appl. Phys.* **19**, L147.
- Turner, R. (1988). *J. Phys. E: Sci. Instrum.* **21**, 948.
- Turner, R. (1989). *Private communication*.
- Turner, R. (1990). *Private communication*.
- Turner, R., and Bowley, R.M. (1986). *J. Phys. E: Sci. Instrum.* **19**, 876.
- Turner, R., Chapman, B., Howseman, A.M., Ordidge, R.J., Coxon, R., Glover, P., and Mansfield, P. (1988). *J. Magn. Reson.* **80**, 248.
- Van Vaals, J.J., and Bergman, A.H. (1990). *J. Magn. Reson.* **90**, 52.